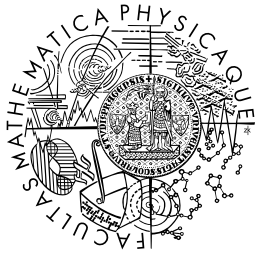

FACULTY
OF MATHEMATICS
AND PHYSICS
Charles University

MASTER THESIS

Dominika Hájková

Towards improved orographic gravity wave parameterization in chemistry-climate models.

Department of Atmospheric Physics

Supervisor of the master thesis: RNDr. Petr Šácha, Ph.D.

Study programme: Atmospheric Physics, Meteorology and Climatology

Study branch: Physics

Prague 2024

I declare that I carried out this master thesis independently, and only with the cited sources, literature and other professional sources. It has not been used to obtain another or the same degree.

I understand that my work relates to the rights and obligations under the Act No. 121/2000 Sb., the Copyright Act, as amended, in particular the fact that the Charles University has the right to conclude a license agreement on the use of this work as a school work pursuant to Section 60 subsection 1 of the Copyright Act.

In ..... date ....

Author's signature

My greatest thanks go to my supervisor RNDr. Petr Šácha, Ph.D. for all his help and guidance. I would also like to thank doc. Mgr. Peter Huszár, Ph.D. and Mgr. Jan Karlický, Ph.D. for their help with compilation of models ICAR and WRF-ARW respectively and Dr. Andreas Dörnbrack for providing the sounding data needed for the simulations.

Title: Towards improved orographic gravity wave parameterization in chemistry-climate models.

Author: Dominika Hájková

Department: Department of Atmospheric Physics

Supervisor: RNDr. Petr Šácha, Ph.D., Department of Atmospheric Physics

Abstract: Orographic gravity waves are ubiquitous in our atmosphere, having a large impact on the energy and momentum transport. Their scales reflect scales of the orography and as such global circulation models cannot resolve them and they need to be parameterized. In this thesis we will introduce the theory behind gravity waves and flow around an obstacle such as a mountain. We show their impact in global models and how they interact with the resolved planetary waves. In the last part of this work we will introduce several idealized simulations, analyzing the resulting wave activity and effects connected to it. We finish with comparison of different parameterization schemes applied on coarse resolution simulations and evaluation of their performance.

Keywords: internal gravity waves, stratosphere, chemistry-climate models

Contents

Introduction

Gravity waves (GWs) are intermittent and ubiquitous, naturally occurring in our atmosphere. They have different sources, but in this work we will concern ourselves with waves created by the orography, orographic gravity waves (OGWs). This topic is very important, since OGWs have a great influence on the dynamics and energy transport, especially in the middle atmosphere. For this reason, their effects must be included in global circulation models (GCMs), to better represent real atmosphere. Currently, GCMs have quite coarse horizontal resolution in orders up to hundreds of kilometres. OGWs exist on quite small scales, which largely reflect the scales of the orography. For that reason the models cannot resolve them explicitly and we must use parameterization to represent their effects.

Parameterizations of OGWs use lot of different simplifications. They are based on the linear wave theory and the only represented effect is a drag force, which causes deceleration in regions of GW breaking. Strong impact of this drag on the model dynamics have been showed in several studies. However, this impact may be to a large extent overestimated and possibly artificial, created by the models. This is due to the different formulation of the parameterization schemes as well as because of only loosely constrained tuning of the individual parameters, which control not only the amount of the drag but also its distribution in the atmosphere.

This thesis is a direct continuation of my bachelor thesis and as such we will build on that work, in some cases referencing to it as not to repeat previously stated information. We will start by the theory and description of OGWs, by possible non-linear effects connected to the waves, and how we can predict the resulting wave field and its characteristics.

We will continue with expanding our research of OGWs effect in CMIP6 (Coupled Model Intercomparison Project Phase 6) models. We focus especially on the impact of parameterized drag on the resolved, planetary waves. Planetary waves are one of the important driving mechanisms in global dynamics and their misrepresentation in the models can have negative impacts on short-term forecasts as well as long-term future projections.

Last part of this thesis will be dedicated to inspection of different variations of parameterization schemes. We create several high-resolution idealized simulations of flow over a singular hill. We use a state of the art research and forecasting model WRF-ARW. We analyze the situations, looking at the differences between the simulations and the interaction of waves with the mean flow. We then replicate those simulations, using coarse horizontal resolution representing the global models, and we will apply the different parameterization schemes. We will try to diagnose weaknesses and strengths of each parameterization scheme, based on how well they are able to replicate the real drag caused by OGWs.

1. Gravity waves, dynamics and theory of flow over orography

There exist many types of wave motions in the terrestrial atmosphere and ocean. Waves are typically resulting from a deviation to a balanced state with some restoring mechanism acting against the deviation. The waves can be classified based on the restoring mechanisms. For example Rossby waves are naturally occurring in rotational mediums due to the gradient of potential vorticity which stems from latitudinal difference of the Coriolis parameter. Whereas internal gravity waves can exist due to restoring force of stratification [Bühler, 2014].

We can divide waves also by their scale. There exist large scale waves, with wavelengths of thousands of kilometres, such as Rossby waves or inertia gravity waves and small scale, with wavelengths of few to few hundreds of kilometres, such as convective or OGWs. Although different in nature, all of those waves play an important role in the atmospheric dynamics.

1.1 Formation of gravity waves

Internal GWs are ubiquitous in the atmosphere and have several different sources such as overshooting tops of convective clouds, eruptions of volcanoes, and also orography, which is the focus of this thesis. Before we introduce the problem of a flow over an obstacle such as a mountain, we will describe the sourcing of gravity waves in general. As mentioned before, gravity waves are enabled by stratification of the atmosphere which is described by the so called Brunt-Väisälä frequency, N,

$$N = \sqrt{\frac{g}{\theta}\frac{\partial\theta}{\partial z}} = \sqrt{-\frac{g}{\rho}\frac{\partial\rho}{\partial z}}, \tag{1.1}$$

where θ is the potential temperature and ρ is the density. It is the natural frequency of an oscillating air particle which follows from description of Newton's second law applied on this particle once it is displaced from its original position as showed in [Hájková, 2022]. Vertical motion of this particle then can be described as

$$\delta z(t) = Ae^{iNt} + Be^{-iNt}. \tag{1.2}$$

As we can see from the equation, the nature of the resulting motion depends on the Brunt-Väisälä frequency. If N is imaginary, meaning that the potential temperature is decreasing with the height, the second term of the equation, Be^{-iNt}, will go to infinity. In that case, the displacement of the particle will only grow with time as the atmosphere is unstably stratified. The first term on the contrary goes to zero, so it is of no concern to us. However, if the potential temperature is increasing, i.e. if the atmosphere is stably stratified, the solution represents a harmonic oscillator.

It can be shown that GWs do not have necessarily frequency of N. In deriving the particle displacement we supposed that the motion is strictly vertical. However, that is rarely the case and once we take into consideration that the particle

may be displaced at an angle, we can see, that N is only an upper limit of the GW frequency, as we show later.

1.2 Equations of motion for gravity waves

Although GWs and their interactions are fairly non-linear in nature, in many cases linear wave theory can be used for their description with surprising accuracy. To derive the governing equations we will start with a set of Eulerian equations in Cartesian coordinates, which describe conservation of momentum, and we also add conservation of mass and energy in a friction-less atmosphere following [Holton, 2013]:

$$\rho\left(\frac{Du}{Dt} - fv\right) + \frac{\partial p}{\partial x} = 0, \tag{1.3a}$$

$$\rho\frac{Dw}{Dt} + \frac{\partial p}{\partial z} + \rho g = 0, \tag{1.3b}$$

$$\frac{D\rho}{Dt} + \rho\nabla\cdot\vec{u} = 0, \tag{1.3c}$$

$$\frac{D\theta}{Dt} = 0. \tag{1.3d}$$

$\frac{D}{Dt}$ represents a material derivative,

$$\frac{D}{Dt} = \frac{\partial}{\partial t} + \vec{u}\cdot\nabla. \tag{1.4}$$

For easier notation we restricted ourselves only to 2D motions.

This set of equations permits not only existence of GWs, but also existence of acoustic waves. This compressible formulation is unnecessary for us and highly increases potential computational costs. To filter sound waves from the system, we will use the Boussinesq approximation, e.g. [Sutherland, 2010]. This approximation assumes that changes in the density are significant only when connected to the buoyancy term, so only in the term including g. We also assume, that the vertical scales of motions we are examining are smaller than the scale height of the atmosphere,

$$H_s = \frac{RT_0}{g}. \tag{1.5}$$

Depending on what part of the atmosphere we are talking about, i.e. what is the temperature in the formula, the scale height is $\approx 6.4 - 8.4$ km. In general, the assumption that the perturbations caused by waves are small is the base of the linear wave theory.

To continue with this approximation, we want to decompose the density to the mean state and perturbation caused by the waves, so we can write it as $\rho = \rho_0(z) + \rho_1(x, z, t)$. Due to our assumption that the vertical motions are small, it stands that $\rho_1/\rho_0 << 1$. We will do the same decomposition for the pressure and substitute both in the equations we have and divide by the mean state density. Taking into account that the mean state pressure will change only in the vertical direction the momentum equations will become

$$\left(1 + \frac{\rho_1}{\rho_0}\right)\left(\frac{Du}{Dt} - fv\right) + \frac{1}{\rho_0}\frac{\partial p_1}{\partial x} = 0 \tag{1.6a}$$

$$\left(1+\frac{\rho_1}{\rho_0}\right)\frac{Dw}{Dt}+\frac{1}{\rho_0}\frac{\partial p_0}{\partial z}+\frac{1}{\rho_0}\frac{\partial p_1}{\partial z}+\left(1+\frac{\rho_1}{\rho_0}\right)g=0. \tag{1.6b}$$

We can also assume that the background pressure is hydrostatic i.e.:

$$-\frac{\partial p_0}{\partial z}=\rho_0 g, \tag{1.7}$$

which will simplify the second equation.

As we said, it follows from Boussinesq approximation that we take the fluid - air - as incompressible e.g. in [Sutherland, 2010], which will in this case simplify the mass conservation equation giving us $\nabla\cdot\vec{u}=0$. The last equation, conservation of energy, can be approximated in several ways, including using density instead of potential temperature e.g. in [Holton, 2013], which we will use here. Since the mean state density is not changing in time nor horizontal direction, we can expand the time derivative and get

$$\frac{D\rho_1}{Dt}=-w\frac{\partial\rho_0}{\partial z}. \tag{1.8}$$

Substituting potential temperature in the last equation with Brunt-Väisälä frequency, altogether we will get set of Boussinesq equations:

$$\frac{Du}{Dt}-fv+\frac{1}{\rho_0}\frac{\partial p_1}{\partial x}=0, \tag{1.9a}$$

$$\frac{Dw}{Dt}+\frac{1}{\rho_0}\frac{\partial p_1}{\partial z}+\frac{\rho_1}{\rho_0}g=0, \tag{1.9b}$$

$$\nabla\cdot\vec{u}=0, \tag{1.9c}$$

$$\frac{D\rho_1}{Dt}+w\frac{\rho_0}{g}N^2=0. \tag{1.9d}$$

1.3 Taylor-Goldstein equation

To study the flow around an obstacle such as a hill we would like to have a wave equation which will predict vertical velocities based on the background wind and shape of the hill. To achieve this we will start by deriving Taylor-Goldstein equation (TGE) which was published by G.I. Taylor and S. Goldstein in 1931 ([Taylor, 1931],[Goldstein and Taylor, 1931]) and governs shear-flow disturbances. This equation is often derived using stream function ψ e.g. in [Sutherland, 2010], we will however derive it using explicitly the vertical velocity similarly to derivations by original authors, following [Nappo, 2002]. We take our set of 2D Boussinesq equations, this time in irrotational fluid and linearise all velocities according to $q(x,z,t)=q_0(z)+q_1(x,z,t)$. $q_1(x,z,t)$ are the disturbances, being order of O(a), where a is the amplitude of the wave. Anything of the order $O(a^2)$ is considered neglectable, due to the previously mentioned assumption of the linear theory, that the disturbances are always small. We will get

$$\frac{\partial u_1}{\partial t}+u_0\frac{\partial u_1}{\partial x}+w_1\frac{\partial u_0}{\partial z}+\frac{1}{\rho_0}\frac{\partial p_1}{\partial x}=0, \tag{1.10a}$$

$$\frac{\partial w_1}{\partial t} + u_0 \frac{\partial w_1}{\partial x} + \frac{1}{\rho_0}\frac{\partial p_1}{\partial z} + \frac{\rho_1}{\rho_0} g = 0, \tag{1.10b}$$

$$\frac{\partial u_1}{\partial x} + \frac{\partial w_1}{\partial z} = 0, \tag{1.10c}$$

$$\frac{\partial \rho_1}{\partial t} + u_0 \frac{\partial \rho_1}{\partial x} + w_1 \frac{\rho_0}{g} N^2 = 0. \tag{1.10d}$$

We are interested in wave-like solutions, hence we can assume that the perturbances have a form of a wave such as

$$q_1(x, z, t) = \hat{q}(z) e^{i(kx - \omega t)}, \tag{1.11}$$

where ω is the extrinsic wave frequency and k is the horizontal wave number in the direction of x defined as $2\pi/\lambda_x$. More correctly the argument of exponential should be $i(kx - \omega t) + z/2H_s$, which considers the exponential decline of atmospheric density [Fritts and Alexander, 2020]. However, it should be mentioned that it is usually neglected during the derivation of TGE. After inserting this into our equations we will get a new set of equations, which we will further simplify by using intrinsic frequency $\Omega = \omega - ku_0$. This will get us

$$i\Omega\hat{u} - \hat{w}\frac{du_0}{\mathrm{d}z} - i\frac{k}{\rho_0}\hat{p} = 0, \tag{1.12a}$$

$$i\Omega\hat{w} - \frac{1}{\rho_0}\frac{d\hat{p}}{\mathrm{d}z} - \frac{\hat{\rho}}{\rho_0} g = 0, \tag{1.12b}$$

$$ik\hat{u} + \frac{d\hat{w}}{\mathrm{d}z} = 0, \tag{1.12c}$$

$$i\Omega\hat{\rho} + \hat{w}\frac{\rho_0}{g} N^2 = 0. \tag{1.12d}$$

These equations describe relations between amplitudes of wave perturbations of different variables and are called polarization relations [Fritts and Alexander, 2020]. Now we want to derive an equation for the vertical structure of $\hat{w}$. We start by inserting $\hat{u}$ from Equation 1.12c to Equation 1.12a. We will also insert $\hat{\rho}$ from Equation 1.12d to Equation 1.12a. This will get us two equations which we both multiply by ρ_0 and get

$$-\rho_0 \frac{\Omega}{k}\frac{d\hat{w}}{\mathrm{d}z} - \rho_0 \hat{w}\frac{du_0}{\mathrm{d}z} - ik\hat{p} = 0, \tag{1.13a}$$

$$i\rho_0\Omega\hat{w} - \frac{d\hat{p}}{\mathrm{d}z} - i\frac{\rho_0}{\Omega} N^2 \hat{w} = 0. \tag{1.13b}$$

We see, that we still have to get rid of $\hat{p}$. We do this by taking the z-derivative of Equation 1.13a and subtracting Equation 1.13b times ik. Remembering that $\Omega = \omega - ku_0$ and multiplying the result by $-k\rho_0/\Omega$ the resulting equation is

$$\frac{\mathrm{d}^2\hat{w}}{\mathrm{d}z^2} + \frac{1}{\rho_0}\frac{d\rho_0}{\mathrm{d}z}\frac{d\hat{w}}{\mathrm{d}z} + \left[\frac{k^2N^2}{\Omega^2} + \frac{k}{\Omega}\frac{\mathrm{d}^2u_0}{\mathrm{d}z^2} + \frac{k}{\Omega}\frac{1}{\rho_0}\frac{d\rho_0}{\mathrm{d}z}\frac{du_0}{\mathrm{d}z} - k^2\right]\hat{w} = 0. \tag{1.14}$$

We will now consider the exponential decline of density

$$\rho_0 = \rho_s e^{z/H_s} \rightarrow \frac{\partial \rho_0}{\partial z} = -\frac{\rho_0}{H_s}. \tag{1.15}$$

$$\frac{\mathrm{d}^2\hat{w}}{\mathrm{d}z^2} - \frac{1}{H_s}\frac{d\hat{w}}{\mathrm{d}z} + \left[\frac{k^2N^2}{\Omega^2} + \frac{k}{\Omega}\frac{\mathrm{d}^2u_0}{\mathrm{d}z^2} - \frac{k}{\Omega}\frac{1}{H_s}\frac{du_0}{\mathrm{d}z} - k^2\right]\hat{w} = 0. \tag{1.16}$$

To simplify the equation more, we will also substitute $c = \Omega/k + u_0$, which is the apparent horizontal phase speed in x direction. This results in TGE

$$\frac{\mathrm{d}^2\hat{w}}{\mathrm{d}z^2} - \frac{1}{H_s}\frac{d\hat{w}}{\mathrm{d}z} + \left[\frac{N^2}{(c-u_0)^2} + \frac{u_0''}{c-u_0} - \frac{1}{H_s}\frac{u_0'}{c-u_0} - k^2\right]\hat{w} = 0, \tag{1.17}$$

where $u_0' = du_0/\mathrm{d}z$. Terms including the scale height in the denominator are usually neglected,

$$\frac{\mathrm{d}^2\hat{w}}{\mathrm{d}z^2} + \left[\frac{N^2}{(c-u_0)^2} + \frac{u_0''}{c-u_0} - k^2\right]\hat{w} = 0. \tag{1.18}$$

Equation 1.18 is the most used form of TGE and it tells us the expected wave field based on the background variables and the wave characteristic in a form of the horizontal wave number. We can see that it actually gives us also a condition for the wave number. To get periodic solution, waves, to this equation we need the term in the square brackets to be positive. We need to apply:

$$\frac{N^2}{(c-u_0)^2} + \frac{u_0''}{c-u_0} > k^2. \tag{1.19}$$

In case of OGWs, this condition actually defines a so called Scorer parameter l, [Nappo, 2002]. Firstly, we need to realise that the apparent horizontal phase speed in the case of a mountain wave is zero. Waves are created above the mountain and to an outside observer appear stationary. This means, that their intrinsic phase speed $c_1 = \Omega/k$ is equal but opposite to the background wind speed, for the apparent phase speed to be zero, as we see in Figure 1.1.

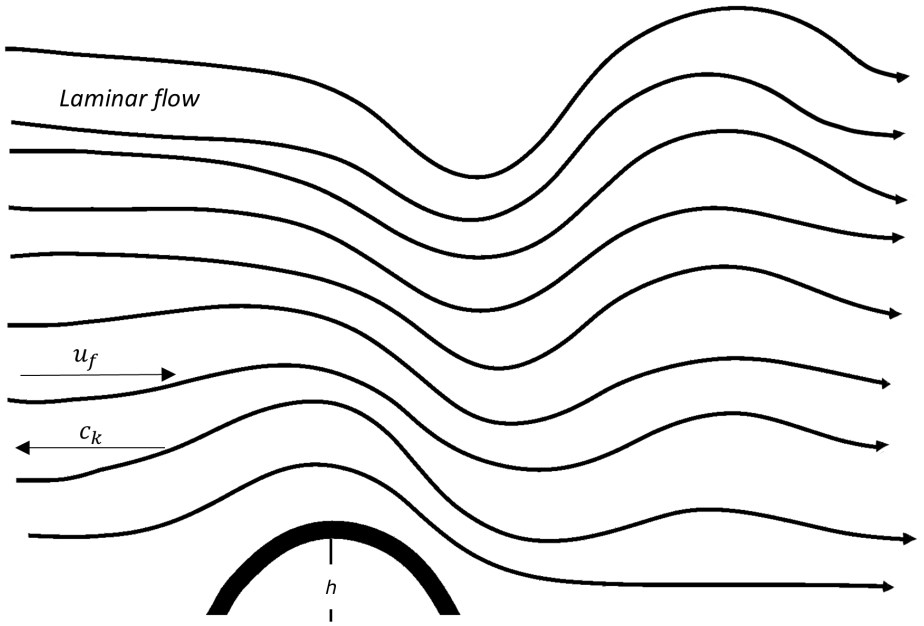

Figure 1.1: Illustration of flow with velocity u_f and resulting formation of OGWs with intrinsic phase speed C_k

This will give us Scorer parameter defined as:

$$l^2 = \frac{N^2}{u_0^2} - \frac{u_0''}{u_0} \tag{1.20}$$

1.4 Flow around an obstacle

To test a model, we usually want to compare its results with some observation and or an analytical solutions. In the case of a flow over a mountain we can derive analytical solution in some idealized cases, where the background variables as well as the mountain are as simple as possible. We will derive this solution for a case with a constant background wind and Brunt-Väisälä frequency — meaning with constant stratification. In this case we mean constant in space as well as time. As we showed in the previous section, the apparent phase speed for mountain waves is zero, which gives us simplified version of TGE from Equation 1.18:

$$\frac{\mathrm{d}^2\hat{w}}{\mathrm{d}z^2} + \left[\frac{N^2}{u_0^2} - k^2\right]\hat{w} = 0. \tag{1.21}$$

Now we have to consider how does w_1, which we want to express, relate to $\hat{w}$. Our assumption of the wave-like solution during derivation of the TGE also means that we would get the same set of equations using Fourier transform [Achatz, 2022]. Or in other words we can define Fourier transform as

$$\hat{w}(k,z) = \int_{-\infty}^{\infty} w_1(x,z)e^{-ikx}\mathrm{d}x \tag{1.22}$$

and inverse Fourier transform as

$$w_1(x,z) = \frac{1}{2\pi}\int_{-\infty}^{\infty} \hat{w}(k,z)e^{ikx}\mathrm{d}k, \tag{1.23}$$

which we will use later. Note that ωt is not present in this version of Fourier transform due to the zero extrinsic frequency. With our condition defined by the Scorer parameter that $l^2 > k^2$ our solution for TGE is

$$\hat{w}(k,z) = Ae^{-i\left(\sqrt{\frac{N^2}{u_0^2}-k^2}\right)z} + Be^{i\left(\sqrt{\frac{N^2}{u_0^2}-k^2}\right)z} = Ae^{-imz} + Be^{imz}, \tag{1.24}$$

where m is the vertical wave number. Firstly we will apply the top boundary condition in the form of a so called radiation boundary condition [Klemp and Durran, 1983]. This means that we allow only upward propagation at the top, which will ensure no reflection there. This condition means that B must be zero. Following [Nappo, 2002] we will define bottom boundary condition to resolve A. To get $\hat{w}(k,0)$ we will firstly get $w_1(x,0)$. The flow is irrotational and without friction, so we can say that the streamline at the surface is of the form of the surface itself, meaning the it can be defined using parametric equation as

$$r = z - h(x), \tag{1.25}$$

where $h(x)$ is the height of the obstacle. This works quite well in a case of a small hill. From the definition of a streamline we know that gradient of the streamline will be normal to the wind velocity which has both the background and perturbation component. In 2D we will get

$$\vec{U}\cdot\nabla r = (u_0 + u_1, w_1)\cdot\left(-\frac{\mathrm{d}h}{\mathrm{d}x}, 1\right) = 0. \tag{1.26}$$

In the linear limit, $\mathrm{d}h/\mathrm{d}x$ must be order of magnitude O(a). Hence, the product of u_1 and $\mathrm{d}h/\mathrm{d}x$ will be neglected and we can express w_1

$$w_1(x,0) = u_0 \frac{\mathrm{d}h}{\mathrm{d}x}. \tag{1.27}$$

If we substitute that to Equation 1.22 and use differentiation property of Fourier transform we will get

$$A = \hat{w}(k,0) = \int_{\infty}^{\infty} u_0 \frac{\mathrm{d}h}{\mathrm{d}x} e^{-ikx} \mathrm{d}x = u_0 \frac{\mathrm{d}\hat{h}}{\mathrm{d}x} = iu_0 k\hat{h}. \tag{1.28}$$

This way we got exact solution for $\hat{w}(k,z)$, which can be substituted to Equation 1.23 of inverse Fourier transform to finally get the solution for vertical wind speed perturbation caused over hill described by $h(x)$

$$w_1(x,z) = \frac{1}{2\pi} \int_{-\infty}^{\infty} iu_0 k\hat{h} e^{-imz} e^{ikx} \mathrm{d}k. \tag{1.29}$$

Using limitation of the Scorer parameter we can define maximum horizontal wave number $|k_m| = N/u_0$. We can also simplify the integral by realising that the imaginary part of the exponential is an odd function and the real part is an even function which altogether gives us

$$w_1(x,z) = \frac{1}{\pi} \int_{0}^{k_m} -iu_0 k\hat{h} \Re(e^{-imz} e^{-ikx}) \mathrm{d}k. \tag{1.30}$$

Because the wave vector has opposite direction than the wind, we take only the negative horizontal wave numbers, which accounts for the minus signs in front of k terms.

From this equation we can analytically calculate the stationary mountain wave solutions for comparison with numerical model simulations of the exact problem. Most often used types of a hill are the so called Witch of Agnesi hill

$$h_A = \frac{Ha^2}{x^2 + a^2} \tag{1.31}$$

and Gaussian hill

$$h_G = He^{-\frac{x^2}{a^2}}. \tag{1.32}$$

Solutions for those hills will be derived in the last part of this thesis.

1.5 Energetics

In the previous section, we used momentum equations to derive the form of OGWs. Now, we use those equations to describe the wave energy transport, as it is crucial for describing their role in the mean flow interactions as well as for the parameterization development. Following [Sutherland, 2010] we will first consider momentum equation (in 2D) in its vector form and make the dot product with $\vec{u}$ or in other words adding together Equation 1.10a multiplied by u_1 and Equation 1.10b multiplied by w_1. Using continuity equation Equation 1.10c we get:

$$\frac{D}{Dt}\left[\frac{1}{2}\rho(u_1^2 + w_1^2)\right] + \rho_1 g w_1 = -\frac{\partial}{\partial x}(u_1 p_1) - \frac{\partial}{\partial z}(w_1 p_1) - \rho_0 u_1 w_1 \frac{\mathrm{d}u_0}{\mathrm{d}z}. \tag{1.33}$$

The first term in the brackets on the left is obviously perturbation kinetic energy. However, we want to get also the potential perturbation energy in the material derivative. We can do that by modifying the second term on the left, by firstly defining vertical displacement as $w_1 = D\delta/Dt$. We will use this and equation Equation 1.8 which will get us

$$\rho_1 = -\frac{\mathrm{d}\rho_0}{\mathrm{d}z}\delta. \tag{1.34}$$

Using this definition, perturbation potential energy itself can be defined as

$$E_p = \rho_1 g\frac{\delta}{2} = -\frac{1}{2}\frac{\mathrm{d}\rho_0}{\mathrm{d}z}g\delta^2 = \frac{1}{2}\rho_0 N^2\delta^2 \tag{1.35}$$

This will give us rate of change for perturbation potential energy as

$$\frac{DE_p}{Dt} = \rho_1 g w_1 = \frac{D}{Dt}\left(\frac{1}{2}\rho_0 N^2\delta^2\right). \tag{1.36}$$

Equation of the total energy is then

$$\frac{DE}{Dt} + \frac{\partial}{\partial x}u_1 p_1 + \frac{\partial}{\partial z}w_1 p_1 = -\rho_0 u_1 w_1\frac{\mathrm{d}u_0}{\mathrm{d}z}, \tag{1.37}$$

where the second and third term on the left are divergences of non-advective horizontal and vertical fluxes of energy. We will now consider special case, where the background wind is zero. We will take horizontal average of the energy equation, showed by the overbar, over one wavelength, which due to the periodicity will cancel the second term on the left. We then get the conservation law for total energy in the stationary wind field

$$\frac{\partial\overline{E}}{\partial t} = -\frac{\partial\overline{w_1 p_1}}{\partial z} = -\frac{\partial F}{\partial z.} \tag{1.38}$$

It can be shown ([Nappo, 2002]) that this flux F is related with the group velocity by

$$F = c_{gz}\overline{E}, \tag{1.39}$$

where $c_{gz} = \partial\omega/\partial m$ is the group velocity in the vertical direction. Of course, in the presence of the background flow, the term cannot be simplified this way.

In a shear flow, the term on the right of Equation 1.37 does not disappear. We would like to derive conservation law of energy for this more realistic case. It stands [Nappo, 2002], that

$$\rho_0\overline{u_1 w_1} = \frac{k}{\Omega}\overline{w_1 p_1} = \frac{k}{\Omega}c_{gz}\overline{E}. \tag{1.40}$$

We can use fact the that z-derivative of Ω can be written as

$$\frac{\partial\Omega}{\partial z} = \frac{\partial\omega - ku_0}{\partial z} = -k\frac{\partial u_0}{\partial z}. \tag{1.41}$$

We will put all of this together and since we take Ω as constant in time, we can write the horizontally averaged energy Equation 1.33 as

$$\frac{\partial\overline{E}}{\partial t} + \frac{\partial c_{gz}\overline{E}}{\partial z} + \frac{k}{\Omega}c_{gz}\overline{E}\frac{\mathrm{d}u_0}{\mathrm{d}z} = \Omega\frac{\partial}{\partial t}\left(\frac{\overline{E}}{\Omega}\right) + \Omega\frac{\partial}{\partial z}\left(c_{gz}\frac{\overline{E}}{\Omega}\right) = 0, \tag{1.42}$$

which gives us the conservation law for wave energy in a shear flow constant in time.

$$\frac{\partial}{\partial t}\left(\frac{\overline{E}}{\Omega}\right) = -\frac{\partial}{\partial z}\left(c_{gz}\frac{\overline{E}}{\Omega}\right), \tag{1.43}$$

where $\overline{E}/\Omega$ is the so-called pseudoenergy, one of the proxies for a wave action.

Biggest attention from OGWs effects on the atmosphere receives the deceleration of the background flow due to the OGW drag. This effect can be illustrated from the conservation of momentum or more precisely of the so-called pseudomomentum.

To derive this conservation law, we will use first momentum Equation 1.9a and apply horizontal averaging across the horizontal wavelength while using continuity equation. This will get us rid of the x-derivatives. Using also the decomposition into mean and perturbation parts we will arrive at equation ([Bühler, 2014],[Sutherland, 2010])

$$\frac{\partial \overline{u}}{\partial t} = \frac{\partial \overline{u_1 w_1}}{\partial z}, \tag{1.44}$$

which shows on the right-hand side the vertical flux of horizontal momentum, which we will call momentum flux in short. The right-hand side is already known to us from manipulations of the pseudoenergy equation. Term $u_1 w_1$ is a component of the Reynold's stress tensor and as we showed in [Hájková, 2022], it is closely tied to the OGW drag.

1.6 Reflection and resonance of waves

We will now delve into effects which can arise during flow around a hill allowing background winds or stratification to vary with altitude. In geometric optics, if there is a change in the index of refraction, light is reflected and or changes its path in the new environment. This happens similarly in our case of OGWs, where fast change in Brunt-Väisälä frequency or wind speed affects in turn the vertical wave number. Although those effects are not easily described in real case, we will briefly describe theory behind them, as reflection and resonance are actually in some form considered in some OGW parameterizations.

1.6.1 Reflection

Following [Nappo, 2002], we will consider flow in two layers with interface at the boundary height z_b, which has constant background variables and the layer differ only in stratification N which we will denote N_A and N_B. We want to study, how a change in the Brunt-Väisälä frequency, wave number and wave frequency are connected. We can demonstrate it using a simplified dispersion relation [Fritts and Alexander, 2020] in the form

$$\omega = \frac{kN}{\sqrt{k^2 + m^2}} = N\cos\alpha. \tag{1.45}$$

Where α is the angle between the horizontal direction and the wave vector, which is perpendicular to the wave fronts. This relation shows us how the wave frequency is limited by Brunt-Väisälä frequency but not necessary equal to it. We

will go back to our two-layer flow. We expect, that in the case of a sharp change of stratification some of the waves travelling upward from the boundary will be refracted, but also reflected back downward from the boundary between the layers. For these waves, we can say that the wave frequency as well as horizontal wave numbers will remain the same. From the dispersion relations this tells us that the vertical wave number must change. We also want to apply boundary conditions. First condition we get from the dispersion relation and the unchanging wave frequency meaning

$$N_A \cos \beta_A = N_B \cos \beta_B. \tag{1.46}$$

This condition can be fulfilled only in the case of a stably stratified atmosphere. In the case of a neutral or unstable atmosphere the waves do not propagate here and are evanescent as in agreement with our previous analysis. Another boundary condition is dynamical boundary condition which says that the pressure including the perturbation parts must equal at both sides of the boundary

$$p_{A,0}(z_b) + p_{A,1}(z_b) = p_{B,0}(z_b) + p_{B,1}(z_b). \tag{1.47}$$

We also need kinematic boundary condition, which tells us, that the local mass vertical fluxes are equivalent in both directions

$$\rho_{A,0}(z_b) w_1(z_b) = \rho_{B,0} w_1(z_b). \tag{1.48}$$

We can use these conditions to find the ratio between the amplitude of the reflected and original wave, which we call reflection index r. Firstly, we use our boundary and kinematic condition to combine them to one

$$\frac{p_A(z_b)}{\rho_{A,0}(z_b) w_A(z_b)} = \frac{p_B(z_b)}{\rho_{B,0}(z_b) w_B(z_b)} \rightarrow Z_A(z_b) = Z_B(z_b), \tag{1.49}$$

which is called impedance. Impedance can be calculated, if we consider, that in the upper layer we have only the refracted wave and in the lower layer we have both the original and reflected wave, [Gill, 1982]. It is easier to start with the wave that was transmitted through as it is only

$$w_B = B e^{-i m_B (z - z_b)} e^{-i(kx - \omega t)}. \tag{1.50}$$

For the bottom layer we have one wave travelling upwards and one downwards but with the same vertical wavenumbers such as

$$w_A = \left(A_u e^{i m_A (z_b - z)} + A_d e^{-i m_A (z_b - z)} \right) e^{-i(kx - \omega t)}, \tag{1.51}$$

where A_u and A_d are amplitudes of the upwards travelling original wave and downwards travelling reflected wave respectively, which we can use to substitute reflective index in to the equation since

$$r = \frac{A_d}{A_u} \tag{1.52}$$

and we get

$$w_A = A_u \left(e^{i m_A (z_b - z)} + r e^{-i m_A (z_b - z)} \right) e^{-i(kx - \omega t)}, \tag{1.53}$$

Pressure and density can be calculated using polarization relations we derived before, which we put into impedance boundary condition. This will actually give us reflective index as

$$r = \frac{m_A - m_B}{m_A + m_B}. \tag{1.54}$$

This relationship can be used to derive how much momentum flux and hence energy will continue upwards and how much will be trapped and dissipated in the lower level. We can see, that for the reflection to be minimal we want the maximum possible vertical wave number in the upper level. This means that the maximum is found when $N_B > N_A$ or when the stratification stays the same. In that case the wave continues upward without any loss of energy. Schematic of reflection is in Figure 1.2

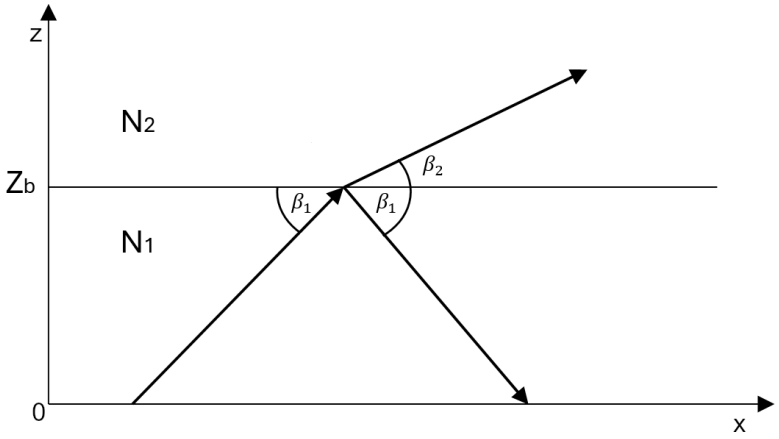

Figure 1.2: Illustration of reflection of a wave on the border of two differently stratified levels.

1.6.2 Resonance

We have seen that it is possible for waves to reflect in case of a sudden change in stratification. We will now analyse more special cases, where waves are trapped in the lower region and or when there is a partial transmission. Specifically, we are interested if the reflection can have any amplification effects on the original wave. Imagine a continuous source of waves, such as mountain. In that case the reflected wave can interfere with the mountain wave which is continuously being created. We can show this using the equation Equation 1.53 together with the boundary condition in Equation 1.27, which leads to the equation for vertical velocity perturbations in the lower layer

$$w_A = u_0 \frac{\mathrm{d}h}{\mathrm{d}x} \left(\frac{e^{im_A(z_b - z)} + re^{-im_A(z_b - z)}}{e^{im_A z_b} + re^{-im_A z_b}} \right) e^{-i(kx - \omega t)}. \tag{1.55}$$

In case of resonance, the amplitude will grow unbounded. It is obvious that the condition for this to happen is that

$$r = -e^{i2m_A z_b}. \tag{1.56}$$

However, we are most interested in cases where $r = 1$ or $r = -1$. We can see that this happens if $m_A z_b = n\pi/2$, where n is a whole number. Then we can get

destructive interference, when n is an even number and $r = -1$, or constructive interference, when n is an odd number and $r = 1$. Generally speaking then, resonance can happen during wave trapping, which inhibits propagation of energy in the vertical direction and so the waves propagate horizontally without loosing their energy. This phenomena is mostly observed with so called lee waves.

We will now analyse the circumstances, when this can actually happen. For this we will look at two dimensionless numbers

$$b = \frac{NL}{U}, F = \frac{NH}{U}, \tag{1.57}$$

where H is the reflecting height and L represents a half-width of an isolated hill and can be connected to horizontal wave number. This is done as

$$k = \frac{2\pi}{\lambda_x} = \frac{2\pi}{4L} \tag{1.58}$$

The first dimensionless number b measures the validity of the hydrostatic approximation [Pierrehumbert, 1986]. This applies for $b >> 1$ or in other words $k << N/U$. However, in that case we can make also approximation that $m = N/U$, which comes from the TGE and assumption that the wind is constant. Now we can see, that our resonance condition for $r = 1$ actually translates to condition for F, which is the inverse Froude number

$$m_a z_b = (2n+1)\frac{\pi}{2} \rightarrow F = \frac{NH}{U} = (2n+1)\frac{\pi}{2}. \tag{1.59}$$

It must be also said, that perfect reflection cannot occur at the boundary of two stably stratified layers, for that would mean, that the vertical wave number m_B in the section above the reflecting level would have to be zero, which is in disagreement with $m_b = N_B/U$. However, if the Froude number is close to our goal value, meaning the reflecting level is at the correct height, there can be partial reflection and in special cases reinforcement of the waves by following reflection of the ground. This can be dangerous as such situations can cause so called downslope windstorms with very high wind speeds as well as vertical accelerations that can cause problems for aviation [Lilly, 1978], [Klemp and Lilly, 1975].

2. GWs in models

In the preceding chapter, we have illustrated how gravity waves and some of their effects emerge from the governing equations. Importance of these effects on real atmospheric dynamics has been thoroughly documented in the literature [Alexander et al., 2010], [Fritts and Alexander, 2020]. However, gravity waves cannot be resolved by GCMs and their effects are parameterized, as was mentioned before. As a motivation for research of OGWs in particular, in this chapter we will review their interaction with resolved dynamics in the models and demonstrate how large their impacts can be based on the current research [Sacha et al., 2021], [Eichinger et al., 2003], [Cohen et al., 2013], [Cohen et al., 2014].

2.1 Representation in models

Importance of OGWs lies in their transport of momentum and energy. Due to Newton's third law the amount of momentum and energy carried by the wave is linked with the conditions at the source level. Particularly, the pressure exerted on the orography by the flow is then equal to the stress propagated away from the orography that causes deceleration once the wave breaks. It has been documented that the drag from OGWs breaking from the troposphere to the upper stratosphere and aloft has significant dynamical effects and hence must be included in GCMs ([Bretherton], [Lilly, 1972]).

In parameterizations, we firstly define base momentum flux, which will be carried by the wave upwards. This momentum flux is estimated using simplified shape of sub-grid scale orography (SSO) and grid scale variables. Propagation of the wave and hence the flux is in models instantaneous and strictly vertical — there is no communication between the neighbouring grid cells. Deposition of this momentum in a form of drag is in parameterizations controlled by the saturation hypothesis. It says that there is some maximum amount of momentum that can be carried by the wave through the background flow without the wave breaking at the level. If the momentum flux is larger than this saturation value, abundance of the momentum is released to the surrounding air masses as the drag and rest of the momentum is carried upwards by the diminished wave. Based on the linear wave theory we can estimate this saturation momentum flux

$$\tau_s = \frac{\rho U^3 \alpha}{N}, \tag{2.1}$$

as shown in [Pierrehumbert, 1986]. Shape of the mountain is considered by dimensionless constant α, which is of an order of unity. It is clear from the equation that the saturation flux is determined by a ratio of density, which is exponentially decreasing with the altitude, and by the third power of the wind speed. If we look at the climatological values of wind in northern hemisphere winter in Figure 2.1 we can see that in the mid-latitudes up to about approximately 100 hPa (lower stratosphere) the winds are growing from the surface to the core of the upper tropospheric - lower stratospheric (UTLS) jet. Above the jet, the winds decrease and so does the saturation momentum flux. At that point, we expect breaking of OGWs and drag deposition. Illustrative focus on mid-latitudes is reasonable

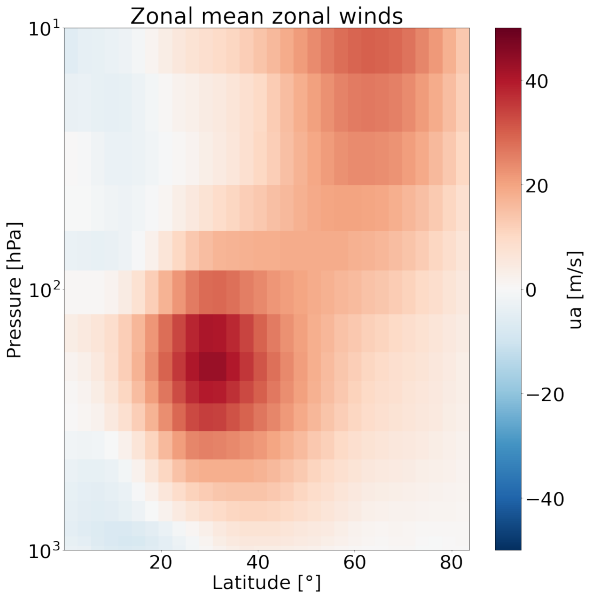

Figure 2.1: Zonal mean zonal wind, winters of 1980-2010, average taken from 14 CMIP6 models

due to the location of the main orographic features on our planet and hence also OGWs in these regions in both hemispheres.

In practical implementation, both base momentum flux and saturation flux are controlled by tunable parameters in the parameterizations, which tend to be tuned differently for each model. There can be several different free parameters, depending on the used parameterization scheme. Usually inverse Froude number is used in the basic form of every parameterizations to define both base and saturation momentum flux, as its critical value indicates breaking of the waves by the so called convective overturning. This instability happens when the amplitude grows too much and causes dense fluid to overly less dense fluid [Sutherland, 2010].

The ability to control and adjust the amount of drag in a model is especially important for climate-modelling centers for adjusting the model biases. Due to the tuning, the parameterized drag does not necessarily reflect the values that would occur in the reality, but rather works as a tool for removing biases in a model. For example, if the model has positive bias of wind speed in the lower stratosphere, we can adjust the critical Froude number to get more drag here, which decelerates the wind speeds towards observational climatology. This would not be as problematic, if the only affected part of the atmosphere were the winds alone. However, it has been shown, that differences in orographic gravity wave drag (OGWD) have large impact on resolved wave driving in models e.g. in [Sacha et al., 2021], [Eichinger et al., 2003]. This is due to the fact, that the location of maximum of OGWD in the so-called valve layer [Kruse et al., 2016] is strategic for controlling the propagation of planetary waves from the troposphere to stratosphere [Wu and Reichler, 2020]. These waves in turn control the resolved dynamics in the models.

2.2 Interaction with resolved waves

In this subchapter, we use CMIP6 data to demonstrate the relationship between parameterized OGWD and the resolved waves. CMIP6 project includes large number of participating models and many different prescribed scenarios for simulations. Here we will use data from 13 models, which include up to 49 different realisations depending on the availability (details in Table A.1). We are interested in several variables and to represent OGWD we will use *utendogw* - tendency of eastward wind due to orographic gravity wave drag. To represent resolved waves, we will adopt classical approach of using Eliassen-Palm flux (EPF) and its divergence, [Andrews et al., 1987]. CMIP6 datasets were chosen, because our previous research showed large differences between OGWD in the models [Hájková, 2022] and we will now broaden this analysis in the following. Figure 2.2 illustrates the intermodel differences on zonal mean OGWD in the lower stratosphere for all the available simulations.

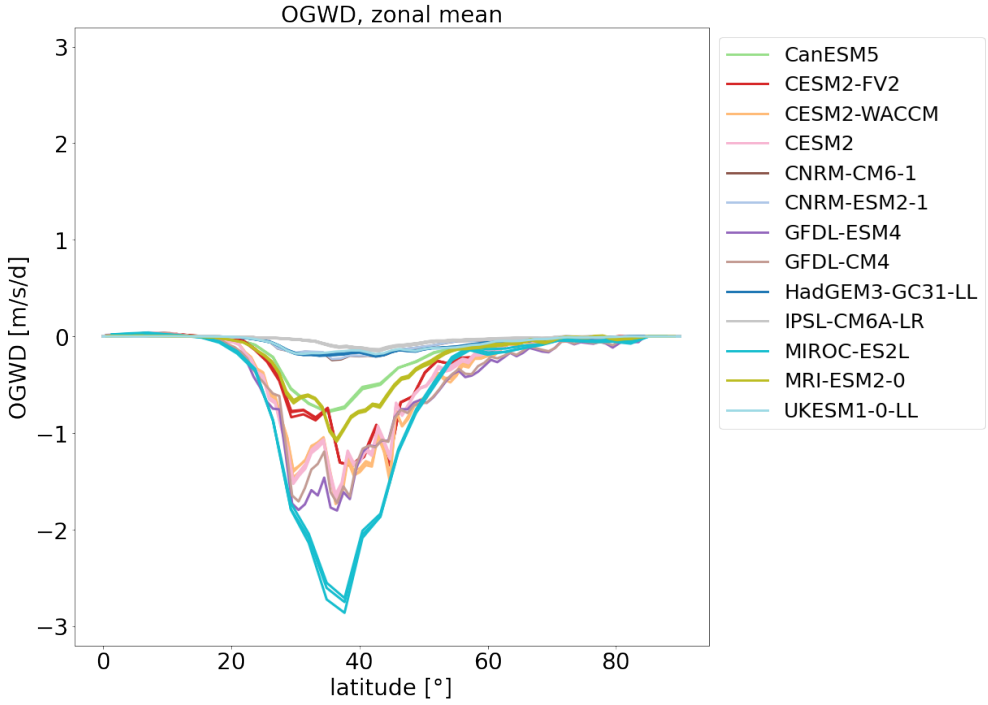

Figure 2.2: Zonal mean of OGWD, average over 100 hPa - 50 hPa, winter season, northern hemisphere

2.2.1 Theory of Eliassen-Palm flux

We will now briefly introduce the theory behind EPF. Following [Andrews et al., 1987] and [Andrews and McIntyre, 1976], we will show that by using transformed eularian mean equations.

In contrast to our previous analysis, we are now at large, planetary scales, which means that the rotational effects are not neglectable. For reducing the complexity of the system of governing equations, we will limit ourselves to the so called quasi-geostrophic approximation on a β-plane. This approximation

assumes only small deviations from the geostrophic balance, which means a dominant balance between the pressure gradient and Coriolis force, which we will decompose as $\vec{f} = f_0 + \beta\vec{y}$, where $\vec{y}$ is a unit vector in the y direction. This way we include the spherical shape of the Earth and the meridional gradient of the Coriolis parameter, without using spherical coordinates.

As detailed in [Andrews et al., 1987], several assumptions underlie this approximation to restrict us to planetary scale motions. We define a Rossby number

$$Ro = \frac{U}{fL}, \tag{2.2}$$

where L is the typical horizontal scale at which we expect changes in wind speed. For small Rossby numbers, the rotational effects are strong and our approximations are valid. Other assumptions are: slow changes of the wind field compared to f_0, small change of Coriolis force on our scale lengths $\beta L << f_0$ and small friction, which is insured by condition

$$|X|, |Y| << f_0/U, \tag{2.3}$$

where X and Y represent non-conservative processes, which will appear in our governing equations.

Continuing with our quasi-geostrophic approximation, we will decompose the wind components to geostrophic and ageostrophic components

$$u = u_g + u_a, v = v_g + v_a, w = w_g. \tag{2.4}$$

Using this and our conditions as defined before we get set of governing equations similarly to Equation 1.3

$$\frac{D_g u_g}{Dt} - f_0 v_a - \beta y v_g = X, \tag{2.5a}$$

$$\frac{D_g v_g}{Dt} + f_0 u_a + \beta y u_g = Y, \tag{2.5b}$$

$$\frac{\partial u_a}{\partial x} + \frac{\partial v_a}{\partial y} + \frac{1}{\rho_0}\frac{\partial \rho_0 w_a}{\partial z} = 0 \tag{2.5c}$$

$$\frac{D_g \theta_d}{Dt} + w_a \frac{\partial \theta_0}{\partial z} = Q, \tag{2.5d}$$

where θ_d is a small departure from the base state potential temperature, such that the vertical derivative of θ can be replaced by that of θ_0. Q represents diabatic heating and material derivative is defined as

$$\frac{D_g}{Dt} = \frac{\partial}{\partial} + u_g\frac{\partial}{\partial x} + v_g\frac{\partial}{\partial y}. \tag{2.6}$$

We now have a way to describe large planetary scales motions. However, similarly as with gravity waves, we would like to know, how the disturbances, meaning planetary waves, interact with the mean flow. In this case, we take mean as a zonal mean and denote by the overbar. We will then decompose all variables to the zonal mean and disturbances and get new set of equations

$$\frac{\partial \overline{u}}{\partial t} - f_0 \overline{v_a} - \overline{X} = -\frac{\partial \overline{u'v'}}{\partial y}, \tag{2.7a}$$

$$\frac{\partial \overline{v_a}}{\partial y} + \frac{1}{\rho_0}\frac{\partial \rho_0 \overline{w_a}}{\partial z} = 0, \tag{2.7b}$$

$$\frac{\partial \overline{\theta}}{\partial t} + \overline{w_a}\frac{\overline{\theta_0}}{\partial z} - \overline{Q} = -\frac{\partial \overline{v'\theta'}}{\partial z}. \tag{2.7c}$$

We dropped the index g, for clarity, as well as Equation 2.5b, because in zonal mean the meridional geostrophic wind is zero and this equation will not be needed in further analysis. Similarly, we also omit the thermal wind equation [Andrews et al., 1987], which would be needed for a full set, as we will not refer to it later.

From these equations we now can see, how the mean flow can change due to the disturbances — eddies — caused by the waves. However, to see effect of this eddy forcing more clearly, we can finally use the transformed eularian mean equations. For this, we have to define so called residual mean meridional circulation for quasi geostrophic beta-plane. We define it as

$$\overline{v}^* = \overline{v_a} - \frac{1}{\rho_0}\left(\frac{\rho \overline{v'\theta'}}{\theta_{0z}}\right)_z, \tag{2.8a}$$

$$\overline{w}^* = \overline{w_a} + \left(\frac{\overline{v'\theta'}}{\theta_{0z}}\right)_y, \tag{2.8b}$$

where the indices denote derivative in this direction.

As we can see, the residual mean circulation is the sum of eularian mean and the wave driven parts. This form is especially useful because it will give us a new set, the transformed eulerian mean equations

$$\overline{u}_t - f_0 \overline{v}^* - \overline{X} = \frac{1}{\rho_0}\left(-(\rho_0 \overline{u'v'})_y + \left(\rho_0 f_0 \frac{\overline{v'\theta'}}{\theta_{0z}}\right)_z\right), \tag{2.9a}$$

$$\overline{v}^*_y + \frac{1}{\rho_0}(\rho_0 \overline{w}^*)_z = 0, \tag{2.9b}$$

$$\overline{\theta}_t + \overline{w}^* \theta_{0z} - \overline{Q} = 0. \tag{2.9c}$$

The largest difference from Equation 2.7 is that the eddies do not figure in the equations alone, but rather in tandem. The right hand side of the Equation 2.9a is the divergence of our wanted Eliassen-Palm flux $\mathbf{F}$

$$\nabla \cdot \mathbf{F} = \left(-(\rho_0 \overline{u'v'})_y + \left(\rho_0 f_0 \frac{\overline{v'\theta'}}{\theta_{0z}}\right)_z\right), \tag{2.10}$$

with components defined as

$$\mathbf{F} = \left(0, -\rho_0 \overline{u'v'}, \rho_0 f_0 \frac{\overline{v'\theta'}}{\theta_{0z}}\right). \tag{2.11}$$

Importance of EPF lies in its dependence on wave characteristics. In case of steady, linear waves and only conservative forces [Eliassen and E., 1961], [Andrews and McIntyre, 1976], we get

$$\nabla \cdot \mathbf{F} = 0. \tag{2.12}$$

This means that EPF divergence is equal to zero, if there is no dissipation of the planetary waves. Allowing non-conservative effects of the waves, represented by D and changing of wave amplitudes in time we get so called generalised Eliassen-Palm theorem

$$\frac{\partial A}{\partial t} + \nabla \cdot \mathbf{F} = D + O(a^3), \tag{2.13}$$

where A is wave activity density representing changes of the wave amplitude a. This theorem shows the clear dependence of the EPF divergence on the wave characteristics and their effects, and subsequently that steady, linear waves do not change the mean flow.

Based on this, we can look at the components of the EPF vector to analyse the wave activity and at its divergence to analyse breaking of these waves and their effect on the mean flow.

2.2.2 Resolved and parameterized drag in CMIP6 models

After illustrating the methodology for analysis of wave-mean flow interaction in the atmosphere and hence also in the models, we use it to analyse the relationship between the resolved and parameterised wave drag. [Cohen et al., 2013] found in an idealized GCM, that there is a compensation between resolved and parameterized drag in the stratosphere. Perturbations to OGWD cause changes of opposite sign in the drag by resolved waves. Specifically, stronger parameterized drag results in weaker resolved one and the other way around. It is argued that this helps to mitigate the uncertainty connected with the parameterized drag, as there are relatively much smaller changes in the net wave driving. [Cohen et al., 2014] showed, that beside compensation mechanism, there can be also inverted relationship, where increasing parameterized drag can cause amplification of the resolved wave driving.

This process is traced to happen via changes to the so called surf zone. This zone can be found in midlatitude stratosphere and is defined by strong mixing of potential vorticity, q, caused by planetary waves. This surf zone encompasses polar vortex, which in contrast has strong gradients of q on its border with the zone. Strong wave activity and breaking at the boundaries can broaden and shift the border of this mixed potential vorticity area poleward (shrinking the polar vortex) [McIntyre and Palmer, 1984]. Breaking of GWs in this area also causes mixing of q. Depending on the location of the breaking in respect to the edge of the surf zone, [Cohen et al., 2014] showed that it can cause either the expected compensation mechanism or an amplification of the resolved wave driving.

[Eichinger et al., 2003] and [Sacha et al., 2021] argued that the interaction between resolved and unresolved dynamics is dominated by modification of resolved wave propagation through the changes of lower stratospheric refractive index, n_s^2. This index describes how easy it is for planetary waves to propagate through some specific region. We expect waves to propagate easily in regions where $n_s^2 > 0$ and avoid areas where $n_s^2 < 0$ [Andrews et al., 1987]. We will derive the definition of this index later.

Although the influence of the parameterized drag on resolved waves has been established before, it was mostly done on either idealized GCMs or on, albeit fully comprehensive, only individual models. We will now use the CMIP6 datasets and

perform a multi model analysis. We are limited by the availability in the case of EPF data (details in Table A.1). For some vertical levels, we can calculate the missing variables, however, we are unable to rely on the calculated data from 100 hPa upwards in some cases. This is due to the coarse vertical resolution of the input variables. Calculations are done using freely available software by [Jucker and rjaiser, 2023] with scaling of EPF terms done as in [Jucker, 2021].

Following analysis updates the results of [Hájková and Šácha, 2024], as we include multiple realisations and more models. We will take a look at EPF divergence to asses if we can further confirm or disprove the compensation and or amplification effect. For this analysis we will only use data available from the CMIP6 database already prepared as outputs from the models. This limits us to 8 different models and 21 realisations. In Figure 2.3 we can see two scatter plots, each for a region with different dynamical regime of OGWD influence on the resolved wave field revealed by [Hájková and Šácha, 2024]. For both regions we calculated the Pearson coefficient to describe the correlation and p-value to show the statistical significance. First plot a) shows OGWD taken over maximum in midlatitudes in the lower stratosphere and EPF divergence taken southward from it. The analysis reveals a strong and statistically significant negative correlation between the parameterized and resolved drag. This is a manifestation of the well known compensation mechanism, with stronger parameterized drag suppressing equatorward propagation of planetary waves from the troposphere to the stratosphere. However, when we look at the Eliassen-Palm flux divergence (EPFD) poleward, we can see clear inversion of this relationship. This points towards the amplification of the resolved wave breaking. This was already showed in [Hájková and Šácha, 2024] and we confirm here the robustness of this interaction using multiple realisations. Such a strong relationship is quite unexpected, especially since the relationships are not in fact linear, as we can see from differences between realisations of one model.

This relationship between OGWD in the valve layer and the resolved dynamics can be predominantly explained by modulation of resolved wave propagation by OGWD. For this, we calculate the refractive index as in [Andrews et al., 1987], demonstrating the influence on the propagation of leading planetary wave modes. Definition of the refractive index is as follows

$$n_s^2 = \frac{\overline{q_\phi}}{\overline{u}} - \frac{s^2}{a^2 \cos\phi^2} - \frac{f^2}{N^2 H_s^2}, \tag{2.14}$$

where $\overline{q_\phi}$ is the meridional gradient of the zonal mean potential vorticity, in spherical coordinates defined as

$$\overline{q_\phi} = 2\Omega \cos\phi - \left[\frac{(\overline{u}\cos\phi)_\phi}{a\cos\phi}\right]_\phi - \frac{a}{\rho_0}\left(\frac{\rho_0 f^2}{N^2}\overline{u}_z\right)_z. \tag{2.15}$$

In both equations a is the radius of the spherical Earth and s is a zonal wave number usually taken between $1-3$.

Since data for calculation of refractive index were available for the full set of models, the refractive index is presented for all 13 models and 49 realisations. In Figure 2.4 we are showing the refractive index taken as a mean over all simulations. In the lower stratosphere, above the midlatitudes, we can see an area of smaller refractive index where large scale waves are inhibited to propagate. This

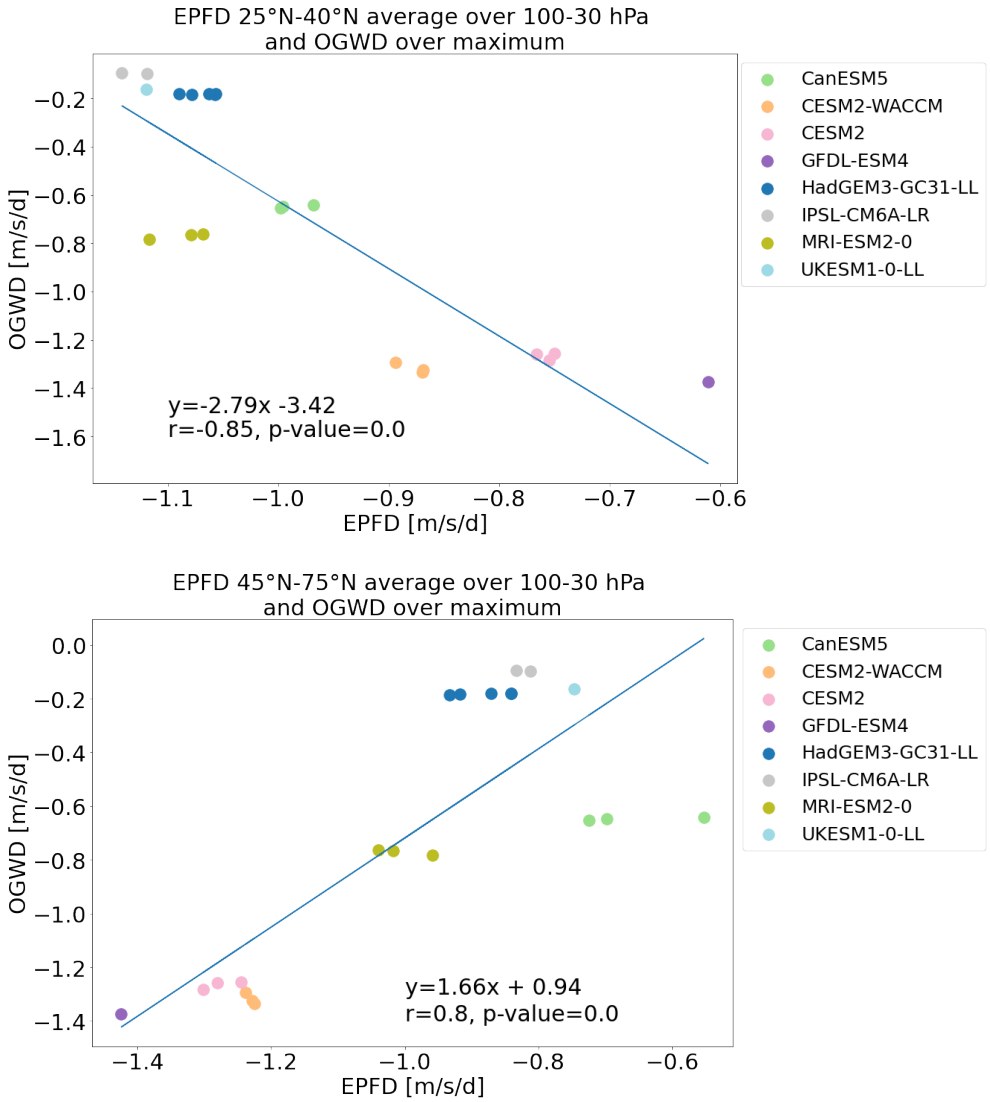

Figure 2.3: Scatter plots of OGWD and EPF divergence (EPFD), OGWD taken over maximum (30° - 45 °, 100-50 hPa), EPFD taken over latitudes as described

is the so-called valve region and our area of interest is indicated by the black border. In the tropics, the index looses physical meaning and is traditionally not used. Near the pole we can see a sharp drop towards negative values. Inside the polar vortex, vertical wave propagation is often inhibited. We again repeat the intermodel correlations analysis and show the scatter plots for RI in Figure 2.5. This specific domains for averaging the RI values were chosen according to [Wu and Reichler, 2020], capturing the most important area for propagation of planetary waves from troposphere to stratosphere. Once again, we can see pronounced strong correlation between the OGWD and the refractive index leading to modulation of the planetary waves propagation. We can clearly see, that larger values of the drag from parameterized waves inhibit propagation of the planetary waves in the UTLS jet region.

Similarly to EPFD, we can be interested if the influence of OGWD on the refractive index does reach higher latitudes, nearer to the polar vortex. Although the relationship is not nearly as strong there, it is still significant and we can see, that there is quite clear inversion of it. This shows that differences in circulation

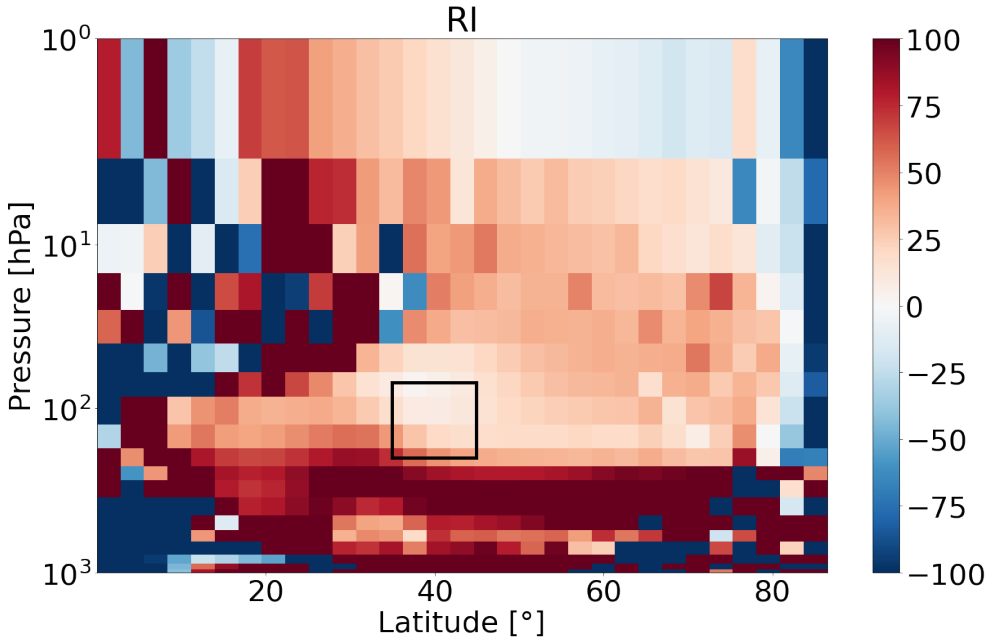

Figure 2.4: Refractive index, northern hemisphere, mean over all realisations.

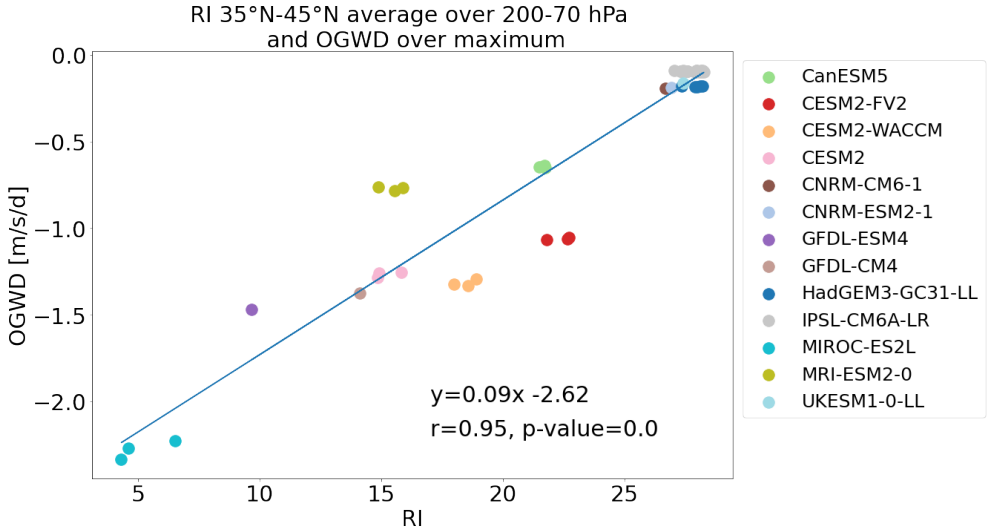

Figure 2.5: Scatter plot of OGWD and the refractive index, OGWD taken over maximum (30° - 45 °, 100-50 hPa), RI taken over and vertical levels as described

as well as the resolved dynamics caused by OGWD can influence far away regions and do not have only localised effects.

The relationship between the parameterized drag and resolved waves can be however more complicated. We are also interested in how near surface OGWD can influence the planetary wave activity in the troposphere and how the waves then possibly influence the resulting OGWD in the lower stratosphere. We will again repeat our scatter plot analysis, but this time we will look at near surface OGWD and at vertical component of EPF above, in Figure 2.7. We must be careful, when looking at the near surface OGWD data, because [Hájková and Šácha, 2024] warned about possibility that there are missing values concerning low-level breaking. This is however in accordance with what we see in Figure 2.7. Models

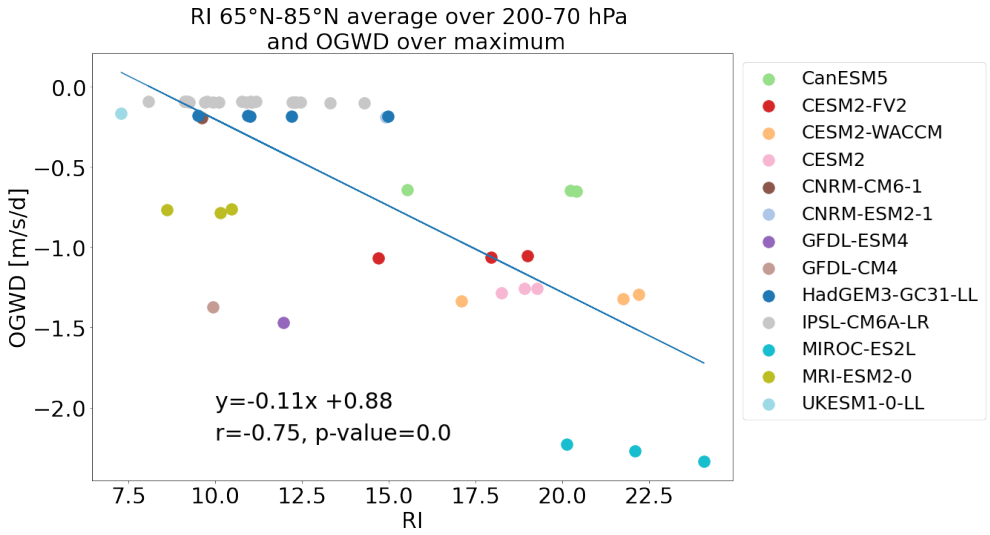

Figure 2.6: Scatter plot of OGWD and the refractive index, OGWD taken over maximum (30° - 45 °, 100-50 hPa), RI taken over and vertical levels as described

HadGEM3-GC31-LL and UKESM1-0-LL, which fall the most out of the found relationship are actually the specific models that were suspected to miss part of the drag. The found relationship, albeit not a strong one, points to amplification

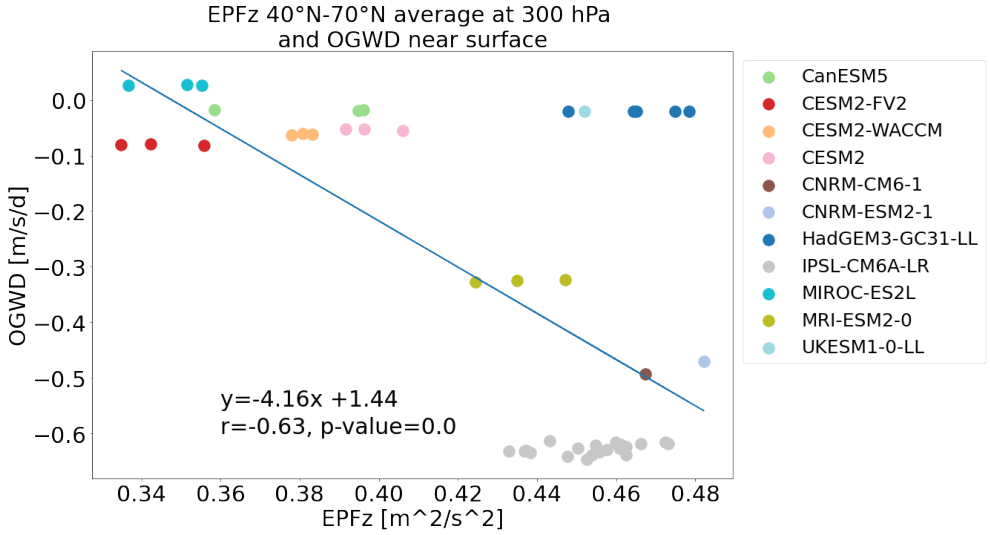

Figure 2.7: Scatter plot of OGWD and the refractive index, OGWD taken over maximum near surface (30° - 45 °, 1000-500 hPa), EPF_z taken over and vertical levels as described

of the wave activity in the troposphere by higher values of OGWD near the surface. In the Appendix, Figure A.1, we show inversion of this relationship when looking at the EPF component at the same location and the drag above in the lower stratospheric maximum. Nevertheless, to properly describe this interaction and correctly define the causality of these effects, further analysis would have to be performed, as there will be influence of other factors such as wind speed for example. All effects described in this section are possibly strongly artificial — found only in models and do not necessary reflect real processes in

the atmosphere. For this reason, more research is needed of GW interaction with Rossby waves and OGW parameterizations should be further improved and their effects more analysed.

The analysis above is shown only for the northern hemisphere for brevity, since the situation is more complicated in the southern hemisphere and generally less studied. Although we can see the same interactions as in NH, the correlations are usually weaker and latitudinally shifted. This is due to slightly different location of the orography there, added drag from the antarctic region and unrealistic OGWD gap between the south America and Antarctic peninsula [McLandress et al., 2012], [Hájková and Šácha, 2024].

3. Simulation of a flow over the hill

In the first part we introduced theoretical background of a flow over some obstacle. We will now use this theory to analyse a set of different idealised simulations of the flow over a hill and we will evaluate the off-line performance of selected OGW parameterizations.

3.1 Model and simulation setup

For our simulations we have used the numerical weather prediction model WRF-ARW [Skamarock et al., 2019]. We have used idealized simulation setup. Main difference between real and idealized cases are the initial conditions. For real cases these are usually data from either observations or from previous runs of a model. For the idealised set-up this is usually only 1D or 2D sounding, with necessary variables — potential temperature, relative humidity and the horizontal wind field. Instead of real orography, we will prescribe the idealised witch of Agnesi hill and Gaussian hill in different versions.

WRF offers several prepared idealised cases, which serve as a basis for more complicated simulations. Some of the cases are for example large eddy simulations, squall line simulations or our chosen setup of flow over a hill called em_hill2d_x. In its base version it is 2D hydrostatic simulation with a single symmetric witch of Agnesi hill of height 100 m. We modified the original setup and performed several simulations based on the work in [Doyle et al., 2011]. We expand the simulation with the Gaussian hill (originally only Agnesi hill was used) and we also run longer simulations.

First two simulations are run in an idealistic (hydrostatic) set-up with a constant wind $U = 10\ m/s$ and a stratification of $N = 0.0196\ s^{-1}$ to test the model. For comparison we use simplistic model ICAR [Gutmann et al., 2016] based on the linear wave theory and an analytical solution which we will now derive. We start with the Witch of Agnesi hill. To calculate the analytical solutions using Equation 1.29 we must firstly define $\hat{h}$. That is

$$\hat{h}(k) = \int_{-\infty}^{\infty} h(x)e^{-ikx}\mathrm{d}x = \int_{-\infty}^{\infty} \frac{Ha^2}{x^2 + a^2}e^{-ikx}\mathrm{d}x = Hae^{-|k|a}\pi. \tag{3.1}$$

We will supply that to Equation 1.29 to get

$$w_1(x, z) = \Re \int_0^{k_m} -iu_0kHae^{-|k|a}e^{-i\sqrt{\frac{N^2}{u_0^2}-k^2}z}e^{-ikx}\mathrm{d}k, \tag{3.2}$$

where vertical wave number m was supplemented accordingly, based on Equation 1.24. We take the same approach to calculate the analytical solution for the Gaussian hill. Fourrier transform will be

$$\hat{h}(k) = \int_{-\infty}^{\infty} He^{\frac{-x^2}{a^2}}e^{-ikx}\mathrm{d}x = Ha\sqrt{\pi}e^{-\frac{k^2a^2}{4}} \tag{3.3}$$

and that gives us

$$w_1(x,z) = \frac{\sqrt{\pi}}{\pi}\Re\int_0^{k_m} -iu_0kHae^{-\frac{k^2a^2}{4}}e^{-i\sqrt{\frac{N^2}{u_0^2}-k^2}z}e^{-ikx}\mathrm{d}k. \tag{3.4}$$

Solutions for w_1 were then calculated numerically using the trapezoidal rule. We also have to include the growth of the amplitude with decreasing density in the vertical. This is done by multiplying the solution by a factor $(\rho_s/\rho_0)^{-1/2}$, where $\rho_0(z)$ is the base state density and ρ_s is the surface density, [Nappo, 2002], [Doyle et al., 2011].

For the idealistic simulations we choose symmetrical hills with height of 100 m and with the parameter, a, describing the slope (half-width) equal to 10 km for the Agnesi hill and 8.3 km for the Gaussian hill. We will call these simulations IdealA and IdealG. The half-width parameter for IdealA was based on the work of [Doyle et al., 2011] and for IdealG it was chosen based on the parameterization schemes we will be using later. We found that by choosing that value, the standard deviation of both of the hills is almost identical for coarse 200 km resolution simulations. This gives us nice inside to how details of the orography can be lost in global models, even when using SSO. More will be explained in the following sections.

For more realistic simulations (using the non-hydrostatic setup) we use vertical profile of the wind given as in [Doyle et al., 2011], that is based on the sounding done in the Sierra Nevada mountains during the T-REX campaign [Grubišić et al., 2008].

In Figure 3.1 we can see the wind and potential temperature profiles used for the simulations. For the numerical stability purposes, the wind was altered to be constant near surface at 5 m/s and to decrease linearly from 18 km to be at zero at 23 km and above. The decrease to zero was done to limit waves from reflecting from the top of the model. The level where the wind speed is equal to zero is called a critical level for OGWs, [Nappo, 2002], and the waves cannot propagate through, causing them to dissipate. This can be seen from the TGE as well, where we get zero in the denominator.

Parameter selection for these simulations is $a = 40$ km on the windward side and $a = 5$ km on the leeward side of the hill for the Agnesi simulations and $a = 40 * 0.83$ km and $a = 5 * 0.83$ km for the Gaussian hills. This means that the Gaussian hill is steeper on both the windward and the leeward side. Simulations were done for hills with height of 1000 m and 2500 m. We will call these simulations A1000, A2500, G1000 and G2500.

To estimate the resulting wave field, we can look at the Brunt-Väisälä frequency and the Scorer parameter. Former will tell us if the atmosphere is stable and supports waves, and will identify points where possible reflection may emerge due to fast changes of the stratification, the latter will tell us what is the maximum horizontal wave number that waves can have to penetrate through the individual levels, as we derived before.

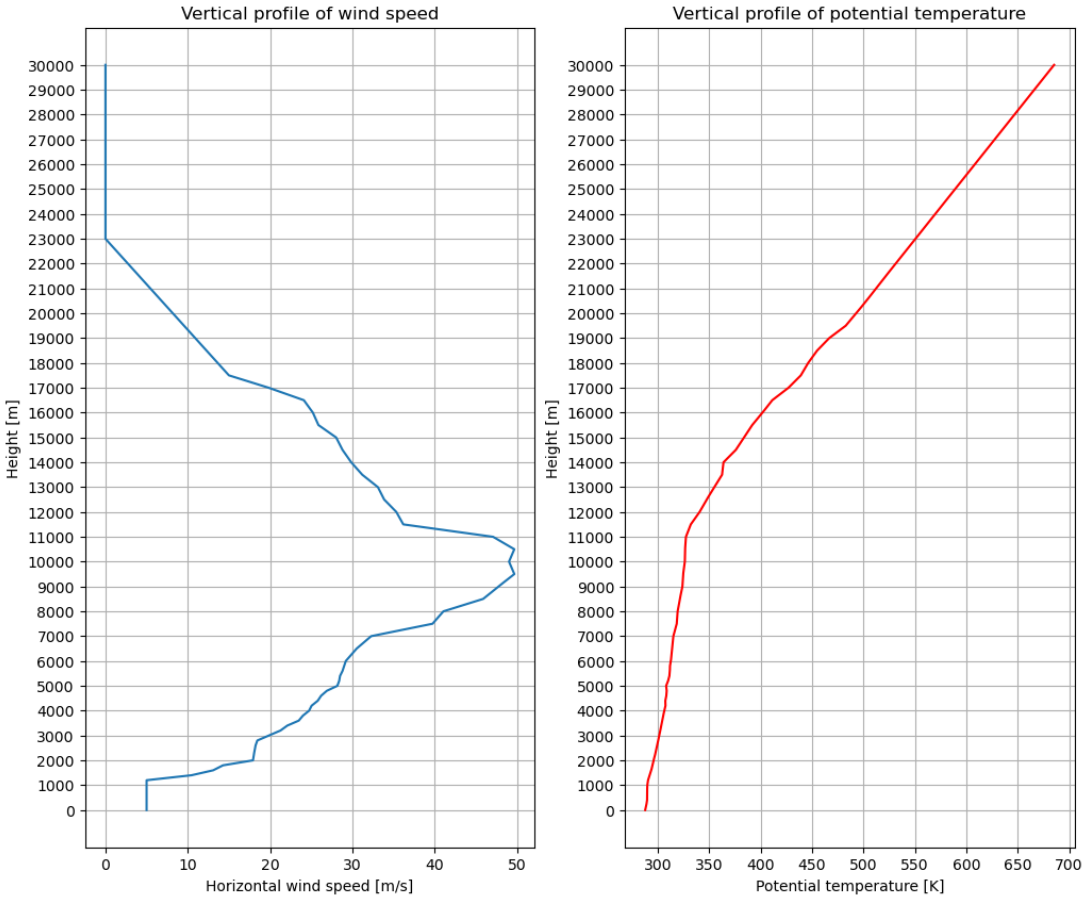

Figure 3.1: Profile of wind and potential temperature used for the non idealistic simulations

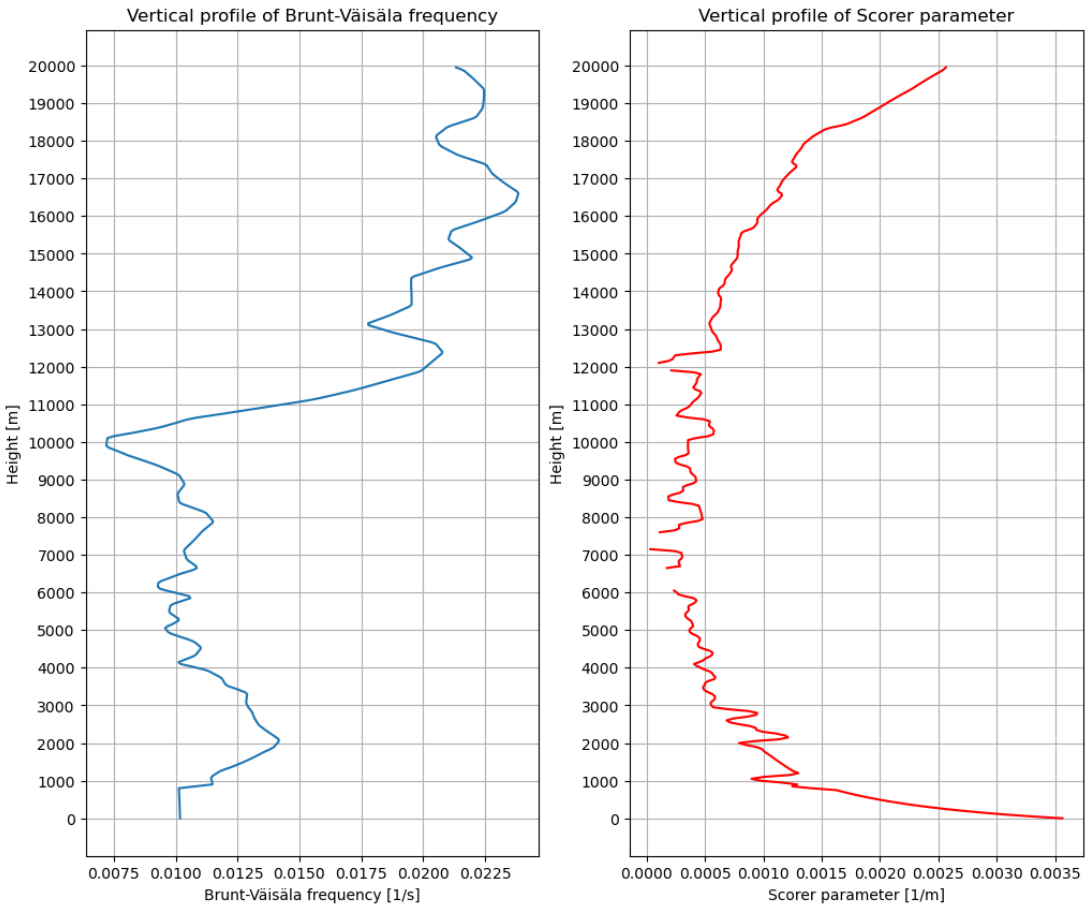

Figure 3.2: Profiles of the Brunt-Väisälä frequency, N, and Scorer parameter, l, for the input sounding, smoothed by rolling average for better visualisation

3.2 Simulations over the Witch of Agnesi and Gaussian hill

We start describing the results of simulations IdealA and IdealB and evaluate WRF against the analytical solutions and linear wave theory based simulations of ICAR. In Figure 3.3 and Figure 3.4 we can see the resulting wave field from the idealized WRF simulations, ICAR and analytic solutions and it is evident that there is in general a very good agreement among them and a vertically propagated wave solution is produced as expected. Due to the constant profile of the wind and Brunt-Väisälä frequency we can see steady hydrostatic waves with a vertical wavelength of

$$\lambda_z = 2\pi \frac{U}{N} \sim 6400m. \tag{3.5}$$

All solutions seem to agree reasonably well regarding the amplitude, with bigger

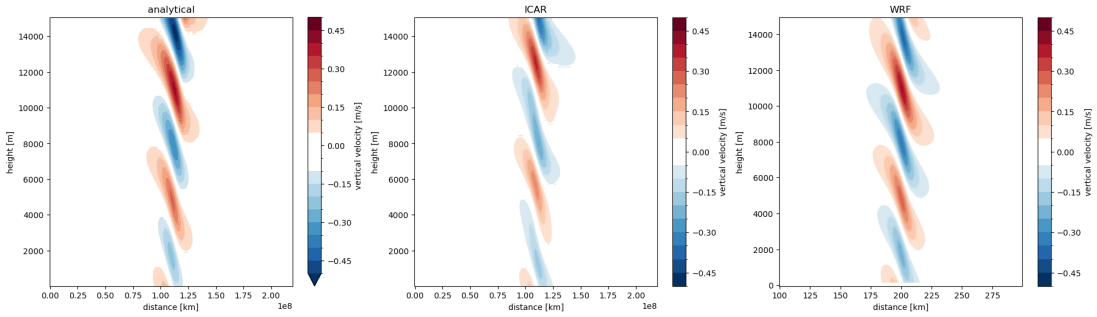

Figure 3.3: IdealA - the wave field above the 100 m Witch of Agnesi hill - the vertical velocity field, 4 hours into the simulation.

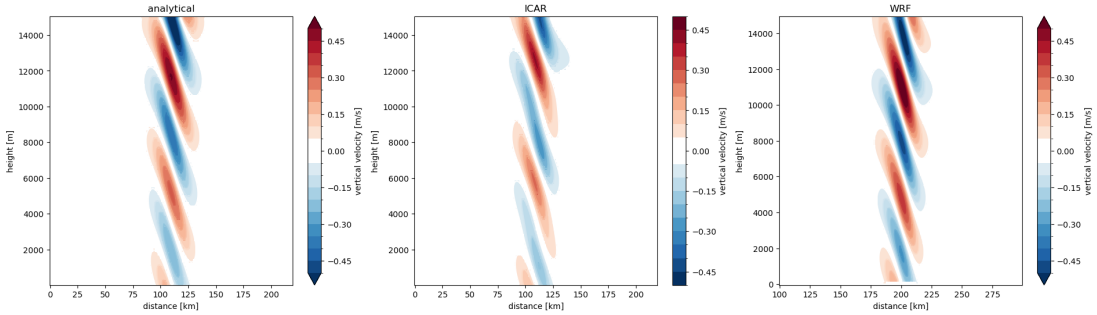

Figure 3.4: IdealB - the wave field above the 100 m Gaussian hill - the vertical velocity field, 4 hours into the simulation.

agreement between analytical and WRF results. ICAR shows slightly weaker vertical velocities as well as a slightly different shape of the windfield itself. We can also notice differences between the simulations for different hills, showing how different shapes can result in differences of the resulting waves independently on the height. Waves above the Gaussian hill reach higher velocities, this is due to the larger slope in comparison to the Witch of Agnesi hill.

After validating the idealistic simulations, we now move towards analyzing the non-linear simulations. We start with replicating Ex1000_fs simulations from [Doyle et al., 2011]. In accordance with the reference, our domain is 400 km large,

with the hill located in the middle. The horizontal resolution is 1 km and there is 150 vertical levels with the top at the altitude of 30 km. In contrast with the original study, we run the simulation for longer time period (24 hours) to see a full time development of the waves. In Figure 3.5 we can see our first try of this simulation, time steps are shown in 2 h. The resulting wind field at 4 hours of the

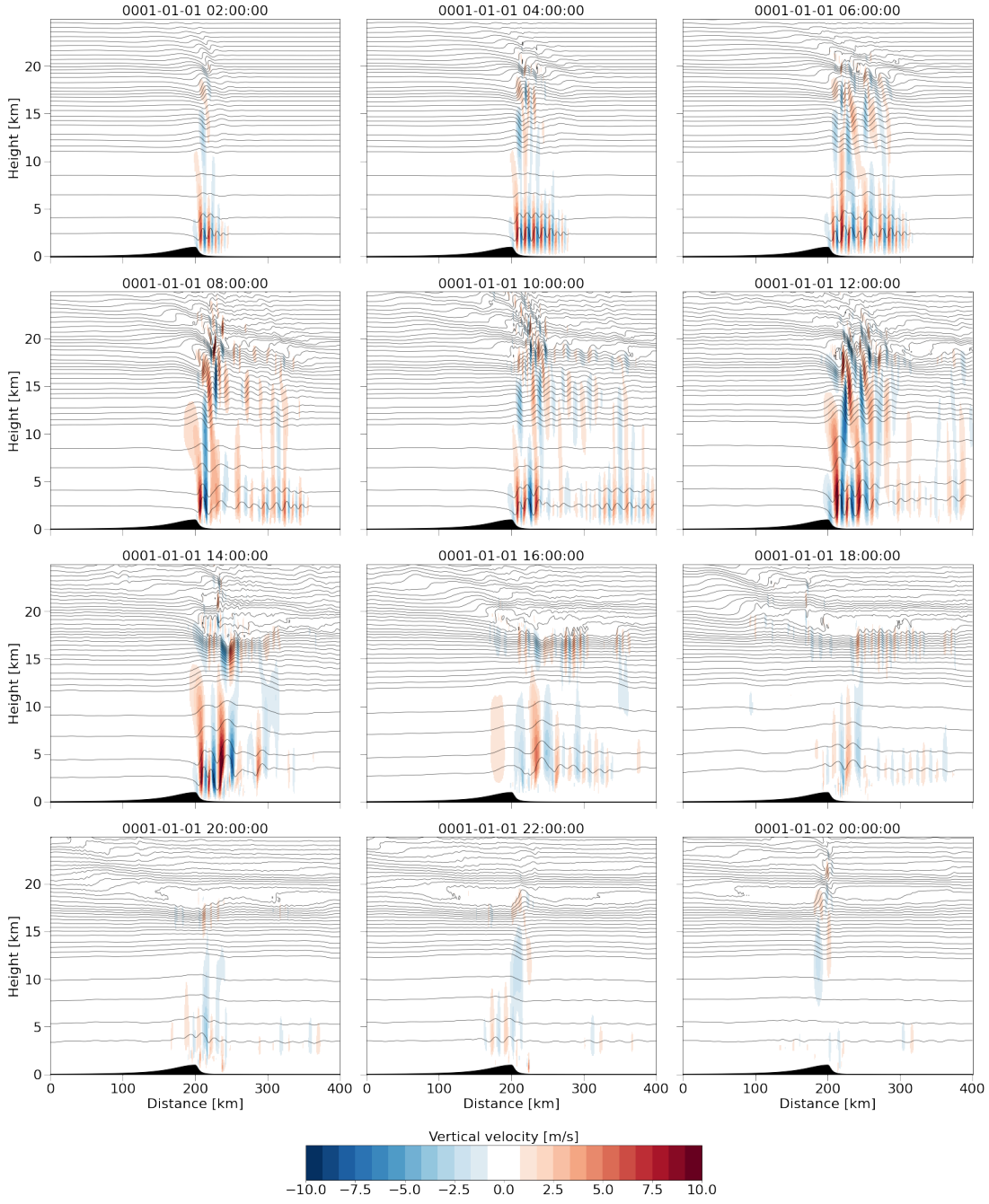

Figure 3.5: A1000 - domain 400 km, 24 hours of simulation.

simulation agrees with the original results of [Doyle et al., 2011], Fig 3. However looking at the further wave field development in later times of the simulation, it is interesting to see the severely decreasing amplitude of the wave modes with progressing simulation. Although the dissipation and resulting drag from the waves feed back on the creation of the waves due to the resulting turbulence

reaching near surface levels, this decreasing tendency seems surprisingly strong here. We found it to be an effect of the lateral boundary conditions, which are open in this simulation as is usual in those cases for the WRF ideal simulations. For those boundary conditions, we can expect possible partial refection, amplified in cases with strong turbulence and wind speeds. We confirmed that by looking at the streamlines of the flow, as in Figure 3.6 Here, we can clearly see a turbulence

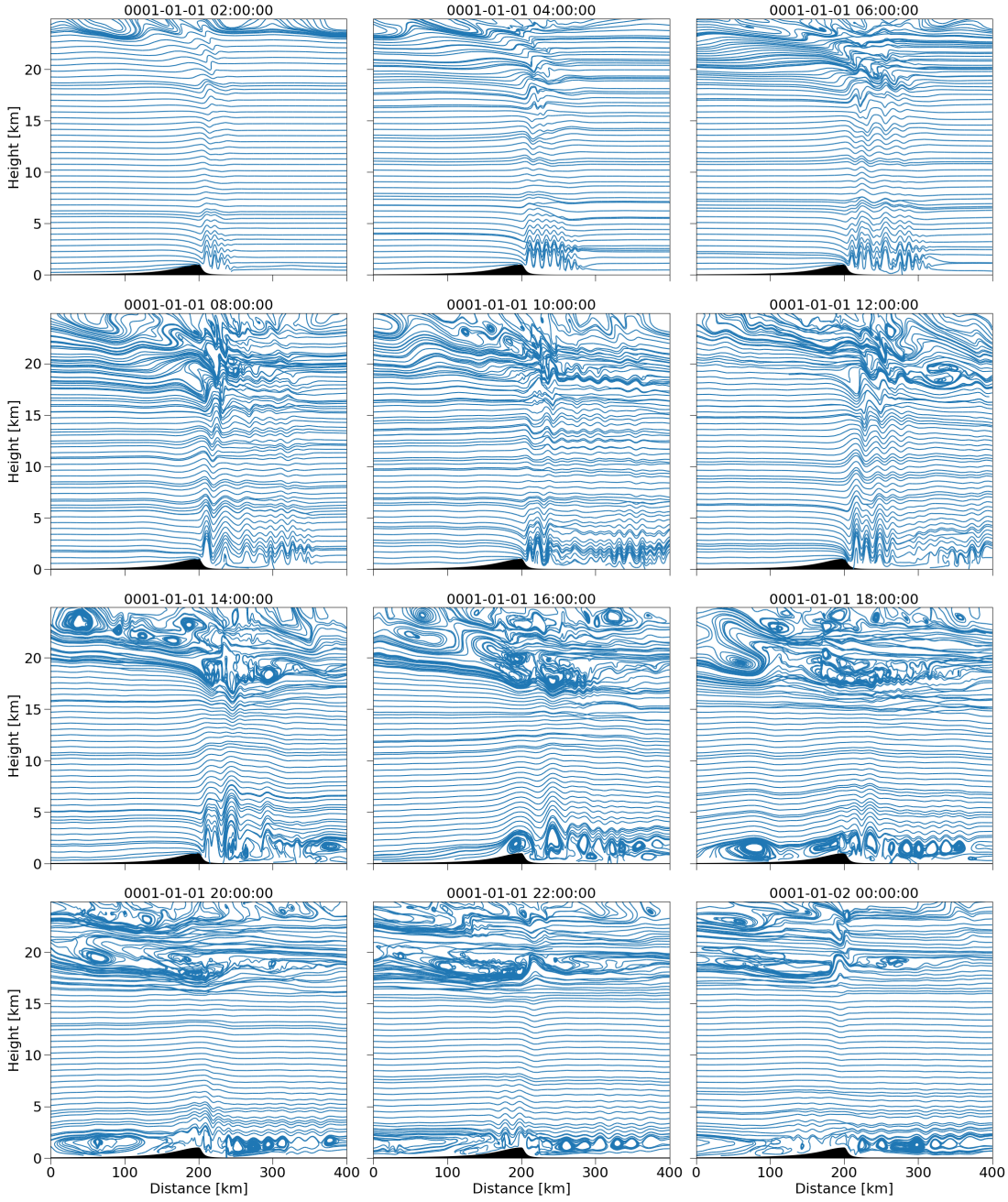

Figure 3.6: A1000 - domain 400 km, 24 hours simulation, streamlines.

in a form of rotors beginning to start at 12 hours of the simulation at the leeward side of the domain boundary and then propagating back to the domain, reaching also the wind facing side of the hill and decreasing the incoming background winds here. Although rotors are not artificial per se in connection to OGWs, the propagation from the boundary is clearly artificial, which confirms the reflection

problem.

To avoid this problem, we enlarged the domain to 800 km with the hill still in the middle, which turned out to be just enough for the length of our simulation, with reflection effects visible at the edge of the domain only by the end of the simulations. However, in cases longer than one day we would have to adapt a new set of boundary conditions to resolve this. Further results shown in the thesis are produced using the wider domain.

We will now look more closely at the simulation A1000 realised on the larger domain in Figure 3.7 focusing on the middle of the domain with the span of 400 km for better visualisation. In the figure, from the start we can clearly see a vertically propagating wave mode and evolving trapped lee waves below ~ 5 km, which are horizontally propagating away from the hill. This is due to the decrease of Scorer parameter which at around 4 km of height starts to decrease below 0.005 m^{-1}. This means that the horizontal wavelengths of the vertically propagating waves must be bigger than 12.5 km according to Equation 1.19,

$$\left(\frac{2\pi}{\lambda_x}\right)^2 = k^2 < l^2 = \frac{N^2}{U} - \frac{U_{zz}}{U} \rightarrow \lambda_x > \frac{2\pi}{0.005} \sim 12.5km. \tag{3.6}$$

Looking closely at the plots, we can see that the horizontal wavelengths of lee-waves are around 10 km, hence they are unable to fully penetrate the levels above. At first amplitudes of the leewaves starts to grow, probably due to the reflection either from the level above or from the ground. Based on looking at smaller time step (not shown), it is possible that after 6 hours of the simulation, the amplitudes grow too large, which leads to instability and breaking. This leads to decreasing amplitude of the vertical velocities at some stages. Also the wave packet propagates horizontally away from the hill.

As noted before, we can also see vertical propagation of waves with larger horizontal wavelengths to the stratosphere, where they start to break already by 4 hours. Breaking of the waves at this altitude is in accordance to the saturation hypothesis. Based on the isolines, we can see regions of unchanging potential temperature. This shows, that the resulting drag leads to slight mixing downwind of the hill in the lower stratosphere and we see it is mostly unchanging in time.

We can now look at the simulation G1000 for comparing the effect of differently shaped hill of the same height. In Figure 3.8 we can see that the simulations are fairly similar to each other in the early stages. The difference between them can be seen after 6 h of the simulation time. While in the case of Agnesi hill it seems that we have rather diminishing of the reflected waves after a while due to instabilities, with the Gaussian hill, there seems to be a resonance effect. The amplitudes and vertical velocities of the lee waves grow, penetrating more easily to the stratosphere, resulting in stronger wave activity altogether. Perturbation to horizontal velocities for both simulations are shown in the Attachment, Figure A.2 and Figure A.3 We will now take a look at the simulations A2500 and G2500, starting with Agnesi hill in Figure 3.9. It should be mentioned that the case of a single mountain with a height of 2500 m above surrounding topography is quite extreme. For this reason, it is not surprising that although we can see formation of large waves in the first time step, there is immediate breaking and overturning in the next. This causes significant downslope winds, with vertical velocities reaching up to 30 m/s. What we see here is so called hydraulic jump, [Doyle and Reynolds, 2008].

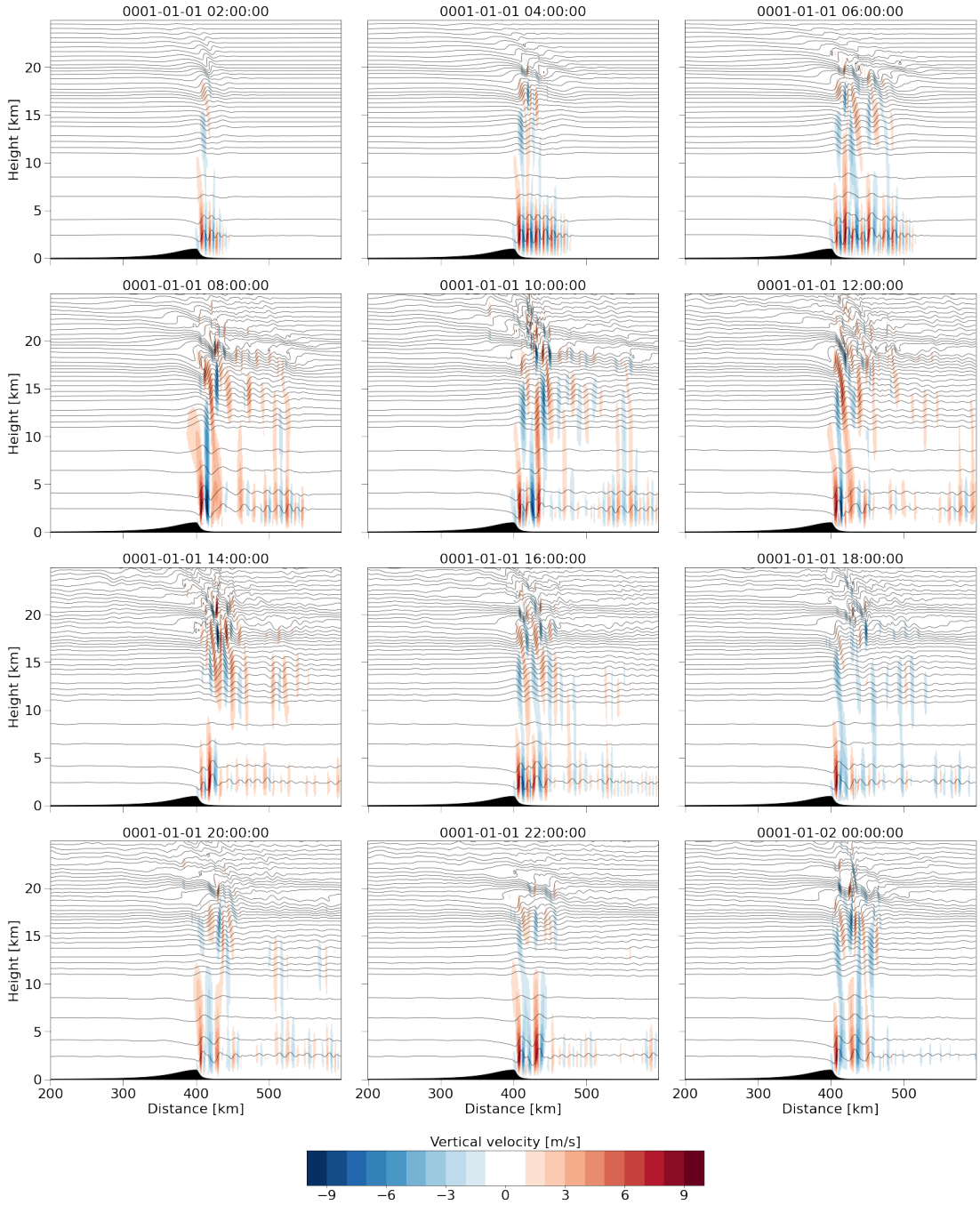

Figure 3.7: A1000 - domain 800 km (400 km showed), 24 hours simulation, vertical velocity. Vertical velocities in color, with black lines as isolines for potential temperature with the interval of 8 K.

In the following time steps we can see propagation of a large mixing area behind the hydraulic jump. This can be seen particularly in Figure 3.10, where we show horizontal wind perturbations. Deceleration in the mixing region reaches up to 50 m/s, causing turning of the flow at some points.

Near surface we can see also overturning due to breaking of the waves. However, it has to be noted that the character of the low-level processes in particular is strongly influenced by the free slip boundary condition, which is a known effect [Doyle and Durran, 2002]

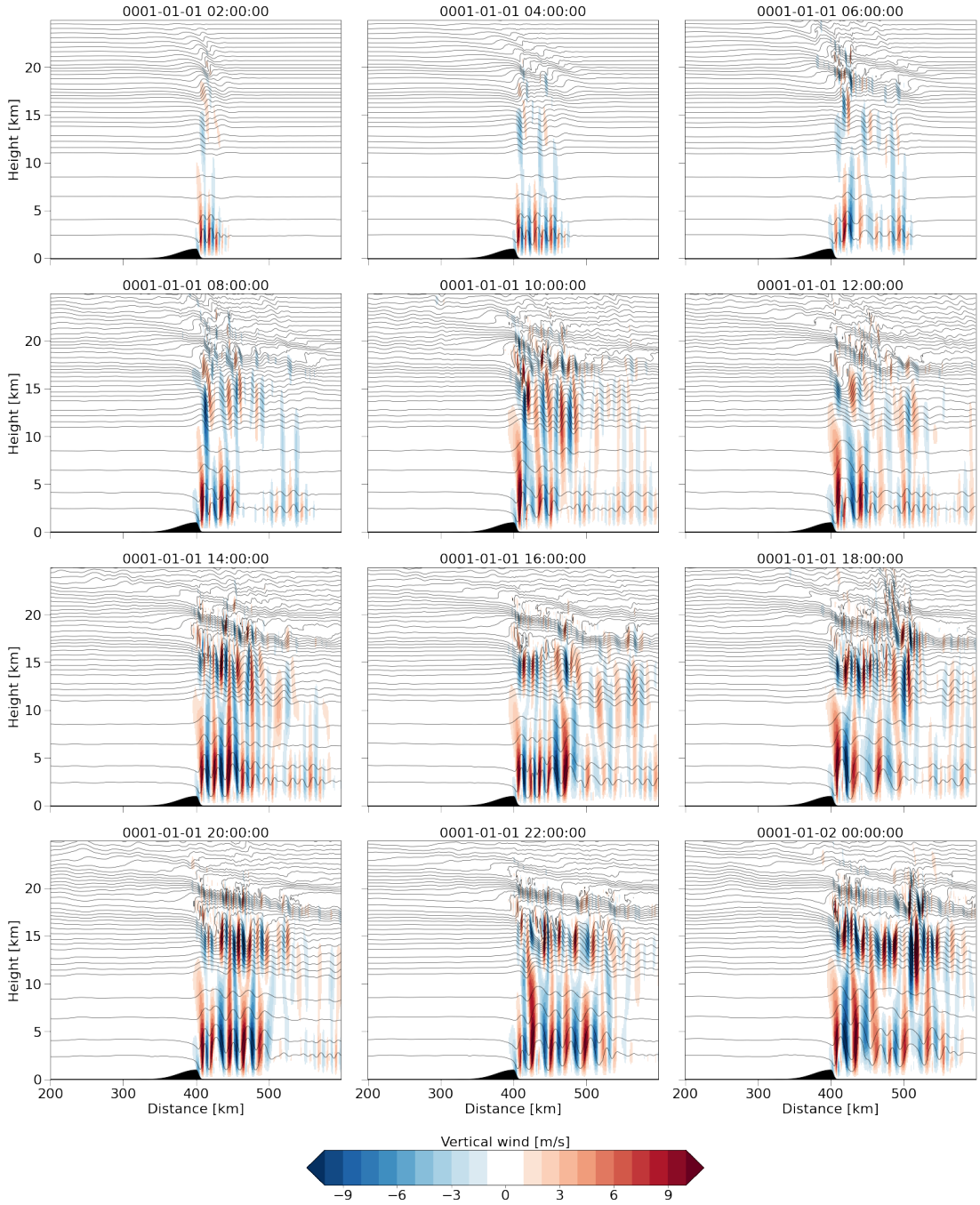

Figure 3.8: G1000 - domain 800 km (400 km showed), 24 hours simulation, vertical velocity.

We will now compare the results of the A2500 simulation with the simulation G2500 shown in Figure 3.11. Since both of these cases are quite extreme, there is less difference between the type of the hills than in 1000 m cases, although we can still see higher vertical velocities for the Gaussian hill, especially along the lee ward slope. There is also difference in the altitude of the lower stratospheric breaking of freely propagating gravity wave modes, more obvious for the last 6 hours of the simulation. For the Gaussian hill, we can see the breaking already at around 15 km of altitude, where in the Agnesi case it is closer to 20 km.

In the simulations we did see many non-linear effects connected to OGW

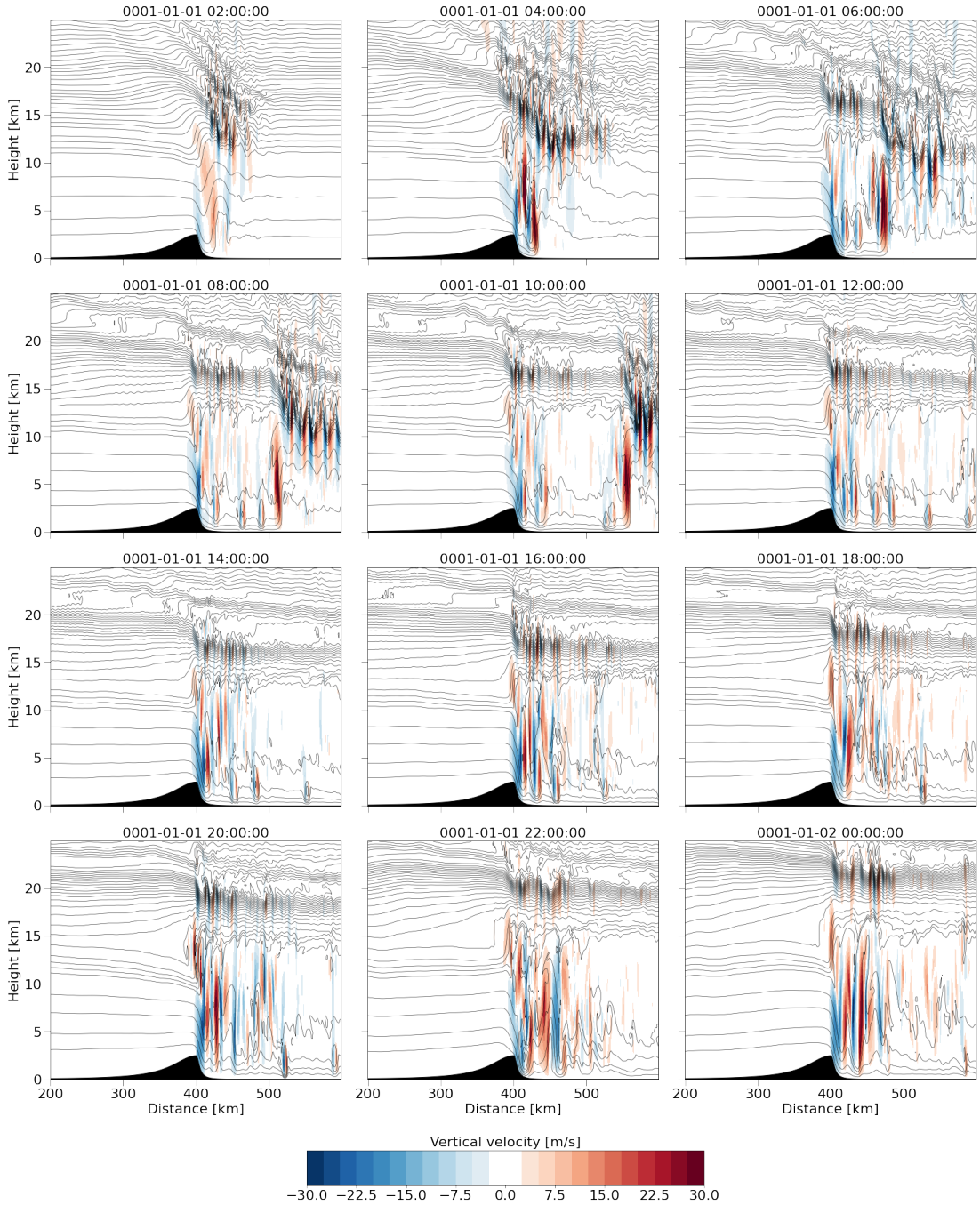

Figure 3.9: A2500 - domain 800 km (400 km showed), 24 hours simulation, vertical velocity.

propagation, breaking and resulting drag. These phenomena, of course, cannot be resolved by the coarse resolution GCMs and the question is if the parameterizations supplement the resulting drag accurately. With the aim of comparing the off-line performance of selected OGW parameterizations in these cases, we will calculate the momentum flux and drag from our WRF simulations in the following way

$$\tau_x = \rho_0 \overline{u_1 w_1}, \tag{3.7}$$

where all variables have been defined before and with a basic state u_0 and w_0 taken as average over the time and the domain. The resulting drag is calculated

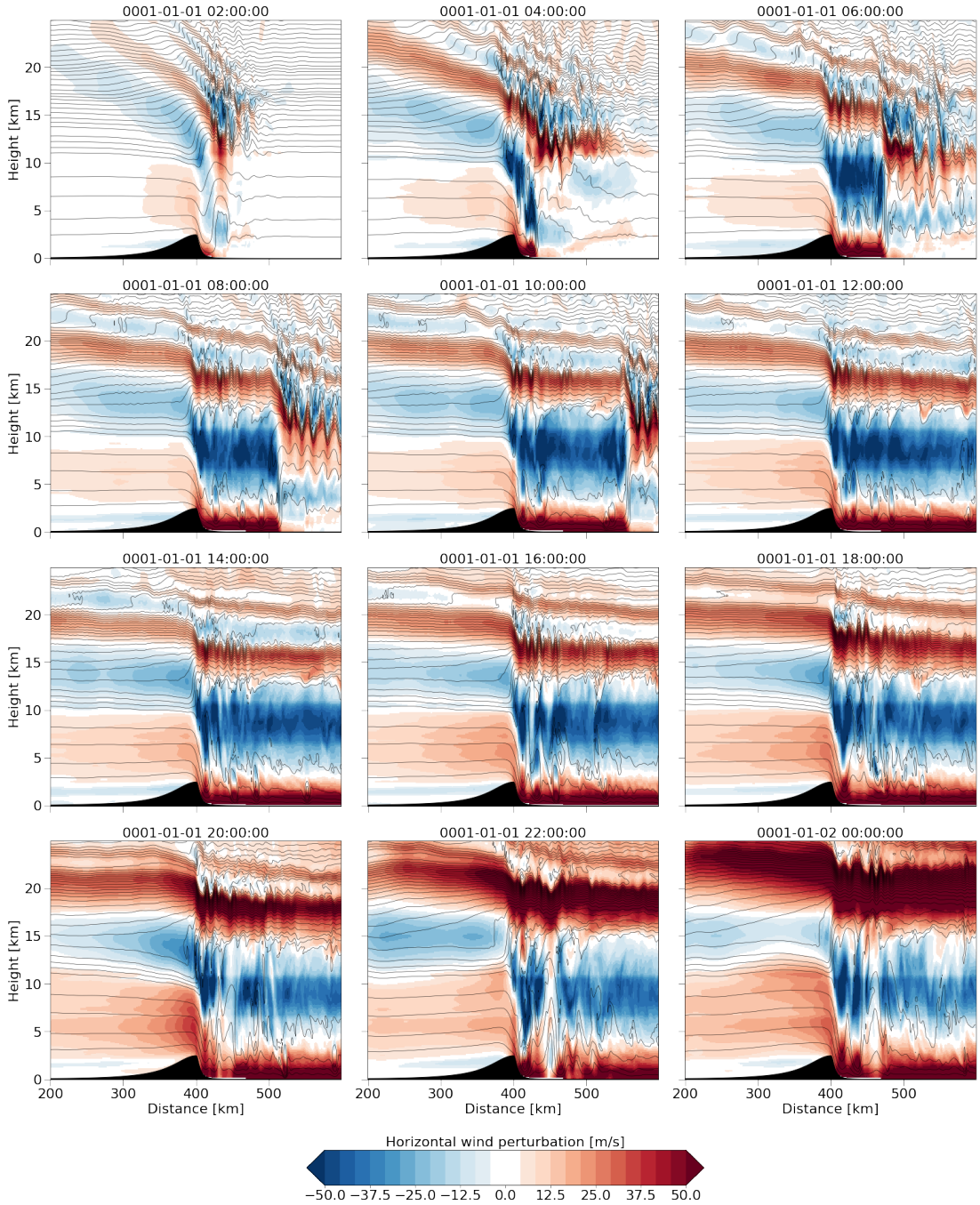

Figure 3.10: A2500 - domain 800 km (400 km showed), 24 hours simulation, horizontal wind perturbations.

as

$$OGWD = -\frac{1}{\rho_0}\frac{\partial \tau_x}{\partial z}, \tag{3.8}$$

as shown in [Hájková, 2022]. The resulting drag averaged over the whole simulation time is shown in Figure 3.12. For the 1000 m hills we see 2 clear regions of breaking. One near surface and one in the lower stratosphere. This is quite in accordance with our expectations. We also see larger amounts of drag for the Gaussian hill, which agrees with our observation of stronger wave activity and turbulence in these simulations. In the case of 2500 m hills, we see continuous

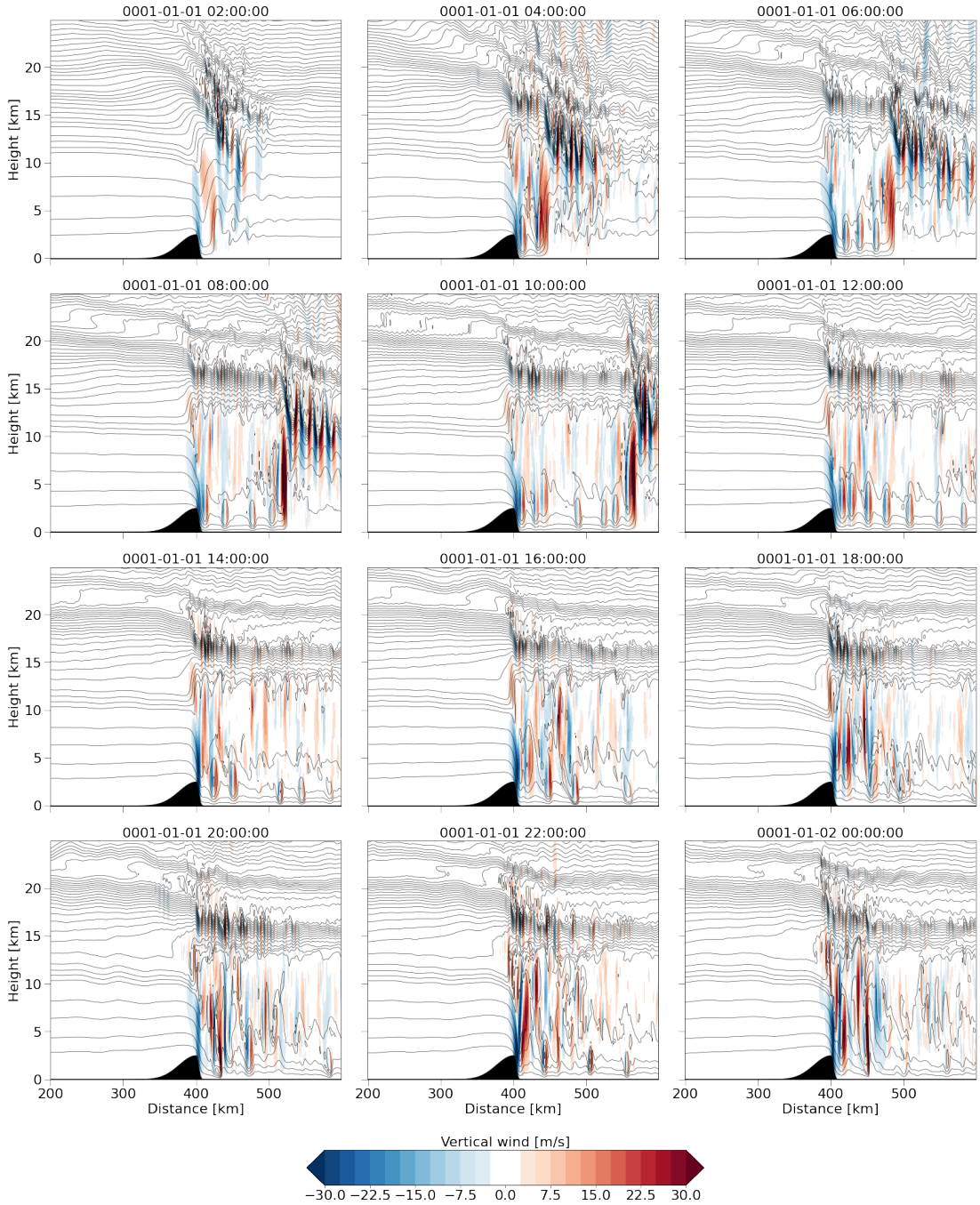

Figure 3.11: G2500 - domain 800 km (400 km showed), 24 hours simulation, vertical wind velocities.

distribution of the drag due to large turbulence and mixing reaching values larger by an order.

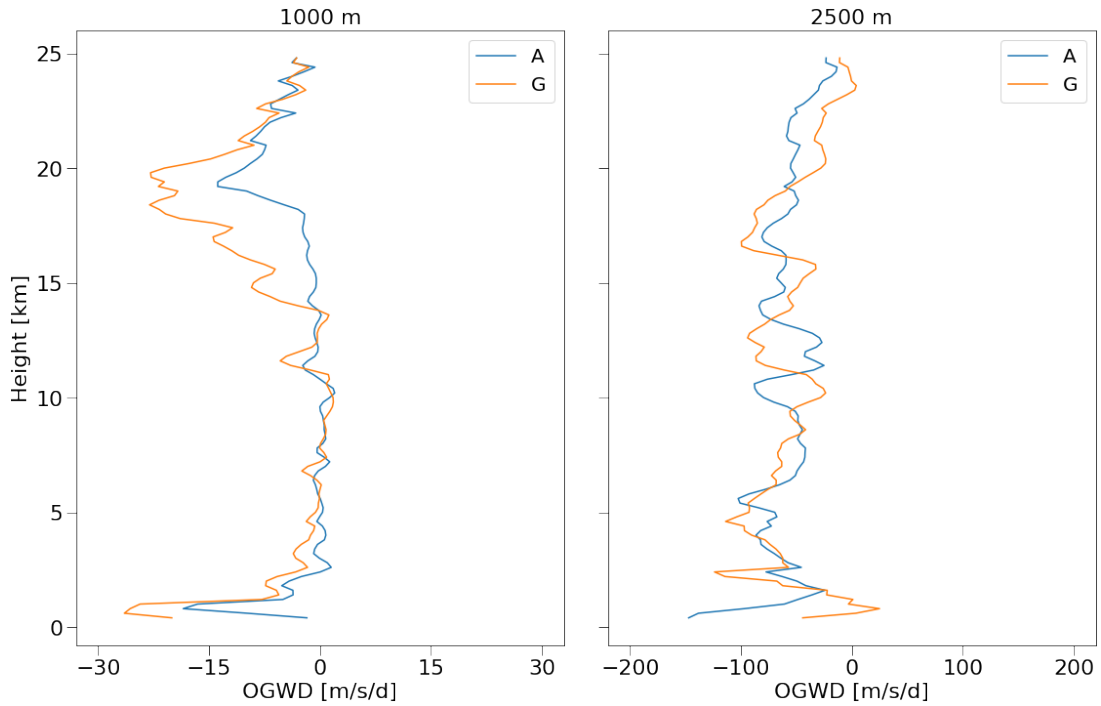

Figure 3.12: OGWD calculated for simulations A1000, A2500, G1000 and G2500 (1000 m hills on the left, 2500 m on the right)

3.3 Off-line calculations of parameterization

In this section we will replicate the high-resolution simulation with simulations on a coarse resolution grid. We have chosen horizontal resolution of 100 km and 200 km, which is appropriate for general circulation models on global scales. We will then apply different parameterization schemes and compare the resulting drag with the original high-resolution simulation.

3.3.1 Coarse resolution simulation

Firstly, we have to create grid scale orography (GSO). Normally, first step is to filter out any features on scales smaller than 5 km [Elvidge et al., 2019]. However in our case of single smooth hill we can skip this step. We simply calculate the mean orography height from the high-resolution orography. We will do that for each grid point. This will become GSO for the simulation. There will be 20 grids in the 100 km resolution and 10 in the 200 km resolution, making the domain much larger at 2000 km in length, with the hill still placed in the middle.

For off-line calculations with the different parameterizations we need information about SSO. Firstly we will subtract GSO from the high resolution one. Then, there are usually 4 parameters for each grid point representing standard deviation, slope, anisotropy and angle of SSO. Standard deviation, μ, is calculated as usual as a root mean square of the variance of SSO. Slope, σ, is defined as a root mean square of the horizontal gradient of orography

$$\sigma = \sqrt{\overline{\frac{\partial h}{\partial x}}^2} \,. \tag{3.9}$$

Anisotropy, i.e. variations of the orography in different directions, in our two dimensional case does not have to be defined. The same applies for the angle, which defines direction of the wind in relation to the mountain, and which is zero for 2D simulations. This set of parameters is further supplemented by a maximum height.

The low resolution simulations are run with the same sounding information and are performed for 24 hours as well.

3.3.2 Estimating the parameterized drag offline.

We base our work on research of different parameterization schemes described in [Hájková and Šácha, 2024]. We apply the set of various parameterization schemes using different components, changing the individual parameters, to asses impacts of these changes.

First step common for every parameterization is to define base momentum flux. We can define it as

$$\tau(p_i) = -EKh_e^2\rho_0 N_0 U_0, \tag{3.10}$$

where E is an efficiency factor of the order of unity, K is a factor concerning the horizontal wave number of the resulting wave and h_e is the effective height of the mountain. All variables are taken near surface at reference level p_i.

The definition of the parameter K differs between different parameterizations. For our tests we will firstly use standard definition $K = \kappa/2$, where κ is a horizontal wave number usually fixed for the whole globe. It varies from $\sim 10^{-6}$ to $\sim 10^{-3}$. We will also use another definition using the slope, σ, and the standard deviation, μ as in [Lott, 1999],

$$K = \frac{\sigma}{4\mu}. \tag{3.11}$$

The main difference between those two definitions is that the slope is not constant for the whole domain and is defined for each grid.

We will continue with defining the effective height, h_e, because the height of the obstacle may be limited by the critical Froude number. That is because once the Froude number is higher than some critical value (usually of the order of unity) the flow instead of going above the hill can go around (not in our 2D case) or the low level gravity wave breaking may occur. Either way the effective height that will give rise to the mountain waves will be smaller than the actual height of the obstacle. This can be estimated using the inverse Froude number definition as

$$h_e = min\left(h_m, \frac{F_c U(p_i)}{N(p_i)}\right). \tag{3.12}$$

h_m is usually defined using standard deviation as $h_m = 2\mu$, e.g. in [McFarlene, 1997]. We will use this definition as well as the definition following [Lott, 1999], which equals it simply to the maximum of SSO height at a given grid box.

In the 3D case, the base momentum flux would be further multiplied by factors depending on the anisotropy and the angle, which are of the order of unity. In that sense, their effect is similar to the efficiency parameter.

Once we have defined the base momentum flux, we can also define the drag from a low-level breaking. This can be done by either considering the drag coefficient [Lott and Miller, 1997], which is more connected to the blocking effects which do not apply here due to the 2D nature of the simulations. Another option, which is more simplistic, is to take the difference between the maximum base momentum flux and the actual one limited by the critical Froude number. That is we will use the same Equation 3.10 but apply $h_e = h_m$. So, if the limitations defined by critical Froude number have not been reached, there will be no OGWD near surface. The resulting drag is then equally distributed to all levels below the reference one.

We will also adopt another approach introduced by [Iwasaki et al., 1989]. Instead of applying the low level breaking, we will employ a second wave, which will be assigned its own momentum flux. In contrast to the first wave, the second wave will have a shorter horizontal wavelength and will be dissipating according to

$$\tau(z) = \tau(p_{i2}) \frac{(p(z) - p(9000))^2}{(p(p_{i2}) - p(9000))^2}, \tag{3.13}$$

where p_{i2} is a reference level below p_i. This is based on an assumption that there are shorter waves developing at lower levels, which are, however, trapped and dissipate up to 300 $hPa \sim 9000$ m.

So far we have defined the base momentum flux and the low level drag. We also need to formulate the saturation hypothesis, i.e. how much momentum flux can be carried through each specific level without any drag deposition. We will do that similarly to the way we defined the base momentum flux. For each level we will calculate the saturation momentum flux using Equation 3.10, with the effective height defined as $h_e = F_c U/N$. If the momentum flux is larger then the saturation momentum flux, the difference will be deposited at the level using Equation 3.8. The wave will continue propagating upwards but the momentum flux will be diminished by the amount that was distributed in this level. The Froude critical number for the saturation test is usually the same as for the base momentum flux definition, but can also differ.

Most parameterization schemes do not consider other effects concerning gravity waves dynamics, but we will additionally account also for the resonance and reflection effects similar to the scheme used in CNRM model as described in [Roehrig et al., 2020].

Resonance effect is based on the work of [Peltier and Clark, 1986] and we did not modify it any way from how it is used in the CNRM model. The effect lies in applying additional drag to all levels below the first critical level, which can be already the reference level, or usually some level close above. This means quite near surface, which is in accordance with the theory of resonance as we described in the first section.

That said, for the reflection effect we had to introduce certain modifications. In the original scheme, reflection is considered only in cases where the Brunt-Väisälä frequency drops to zero and the atmosphere is neutrally stratified, meaning the waves cannot propagate upwards anymore. These cases are however quite unusual. Drag is then applied to all levels below this critical one based on the amount of momentum flux carried by the wave. We will instead adopt different approach, considering reflection at every level, where the Brunt–Väisälä frequency

will change its gradient from positive to negative as to account for possible quick decreases of stability. This is based on the theoretical background from the Chapter 1 of the thesis. To calculate the amount of drag deposited in the levels below reflection, we will use a modification of Equation 1.54. We will approximate vertical wavenumber m by N/U and we will suppose that the changes of wind speed between the two levels are negligible so we will get the reflective index

$$r = \frac{N_1 - N_2}{N_1 + N_2}. \tag{3.14}$$

We will then deposit a drag to this level equal to the product of the momentum flux with the reflective index. Although being a very crude approach for accounting for the reflection, it is the first step towards a better vertical variance for parameterized OGWD.

This was a brief description of the parameterization schemes used further for off-line estimation of the drag from the unresolved orography. Details on all simulations and selected values of free parameters used in our tests are inTable 3.1.

test	w. n.	slp	std	max	2. w.	s. drg	ref.	res.	F_c	F_{cs}
base 1	1	0	1	0	0	0	0	0	1	1
base 07	1	0	1	0	0	0	0	0	0.7	0.7
base 05	1	0	1	0	0	0	0	0	0.5	0.5
difF 107	1	0	1	0	0	0	0	0	1	0.7
difF 105	1	0	1	0	0	0	0	0	1	0.5
difF 071	1	0	1	0	0	0	0	0	0.7	1
difF 0705	1	0	1	0	0	0	0	0	0.7	0.5
difF 051	1	0	1	0	0	0	0	0	0.5	1
difF 0507	1	0	1	0	0	0	0	0	0.5	0.7
kgw4	1	0	1	0	0	0	0	0	1	1
slope	0	1	1	0	0	0	0	0	1	1
maxim	1	0	0	1	0	0	0	0	1	1
twowave	1	0	1	0	1	0	0	0	1	1
lowlevstd	1	0	1	0	0	1	0	0	1	1
lowlevmax	1	0	0	1	0	1	0	0	1	1
reson	1	0	1	0	0	0	0	1	1	1
reflection	1	0	1	0	0	0	1	0	1	1

Table 3.1: Summary of the performed off-line parameterization tests. First 8 columns represent which variant of the scheme was used, last 2 represent value of certain nondimensional tunable parameters. w.n. - wave number, slp - slope, std - standard deviation, max - maximum height, ref - reflection, res - resonance, F_c- Froude critical number, F_{cs} - Froude critical number for saturation limit. Wave number $\kappa = 10^{-5}$, for all except kgwe4 where $\kappa = 10^{-4}$. $\kappa_2 = 4 * 10^{-5}$ is a value for the smaller wave in twowave scheme.

As a base reference we used $F_c = 1$, effective height defined using the standard deviation and wave number $\kappa = 10^{-5}$, based on the review of existing parameterization schemes and their setups in [Hájková, 2022]. Drag estimates using

the parameterization schemes were calculated off-line using the coarse resolution simulations and SSO information as an input. For each parameterization setup there is 8 different results, accounting for 4 simulations A1000, G1000, A2500 and G2500, using coarse resolutions of 100 km and 200 km for each of them.

3.3.3 Results of offline parameterization calculations

We will start with the base test *base*1. Results of the scheme are in Figure 3.13

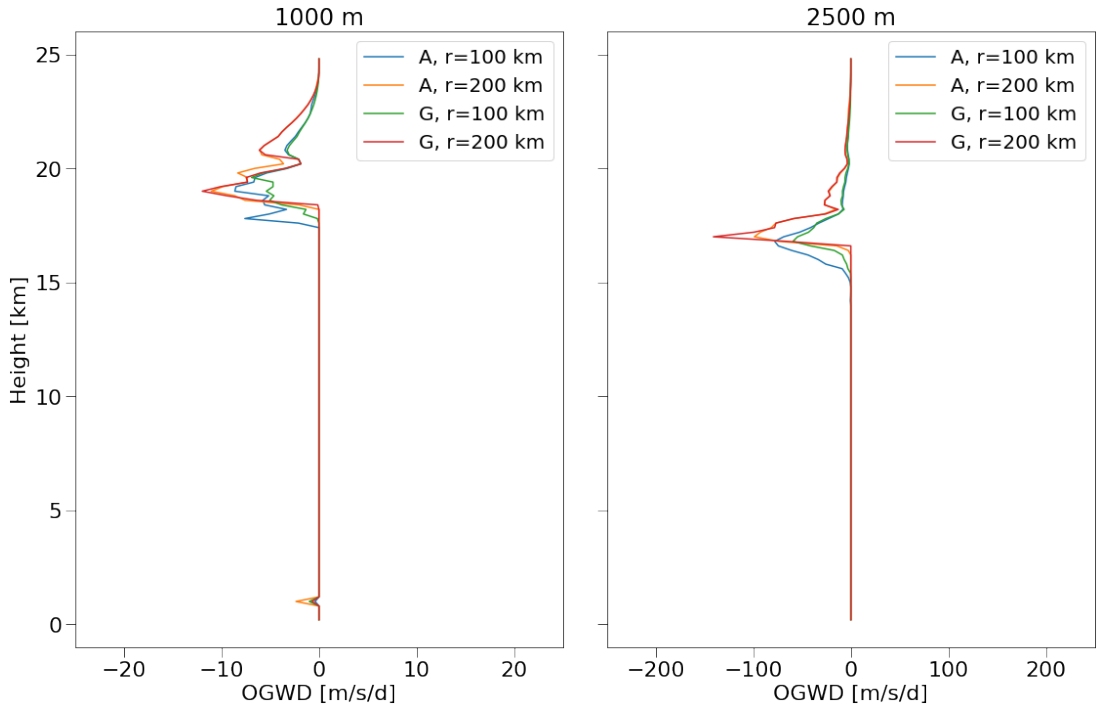

Figure 3.13: OGWD calculated using *base*1 parameterization scheme. Average over time and the domain.)

Firstly, we will notice the magnitude of the drag. The resulting drag from the parameterization is of the same order as for the high-resolution simulations. Looking at the 1000 m hill simulation on the left in Figure 3.13, we can see that for some of the simulations there is a small amount of low-level drag, coming from exceeding the saturation limit in the levels just above the reference level. Then, we can see the breaking region of freely propagating waves at around 20 km for all simulations, as expected. There is a quite clear division between 100 km resolution simulations and 200 km ones. We see earlier breaking for the higher resolution but smaller peaks in the levels above. Interestingly, we can also see higher values for Witch of Agnesi hill with 100 km resolution, which is in contradiction to our high-resolution results. Differences between Agnesi and Gaussian hills with 200 km resolutions are, as we expected, much smaller due to the same standard deviation. We can also see that there is no drag being distributed between the two previously identified breaking regions. This is due to the increasing stability and strong winds in the UTLS. Only when the winds drop enough, the saturation limit can be reached.

The issue of vertical distribution is more acutely seen in the 2500 m hill simulation on the right in Figure 3.13. This striking difference between the param-

eterized and simulated drag in Figure 3.12 could be attributed to the limitation of off-line calculation. On-line calculation would possibly provide the model with enough drag to cause the turbulence and subsequently more frequent breaking of the waves. However, our parameterized OGWD has the similar profile to the 1000 m hill although correctly reaching larger values by an order. The upper level breaking is lower then for 1000 m hills as we would expect due to larger values and we can once again see earlier deposition as well as lower peaks for the 100 km resolution simulations.

Results for tests *base*07 and *base*05 are in the Attachment, Figure A.4, Figure A.5. Due to lowering of both Froude critical number and saturation critical number, the resulting drag does not differ much in the vertical distribution from the *base*1 but significantly in the magnitude, which drops with lower critical number. Main difference we can see is that the altitude of upper level breaking is more similar between 100 km and 200 km resolution simulations in case of 2500 km hills.

We will now move to tests with different choice of the Froude number $diffF$. The idea behind having different F_c and F_{cs} is that by the first one we control the amount of the momentum flux launched to the atmosphere and by the other we can control the vertical distribution. As we can see in Figure 3.14, by choosing larger critical number for the definition of the base momentum flux and smaller for the saturation limit, we will get more drag near surface and less at the upper-level breaking region.

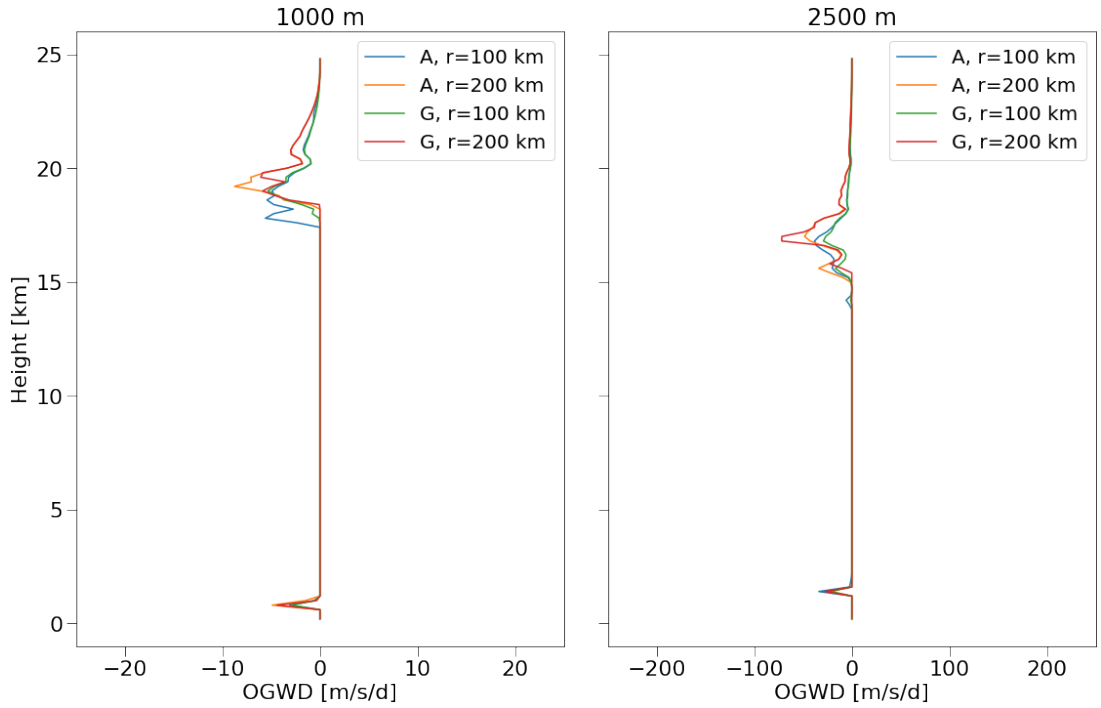

Figure 3.14: OGWD calculated using $diffF107$ parameterization scheme. Average over time and the domain.)

We can further observe this effect in $diffF105$ in the Attachment Figure A.6, where the shift of drag towards the surface is even stronger.

On other other hand, by choosing larger critical number for the saturation hypothesis, we can eliminate drag near surface, Figure 3.15 and in the extreme

case of $diffF051$, Figure 3.16, we can also see diminishing of the drag in the upper-levels and altogether a shift of the breaking altitude upwards.

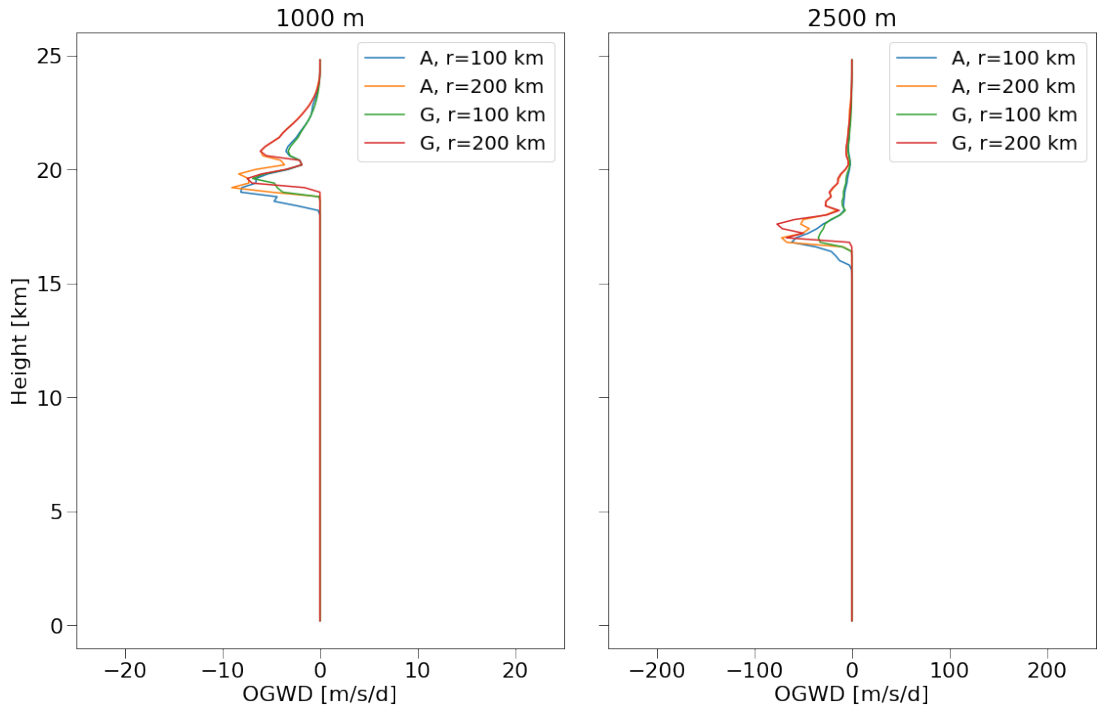

Figure 3.15: OGWD calculated using $diffF071$ parameterization scheme. Average over time and the domain.)

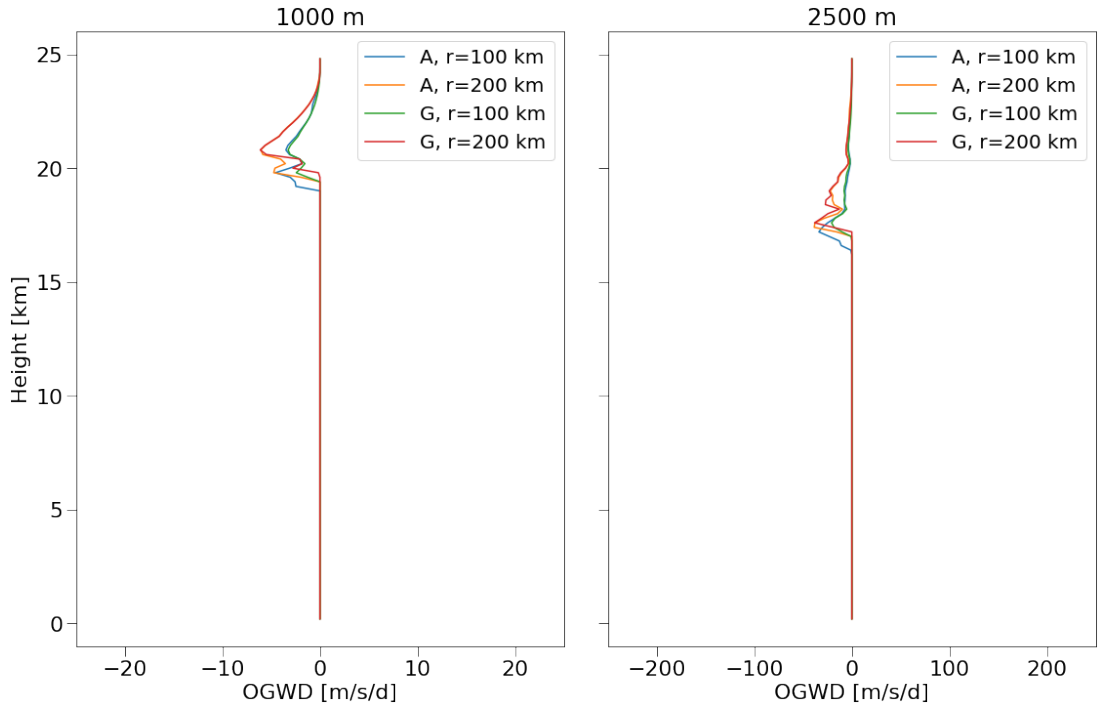

Figure 3.16: OGWD calculated using $diffF051$ parameterization scheme. Average over time and the domain.)

The remaining set of the $diffF$ test results can be found in the Attachment

Figure A.7, Figure A.8.

We will now keep both critical numbers equal to 1 and focus on effects of different parts of the parameterizations. As we could see in the test *base*1, local values of the $OGWD$ do reach the same order as the high-resolution ones. Due to otherwise small vertical distribution, it seems however that the whole amount of drag and hence momentum flux is underestimated.

This can be mitigated by choosing more appropriate values of the horizontal wave number κ. Our first choice $\kappa = 10^{-5}$ might seem like a possible underestimation, but it is not an unusual choice for GCMs and it demonstrates how global models can underestimate the amount of momentum flux carried by the wave. For our test $kgw4$ we chose larger value, $\kappa = 10^{-4}$ which is more accurate for our specific orography. We can see the results in Figure 3.17.

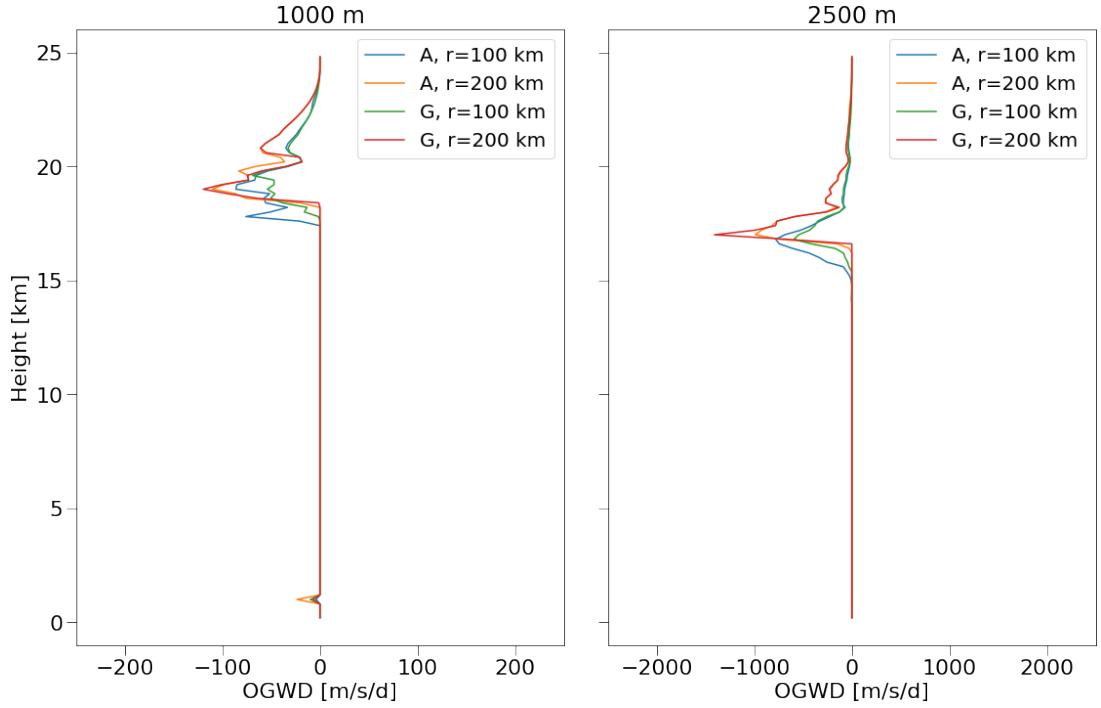

Figure 3.17: OGWD calculated using $kgw4$ parameterization scheme. Average over time and the domain.

As a direct consequence of the different choice of the characteristic horizontal wave number, we can see by an order larger values of OGWD. This brings the net momentum flux closer to the expected values (as we will show later), but locally gives unrealistically large amounts of drag at the specific levels.

In the following, we will continue with different definition of the wave number. It will not be a fixed parameter, but it will depend on a varying slope and the standard deviation as defined in Equation 3.11. This takes into consideration the diversity of the orography, by specifying the value for each grid by using SSO data. In this case we would expect larger differences between the Agnesi and Gaussian hills. Looking at Figure 3.18, we can see that for the 100 km resolutions we get quite a large amplification of the drag in comparison with the *base*1 test. However, we do not see the significant variations between Agnesi and Gaussian hills as we would expect. This might be because the ratio with standard deviation in Equation 3.11 could actually mask the difference. Even for the 200

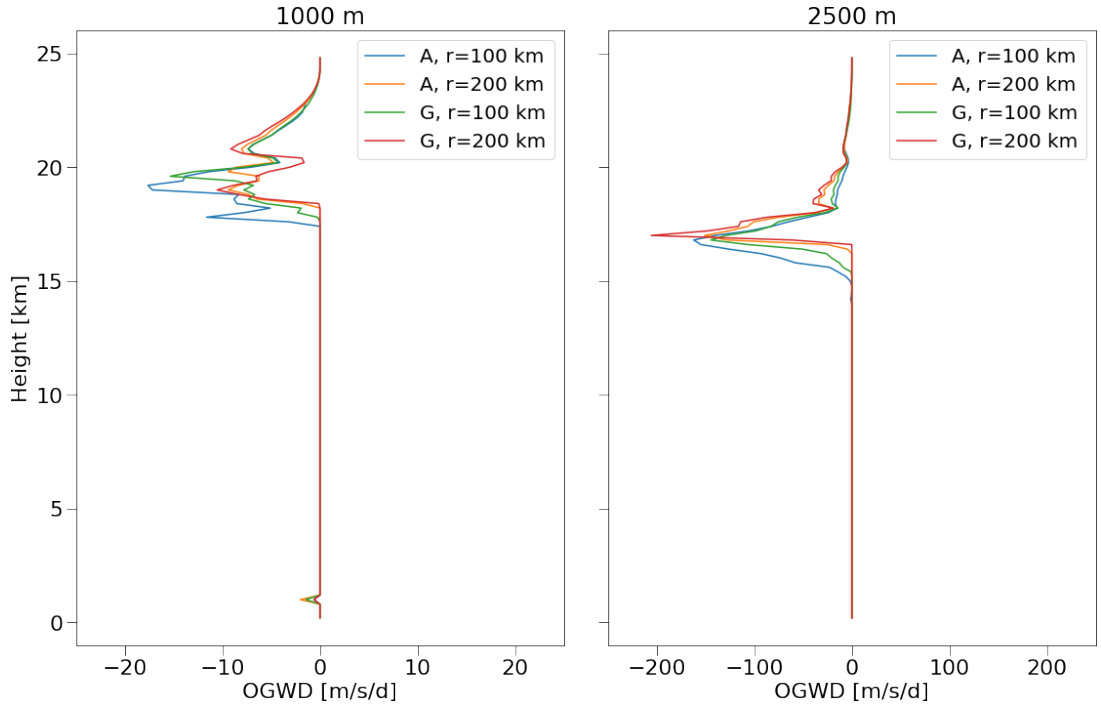

Figure 3.18: OGWD calculated using *slope* parameterization scheme. Average over time and the domain.

km resolution tests, where the standard deviation is the same, we can see that the Guassian hills reach higher values only slightly. It seems that although quite small differences in the slope of the mountains cause a large differences in the reality, due to coarse resolution those differences in SSO are not enough to reflect the real effects.

We will now turn to the impact of the definition of the effective height. It is argued in [Lott, 1999] that using standard deviation leads to incorrect elevations in some cases. This is possibly because standard deviation considers the shape of the hill as well, which in some cases does not have to be strictly connected to the maximum height. We can go around this problem by simply using only the maximum height of the SSO above the grid height to define the effective height. We can see the results in Figure 3.19.

Since we are now not considering the shape of the mountain at all, we can see only small differences between the different hills of the same resolution, which can be caused by the differences in the background flow. Looking at the magnitude we can also see increase of the drag. Comparing with test *base*1, in the case of the 1000 m hills we can see larger peaks and in the case of 2500 m hills we can rather see earlier wave breaking, with a broader vertical distribution of the drag.

We will now look at schemes, which consider other effects connected to OGWs. The *twowave* scheme deploys second, smaller wave, which is supposed to be trapped. The two wave scheme results in a moderate amount of the drag being distributed in the troposphere, in accordance with the definition, as we see in Figure 3.20. Generally the inclusion of the second wave did not bring any unexpected results. Differences between values of each simulation reflect what we saw in the previous tests.

None of the previous set-ups considered the drag due to blocking and the near

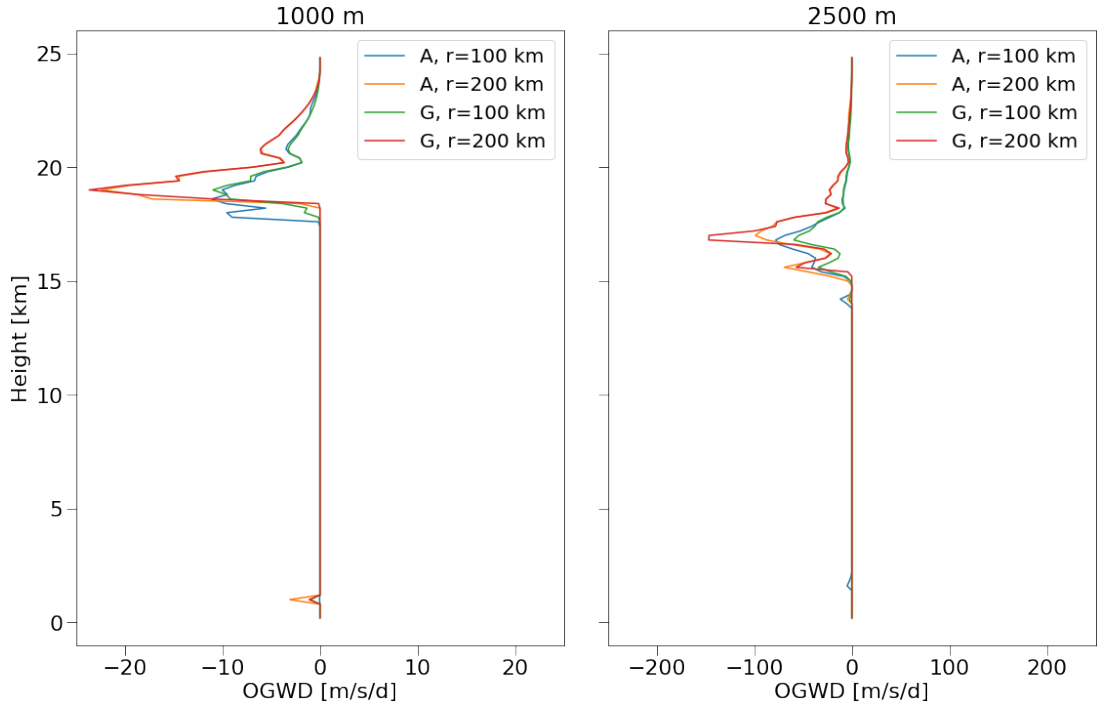

Figure 3.19: OGWD calculated using *maxim* parameterization scheme. Average over time and the domain.

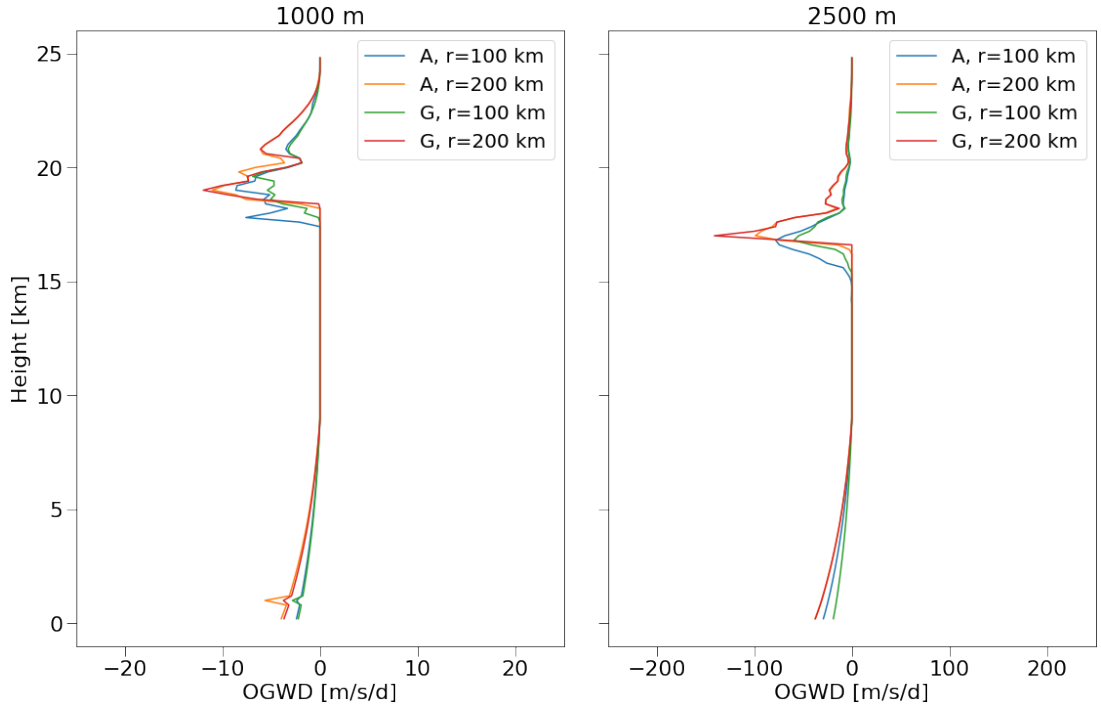

Figure 3.20: OGWD calculated using *twowave* parameterization scheme. Average over time and the domain.)

surface breaking of the waves, which is a consequence of the definition of the base momentum flux. We will now add these mechanisms to the same set-ups which were used in *base*1 and *maxim*. We chose these test because of the different description of effective height, to compare the impacts of the definitions on the

low-level drag. In Figure 3.21 we can see the *lowlevstd* test. For both heights of the hill, we can see rather small amount of the near surface drag which does not agree with the results of high-resolution simulations. Looking at the second case

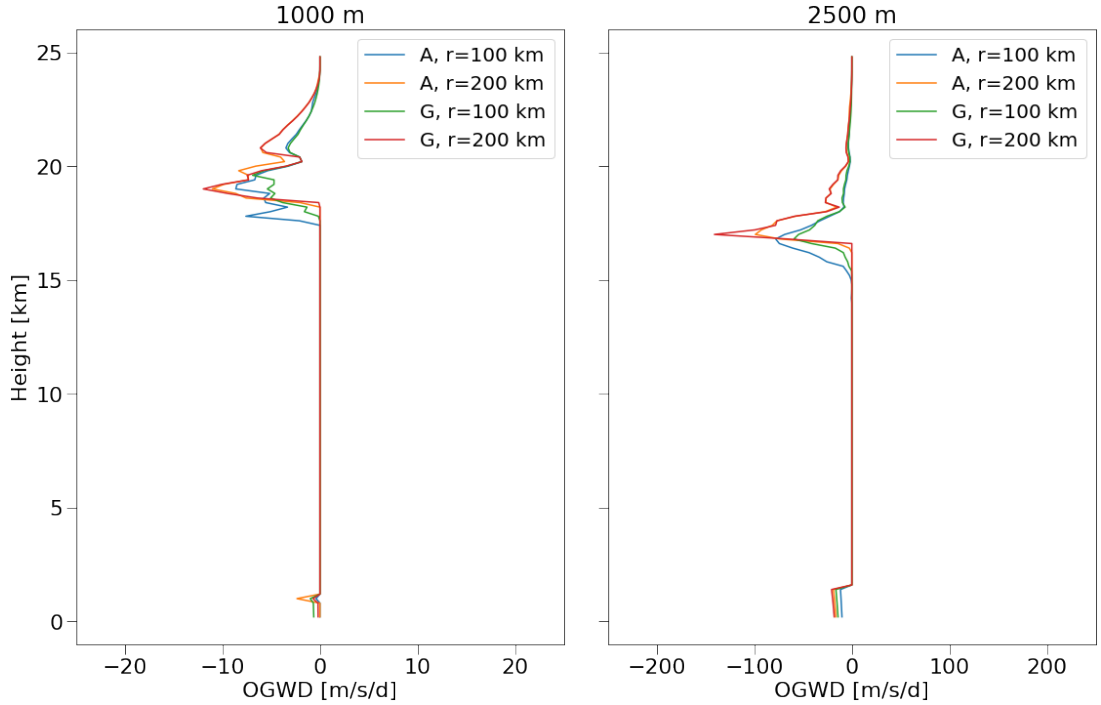

Figure 3.21: OGWD calculated using the *lowlevstd* parameterization scheme. Average over time and the domain.

lowlevmax in Figure 3.22, we do see significant amount of the drag deposited at the near surface levels, especially in the case of the 2500 m hills. Also, we can see a clear distinction between the types of the hills. Since we are using the definition of a maximum height, which does not consider the shape of the orography, this could be attributed to the slightly different wind speeds between the coarse resolution simulations. This leads to capturing the larger drag from the Guassian type of the hill. Looking closer this applies for the *lowlevstd* setup as well.

Last two schemes we will look at, will employ effects of resonance and reflection, starting with the resonance. Based on its definition, we expect its effects only near the surface, as we can confirm in Figure 3.23.

In comparison to *lowlev* schemes, the distinction between the 1000 m and 2500 m after including the resonance effects is more subtle, with relatively larger values seen in 1000 m hills.

We will finish this section with including the reflection effects. In Figure 3.24 we see that even the simplistic use of a reflective index does add some small amount of variation to the vertical distribution of the drag between the low-level and lower stratospheric drag regions. It seems that for the cases of smaller hills it is able to at least partially reproduce the peaks as seen in the high-resolution simulations. However, for the larger hill, the amount of drag by reflection is almost negligible compared to the pronounced drag maximum in the profile as the scheme can not capture the turbulent nature of this simulation. But, this could not have been expected.

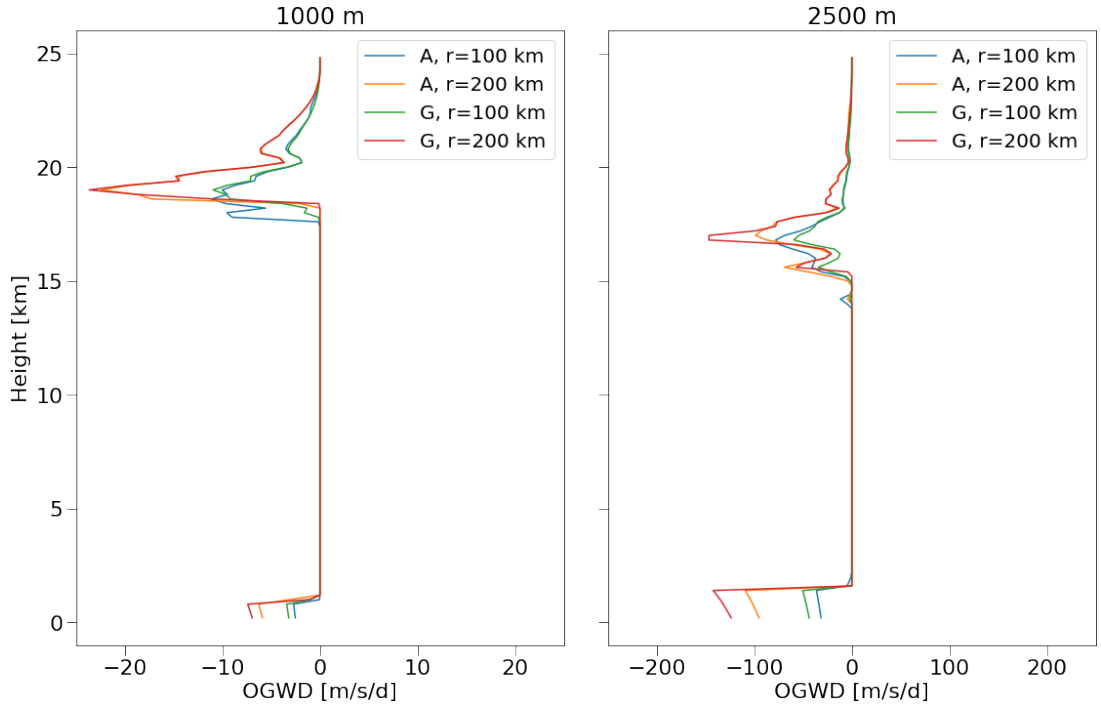

Figure 3.22: OGWD calculated using the *lowlevmax* parameterization scheme. Average over time and the domain.

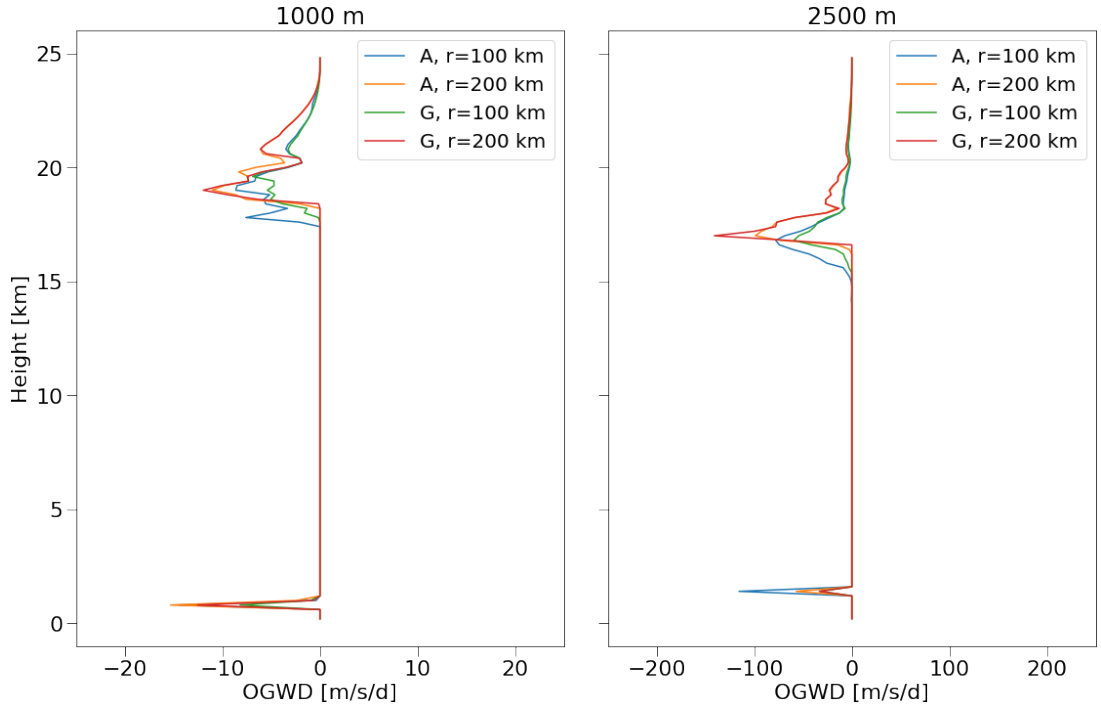

Figure 3.23: OGWD calculated using the *reson* parameterization scheme. Average over time and the domain.)

3.3.4 Discussion of results of parameterization schemes

We will now discuss the results of our parameterization tests. Firstly, it must be said that these were only off-line calculations and we do not have online compu-

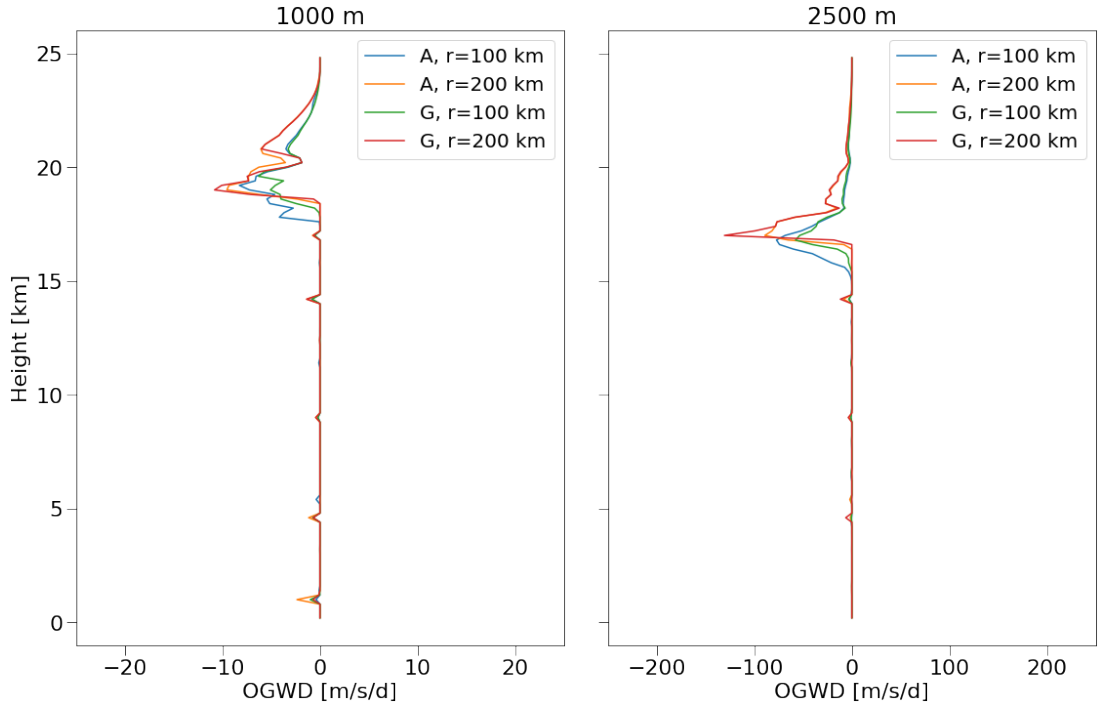

Figure 3.24: OGWD calculated using the *reflection* parameterization scheme. Average over time and the domain.

tations for comparison. This means that the parameterized drag was not communicated back to the model and was therefore not able to alter the background flow, which would in turn modify the computed parameterized drag.

For a full insight into the previous results concerning resulting drag profiles, in Table 3.2 we list the momentum flux transported to the free atmosphere after the low-level breaking. We include only the tests for which the base momentum flux is different.

	A1000100	A1000200	A2500100	A2500200	G1000100	G1000200	G2500100	G2500200
High-Res	-0.11278		-5.14569		-0.32143		-5.42674	
base 1	-0.02557	-0.03264	-0.22216	-0.22642	-0.01941	-0.02608	-0.14248	-0.23288
base 07	-0.0176	-0.02009	-0.14178	-0.1759	-0.01193	-0.01483	-0.08902	-0.16692
base 05	-0.00905	-0.01231	-0.0741	-0.09084	-0.00627	-0.00954	-0.04542	-0.08962
maxim	-0.03064	-0.04922	-0.28678	-0.36215	-0.02508	-0.04263	-0.18167	-0.35849
kgw4	-0.2557	-0.3264	-2.22156	-2.26421	-0.19408	-0.26085	-1.4248	-2.32879
slope	-0.04744	-0.03355	-0.46203	-0.31784	-0.0355	-0.02786	-0.33996	-0.33099

Table 3.2: Calculated momentum fluxes for the high-resolution simulation and each test, $[m^2/s^2]$.

We can see that although the peaks of OGWD did locally reach comparable values, the actual amount of momentum flux propagated vertically is much smaller for all the parameterization set-ups (for example in the case of *base*1 smaller by an order). We can also see the expected distinction between the Agnesi and Gaussian hills in the case of 1000 m height for the high-resolution simulation. This confirms that for the steeper hill we do not have only more breaking near the surface, but also stronger wave activity transported upwards. It seems however that parameterization schemes were not able to accurately represent that.

Looking at the three *base* experiments, we can see the large disparity between them. All of these critical number values are actively used in state-of-the-art climate models [Hájková, 2022]. This demonstrates that the parameterized drag does not have to represent the real physical values that would actually be there in more realistic cases. There is a possible argument that the tuning is based on the biases of zonal wind speed in the models and that the resulting drag will have to be the same. However, as we saw in actual cases in Chapter 2, this is not the case and also it would be applicable only if the bias was homogeneous throughout the atmosphere, which is usually not the case at all.

Using *maxim* scheme seems to not only enlarge the whole momentum flux, but also widen the differences between the underlying horizontal resolutions of the coarse grid simulations. This suggests that, this approach is more resolution sensitive.

As we already saw in Figure 3.18, using combination of the slope and standard deviation seems to estimate more OGW drag in the 100 km resolution simulations, which is actually opposite of what we see in other tests. Also even this scheme was not able to properly represent the different shapes of the hills. This is possibly because the differences between the slope were too small for the coarse resolution to truly effect the results.

Last point concerning momentum fluxes that we want to highlight is connected with the choice of the wave number. Of course, the larger value of the wave number did result in the greater momentum flux as expected, but it also accentuated the underestimation for the higher hill. In the 1000 m cases, the momentum flux is now either greater or relatively close to the high-resolution values. On the contrary, in cases of 2500 m hills, we get less then half of the resolved momentum flux. This shows how the parameterizations is less able to capture the more extreme cases involving strongly nonlinear flow regimes.

Summarising the results of the rest of the tests, schemes $diffF$ demonstrated the use of different critical numbers in controlling the vertical distribution of the drag. This can possibly help in the cases where there are biases of the wind speed in particular vertical levels.

To account for the low-level drag in the schemes, one needs to utilise the concept of the effective height. Our *lowlevel* schemes show large differences depending on its definition. Although not surprising, it suggests that better approach, as is for example in [Lott, 1999], is needed to represent the effects of blocking and near-surface breaking more accurately.

The scheme including the resonance seems to capture the effect correctly. Relatively larger values for the 1000 m hill could be a good indicator that the scheme can recognise the good resonance condition we see in the high-resolution simulations.

Overall, we can say that the possibly biggest problem is the lack of a greater variability in the vertical distribution of the drag. In the middle troposphere we cannot get any drag due to high winds. This is in accordance with the linear theory, but in the reality we get much more turbulent flow, especially in the extreme case of 2500 m. Our $reflection$ scheme does add small amount of vertical variability, but it can be considered realistic only in the 1000 m hill cases, where the added drag in the troposphere can be possibly at least partially accounted to the reflection effects. The very strong mixing in the 2500 m case, would be

however probably represented in online calculations, which would consider effects of large added drag near surface.

Conclusion

In the first chapter of this thesis, we introduced theory behind the orographic gravity waves. We started by deriving the governing equations. Using these we then derived the TGE, which describes the resulting windfield in linear cases, as well as the conditions for vertical propagation of the waves. We also showed the energy conservation laws and the possible non-linear effects concerning waves such as reflection and resonance.

We followed with providing a motivation for the research of OGWs by showing how large is the impact of parameterized drag on the resolved dynamics in global circulation models. We expanded the previous research from [Hájková, 2022], using multiple models and realisations to show robust correlations between OGW drag and the refractive index that describes ability of the atmosphere to allow propagation of large scale waves. We were also able to further confirm the relationship between parameterized and resolved drag, showing both compensation as well as amplification depending on the analyzed location. This is especially important since the tuning parameters of the OGW schemes are always individually tuned for each model based on the possible biases it has. This however means that the drag does not necessarily represent the real values we would found in a real atmosphere.

Last part of this work starts with high-resolution simulations of overflowing of four different hills. We analyzed the simulations, looking for differences between resulting wave fields, breaking and other non-linear effects. Further, we replicated these simulations, using 2 different coarse resolution set-ups, trying to mimic global circulation model. This section was followed by an application of chosen versions of parameterization schemes. Using different tuning and modifications, we tried to show the sensitivity to the choices and to what extent the schemes are able to reproduce the real drag from high-resolution simulations.

Similarly to my bachelor thesis, this work will lay the basics for my following research, which will go in two directions.

Results from the second chapter will be further analyzed. We need to better understand the causality between propagation of the planetary waves and the parameterized drag near surface as well as in the lower stratosphere. Our results showed a clear connection which we will further investigate. Resolved waves are an important variable for correct prediction of sudden stratospheric warmings (SSW) in models, [Wu and Reichler, 2020]. Previous research already showed that differences in OGW schemes have significant impact on the simulated SSW frequency [Sigmond et al., 2023]. Our goal is to better quantify the impact of the parameterized drag, continuing with CMIP6 data to perform a further multimodel analysis.

The off-line parameterization calculation is the first step in further research, with an ultimate goal of developing a new parametrization scheme. Our results showed huge dependence on the tuning parameters as well as the horizontal resolution. Where quite small difference in the shape of the mountain causes a large differences in the wave activity in the high-resolution simulations, those differences are not well represented by the parametrisations. This stands even when using SSO information such as slope.

Otherwise, the schemes were to some degree able to replicate the drag in cases of the smaller hills, although the vertical distribution as well as the momentum flux were underestimated. This effect was more evident in the cases of more extreme hill. We hope to continue our work with on-line application of the schemes to WRF-ARW to properly analyse these effects and determine the source of the problems.

Results from both section show the continuous need for better understanding of the OGW processes as well as for improvement of their representation in global climate models. This topic has a big societal relevance, as these improvements could help to improve both the short-term weather forecasts as well as the long-term projections.

Bibliography

U. Achatz. *Atmospheric Dynamics*. Springer Spektrum Berlin, Heidelberg, 2022. ISBN 978-3-662-63941-2.

M. J. Alexander, M. Geller, C. McLandress, S. Polavarapu, P. Preusse, F. Sassi, K. Sato, S. Eckermann, M. Ern, A. Hertzog, Y. Kawatani, M. Pulido, T. A. Shaw, M. Sigmond, R. Vincent, and S. Watanabe. Recent developments in gravity-wave effects in climate models and the global distribution of gravity-wave momentum flux from observations and models. *Quarterly Journal of the Royal Meteorological Society*, 136(650):1103–1124, 2010. doi: https://doi.org/10.1002/qj.637.

D. Andrews, C. Leovy, and J. Holton. *Middle Atmosphere Dynamics*. Academic Press, London, UK, 1987. ISBN 9780120585762.

D. G. Andrews and M. E. McIntyre. Planetary waves in horizontal and vertical shear: The generalized eliassen-palm relation and the mean zonal acceleration. *Journal of Atmospheric Sciences*, 33(11):2031 – 2048, 1976. doi: 10.1175/1520-0469(1976)033⟨2031:PWIHAV⟩2.0.CO;2.

F. P. Bretherton. Momentum transport by gravity waves. *Quarterly Journal of the Royal Meteorological Society*, 95(404):213–243. doi: https://doi.org/10.1002/qj.49709540402.

Oliver Bühler. *Waves and Mean Flows*. Cambridge Monographs on Mechanics. Cambridge University Press, 2 edition, 2014. ISBN 9781107478701.

N. Y. Cohen, E. P. Gerber, and O. Bühler. Compensation between Resolved and Unresolved Wave Driving in the Stratosphere: Implications for Downward Control. *J Atmos Sci*, 70:3780–3798, 2013. doi: 10.1175/JAS-D-12-0346.1.

N. Y. Cohen, E. P. Gerber, and O. Bühler. What Drives the Brewer–Dobson Circulation? *J Atmos Sci*, 71:3837–3855, 2014. doi: 10.1175/JAS-D-14-0021.1.

James D. Doyle and Dale R. Durran. The dynamics of mountain-wave-induced rotors. *Journal of the Atmospheric Sciences*, 59(2):186 – 201, 2002. doi: 10.1175/1520-0469(2002)059⟨0186:TDOMWI⟩2.0.CO;2.

James D. Doyle and Carolyn A. Reynolds. Implications of regime transitions for mountain-wave-breaking predictability. *Monthly Weather Review*, 136(12):5211 – 5223, 2008. doi: 10.1175/2008MWR2554.1.

James D. Doyle, Saša Gaberšek, Qingfang Jiang, Ligia Bernardet, John M. Brown, Andreas Dörnbrack, Elmar Filaus, Vanda Grubišić, Daniel J. Kirshbaum, Oswald Knoth, Steven Koch, Juerg Schmidli, Ivana Stiperski, Simon Vosper, and Shiyuan Zhong. An intercomparison of t-rex mountain-wave simulations and implications for mesoscale predictability. *Monthly Weather Review*, 139(9):2811 – 2831, 2011. doi: 10.1175/MWR-D-10-05042.1.

R. Eichinger, H. Garny, and P. et al. Šácha. Effects of missing gravity waves on stratospheric dynamics; part 1: climatology. *Clim Dyn*, 54, 2003. doi: 10.1007/s00382-020-05166-w.

A. Eliassen and Palm E. *On the Transfer of Energy in Stationary Mountain Waves*. Geofysiske publikationer. 1961.

Andrew D. Elvidge, Irina Sandu, Nils Wedi, Simon B. Vosper, Ayrton Zadra, Souhail Boussetta, François Bouyssel, Annelize van Niekerk, Mikhail A. Tolstykh, and Masashi Ujiie. Uncertainty in the representation of orography in weather and climate models and implications for parameterized drag. *Journal of Advances in Modeling Earth Systems*, 11(8):2567–2585, 2019. doi: https://doi.org/10.1029/2019MS001661.

D.C. Fritts and M.J. Alexander. Gravity wave dynamics and effects in the middle atmosphere. *Reviews of Geophysics*, 41(1):3165–3183, 2020. doi: 10.1007/s00382-020-05166-w.

Adrian E. Gill. *International geophysics series. Volume 30, Atmosphere-ocean dynamics*. International geophysics series ; 30. Academic Press, New York, 1982. ISBN 0122835220.

S Goldstein and Geoffrey Ingram Taylor. On the stability of superposed streams of fluids of different densities. *Proceedings of the Royal Society of London. Series A, Containing Papers of a Mathematical and Physical Character*, 132 (820):524–548, 1931. doi: 10.1098/rspa.1931.0116.

Vanda Grubišić, James D. Doyle, Joachim Kuettner, Stephen Mobbs, Ronald B. Smith, C. David Whiteman, Richard Dirks, Stanley Czyzyk, Stephen A. Cohn, Simon Vosper, Martin Weissmann, Samuel Haimov, Stephan F. J. De Wekker, Laura L. Pan, and Fotini Katopodes Chow. The terrain-induced rotor experiment: A field campaign overview including observational highlights. *Bulletin of the American Meteorological Society*, 89(10):1513 – 1534, 2008. doi: 10.1175/2008BAMS2487.1.

Ethan Gutmann, Idar Barstad, Martyn Clark, Jeffrey Arnold, and Roy Rasmussen. The intermediate complexity atmospheric research model (icar). *Journal of Hydrometeorology*, 17(3):957 – 973, 2016. doi: 10.1175/JHM-D-15-0155.1.

James R Holton. *An introduction to dynamic meteorology*, volume 41. American Association of Physics Teachers, fifth edition, 2013. ISBN 978-0-12-384866-6.

D. Hájková. Type of the scheme and tuning dependence of the parameterized orographic gravity wave drag distribution in global climate models. Charles University, Faculty of Mathematics and Physics, 2022. Bachelor's Thesis.

D. Hájková and P. Šácha. Parameterized orographic gravity wave drag and dynamical effects in cmip6 models. *Clim Dyn*, 62:2259–2284, 2024. doi: 10.1007/s00382-023-07021-0.

Toshiki Iwasaki, Shinichi Yamada, and Kazumasa Tada. A parameterization scheme of orographic gravity wave drag with two different vertical partitionings: Part i: Impacts on medium-range forecasts. *Journal of the Meteorological Society of Japan. Ser. II*, 67:11–27, 01 1989. doi: 10.2151/jmsj1965.67.1_11.

Martin Jucker. Scaling of eliassen-palm flux vectors. *Atmospheric Science Letters*, 22(4):e1020, 2021. doi: https://doi.org/10.1002/asl.1020.

Martin Jucker and rjaiser. mjucker/aostools: aostools v2.6, 2023. Zenodo.

J. B. Klemp and D. R. Lilly. The dynamics of wave-induced downslope winds. *Journal of Atmospheric Sciences*, 32(2):320 – 339, 1975. doi: 10.1175/1520-0469(1975)032⟨0320:TDOWID⟩2.0.CO;2.

Joseph B. Klemp and Dale R. Durran. An upper boundary condition permitting internal gravity wave radiation in numerical mesoscale models. *Monthly Weather Review*, 111(3):430 – 444, 1983. doi: 10.1175/1520-0493(1983)111⟨0430:AUBCPI⟩2.0.CO;2.

Christopher G. Kruse, Ronald B. Smith, and Stephen D. Eckermann. The midlatitude lower-stratospheric mountain wave "valve layer". *Journal of the Atmospheric Sciences*, 73(12):5081 – 5100, 2016. doi: 10.1175/JAS-D-16-0173.1.

D. K. Lilly. Wave momentum flux—a garp problem. *Bulletin of the American Meteorological Society*, 53(1):17 – 24, 1972. doi: 10.1175/1520-0477-53.1.17.

D. K. Lilly. A severe downslope windstorm and aircraft turbulence event induced by a mountain wave. *Journal of Atmospheric Sciences*, 35(1):59 – 77, 1978. doi: 10.1175/1520-0469(1978)035⟨0059:ASDWAA⟩2.0.CO;2.

François Lott. Alleviation of stationary biases in a gcm through a mountain drag parameterization scheme and a simple representation of mountain lift forces. *Monthly Weather Review*, 127(5):788 – 801, 1999. doi: 10.1175/1520-0493(1999)127⟨0788:AOSBIA⟩2.0.CO;2.

François Lott and Martin J. Miller. A new subgrid-scale orographic drag parametrization: Its formulation and testing. *Quarterly Journal of the Royal Meteorological Society*, 123(537):101–127, 1997.

N.A. McFarlene. The effect of orographically excited gravity wave drag on the general circulation of the lower stratosphere and troposphere. *J Atmos Sci*, 59: 371–386, 1997. doi: 10.1175/1520-0469(1987)044⟨1775:TEOOEG⟩2.0.CO;2.

Michael McIntyre and Tim Palmer. The 'suf zone' in the stratosphere. *Journal of Atmospheric and Terrestrial Physics*, 46:825–849, 09 1984. doi: 10.1016/0021-9169(84)90063-1.

Charles McLandress, Theodore G. Shepherd, Saroja Polavarapu, and Stephen R. Beagley. Is missing orographic gravity wave drag near 60°s the cause of the stratospheric zonal wind biases in chemistry–climate models? *Journal of the Atmospheric Sciences*, 69(3):802 – 818, 2012. doi: 10.1175/JAS-D-11-0159.1.

C. J. Nappo. *An Introduction to Atmospheric Gravity Waves*. Volume 85, INTERNATIONAL GEOPHYSICS SERIES. Academic Press, San Diego, USA, 2002. ISBN 978-0-12-514082-9.

W.R. Peltier and T.L. Clark. *Nonlinear mountain waves and wave-mean flow interaction: elements of a drag parameterization*. PhD thesis, Shinfield Park, Reading, 1986 1986.

R.T. Pierrehumbert. An essay on the parameterization of orographic gravity wave drag. *Conference paper, Seminar/Workshop on Observation, Theory and Modelling of Orographic effects. Seminar: 15-19 September 1986, Workshop: 19-20 September 1986*, 1986.

R. Roehrig, I. Beau, D. Saint-Martin, A. Alias, B. Decharme, J.-F. Guérémy, A. Voldoire, A. Y. Abdel-Lathif, E. Bazile, S. Belamari, S. Blein, D. Bouniol, Y. Bouteloup, J. Cattiaux, F. Chauvin, M. Chevallier, J. Colin, H. Douville, P. Marquet, M. Michou, P. Nabat, T. Oudar, P. Peyrillé, J.-M. Piriou, D. Salas y Mélia, R. Séférian, and S. Sénési. The CNRM Global Atmosphere Model ARPEGE-C limat 6.3: Description and evaluation. *Journal of Advances in Modeling Earth Systems*, 12, 2020. doi: 10.1029/2020MS002075.

P. Sacha, A. Kuchar, R. Eichinger, P. Pisoft, C. Jacobi, and H.E. Rieder. Diverse Dynamical Response to Orographic Gravity Wave Drag Hotspots—A Zonal Mean Perspective. *Geophysical Research Letters*, 48(13), 2021. doi: 10.1029/2021GL093305.

M. Sigmond, J. Anstey, V. Arora, R. Digby, N. Gillett, V. Kharin, W. Merryfield, C. Reader, J. Scinocca, N. Swart, J. Virgin, C. Abraham, J. Cole, N. Lambert, W.-S. Lee, Y. Liang, E. Malinina, L. Rieger, K. von Salzen, C. Seiler, C. Seinen, A. Shao, R. Sospedra-Alfonso, L. Wang, and D. Yang. Improvements in the canadian earth system model (canesm) through systematic model analysis: Canesm5.0 and canesm5.1. *Geoscientific Model Development*, 16(22):6553–6591, 2023. doi: 10.5194/gmd-16-6553-2023.

W. C. Skamarock, J.B. Klemp, J. Dudhia, D. O. Gill, Z. Liu, J. Berner, W. Wang, J.G. Powers, M. G. Duda, D. M. Barker, and X.-Y. Huang. A description of the advanced research wrf version 4. (no. ncar/tn-556+str). *NCAR Tech.*, 2019. doi: 10.5065/1dfh-6p97.

B.R. Sutherland. *Internal Gravity Waves*. Cambridge University Press, 2010. ISBN 9781316184325.

Geoffrey Ingram Taylor. Effect of variation in density on the stability of superposed streams of fluid. *Proceedings of the Royal Society of London. Series A, Containing Papers of a Mathematical and Physical Character*, 132(820): 499–523, 1931. doi: 10.1098/rspa.1931.0115.

Zheng Wu and Thomas Reichler. Variations in the frequency of stratospheric sudden warmings in cmip5 and cmip6 and possible causes. *Journal of Climate*, 33(23):10305 – 10320, 2020. doi: 10.1175/JCLI-D-20-0104.1.

List of Figures

List of Tables

List of Abbreviations

GW gravity wave 2

OGW orographic gravity wave 2

OGWD orographic gravity wave drag 16

TGE Taylor-Goldstein equation 5

EPF Eliassen-Palm flux 17

EPFD Eliassen-Palm flux divergence 21

SSO sub-grid scale orography 15

GSO grid scale orography 39

GCM global circulation model 2

A. Attachments

A.1 First Attachment

Model	OGWD	EPFD	EPFz	RI
CanESM5	3	3	3	3
CESM2	3	3	3	3
CESM2-FV2	3	/	3	3
CESM2-WACCM	3	3	3	3
CNRM-CM6-1	1	/	1	1
CNRM-ESM2-1	1	/	1	1
GFDL-CM4	1	/	/	1
GFDL-ESM4	1	1	/	1
HadGEM3-GC31-LL	5	5	5	5
IPSL-CM6A-LR	21	2	21	21
MIROC-ES2L	3	/	3	3
MRI-ESM2-0	3	3	3	3
UKESM1-0-LL	1	1	1	1

Table A.1: Used CMIP6 models and number of realisations for each variable. OGWD and EPFD are taken from the CMIP6 database, EPFz and RI are calculated using available variables as described in the text.

A.2 Second Attachment

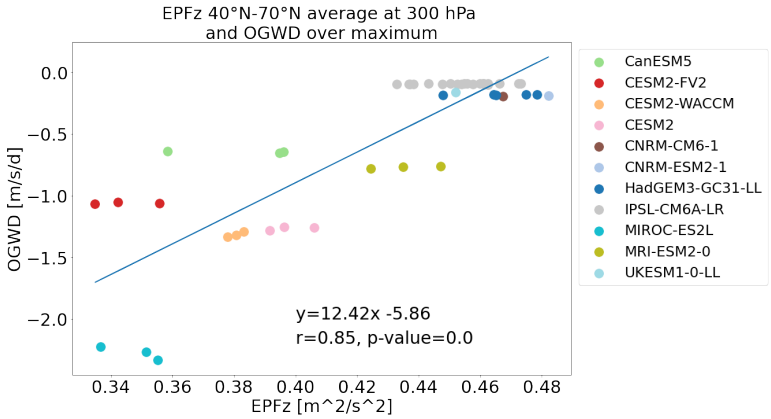

Figure A.1: Scatter plot of OGWD and the refractive index, OGWD taken over maximum near surface (30° - 45 °, 1000-500 hPa), EPF_z taken over and vertical levels as described

A.3 Third Attachment

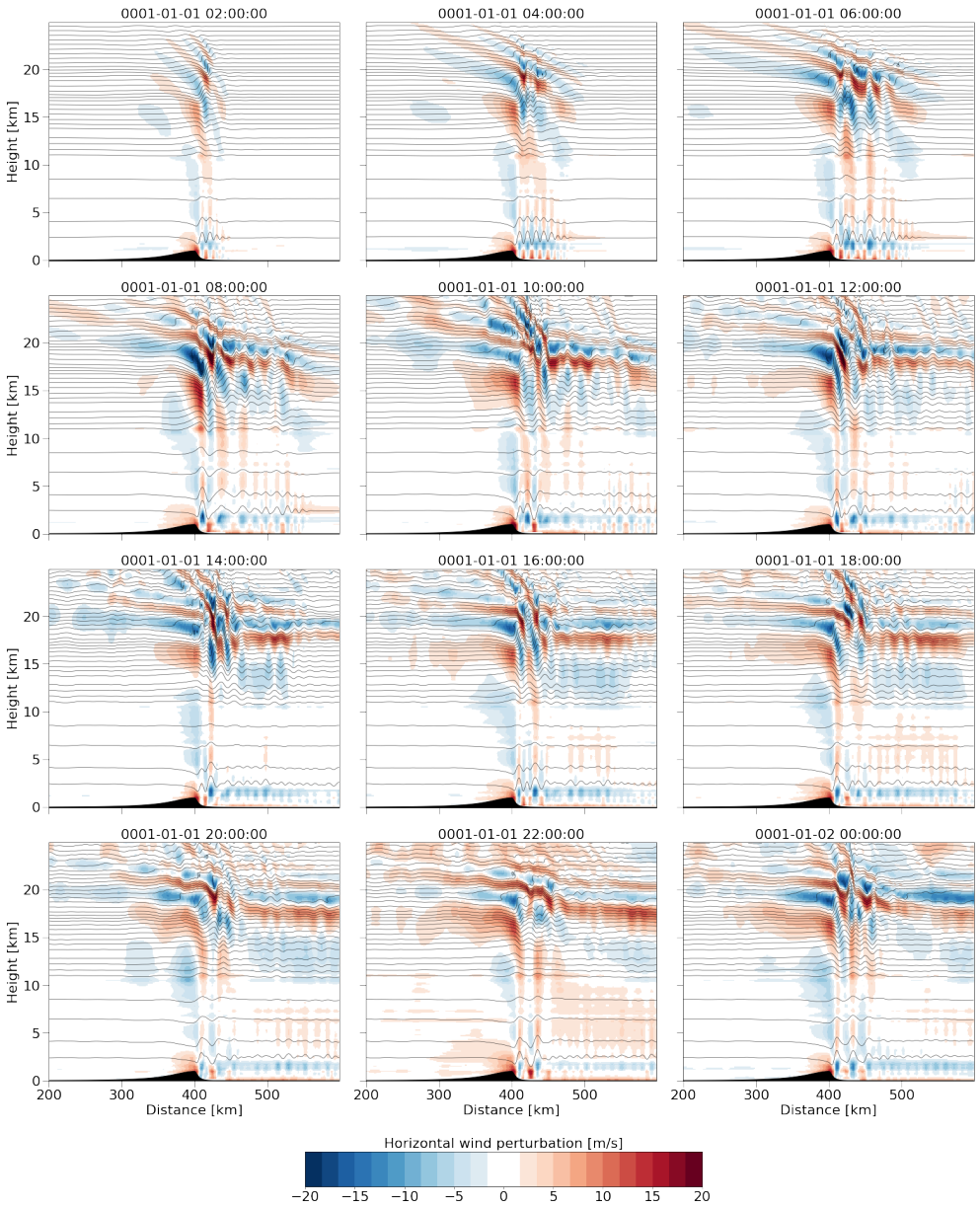

Figure A.2: A1000 - domain 800 km (400 km showed), 24 hours simulation, horizontal wind perturbations.

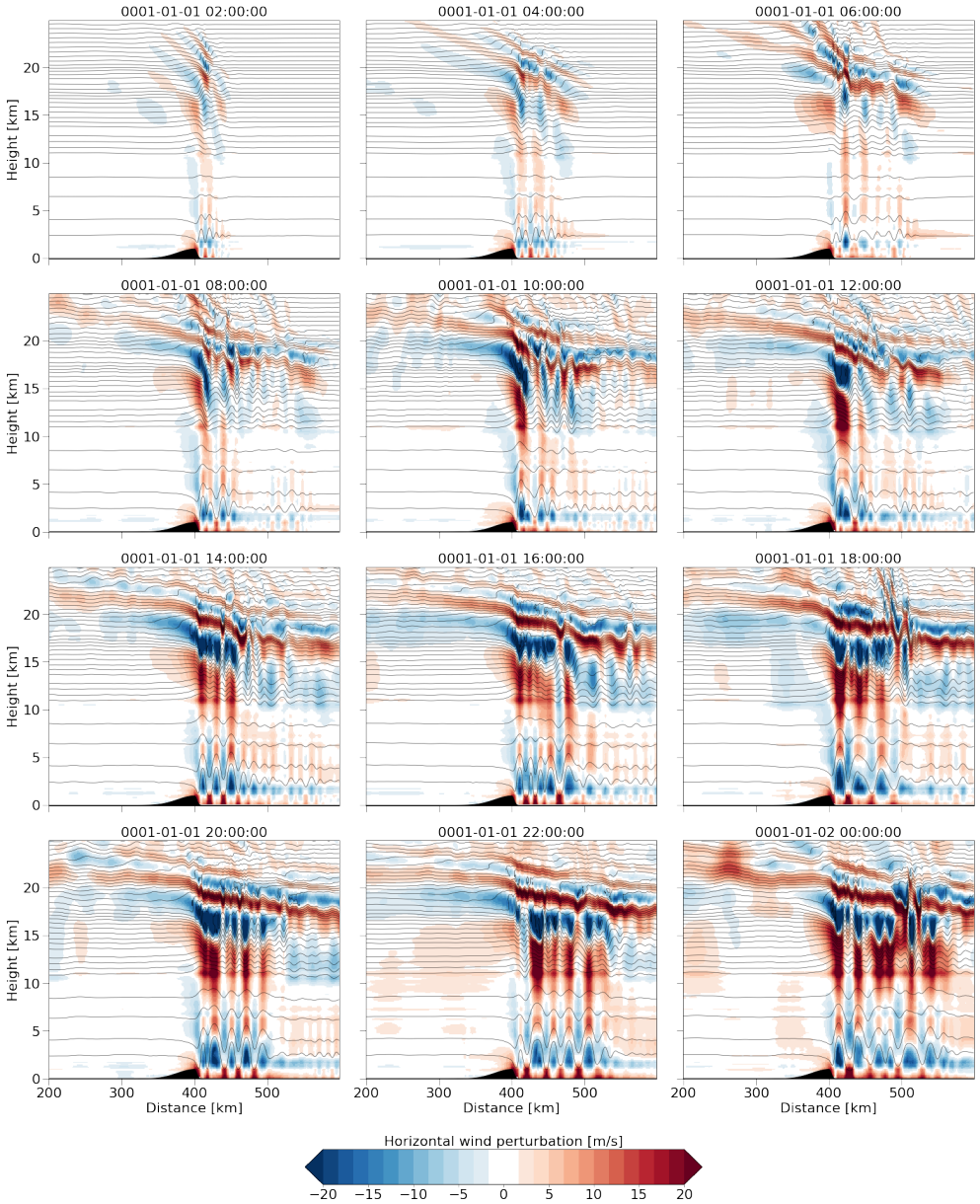

Figure A.3: G1000 - domain 800 km (400 km showed), 24 hours simulation, horizontal wind perturbations.

A.4 Fourth Attachment

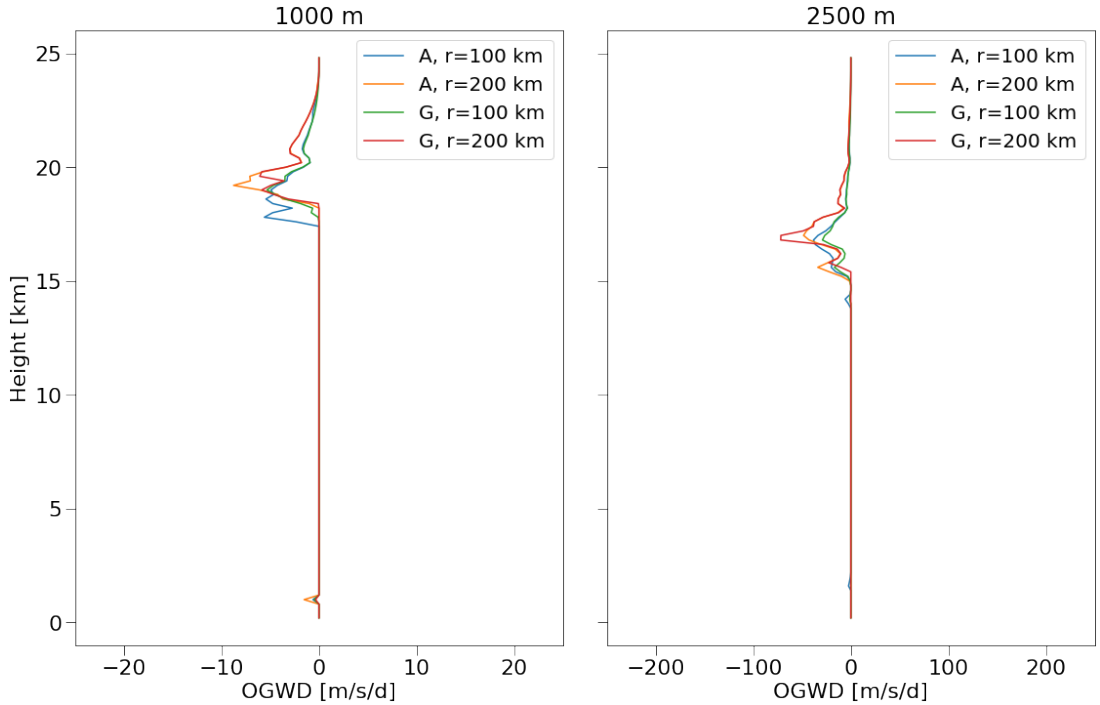

Figure A.4: OGWD calculated using *base*07 parameterization scheme. Average over time and the domain.)

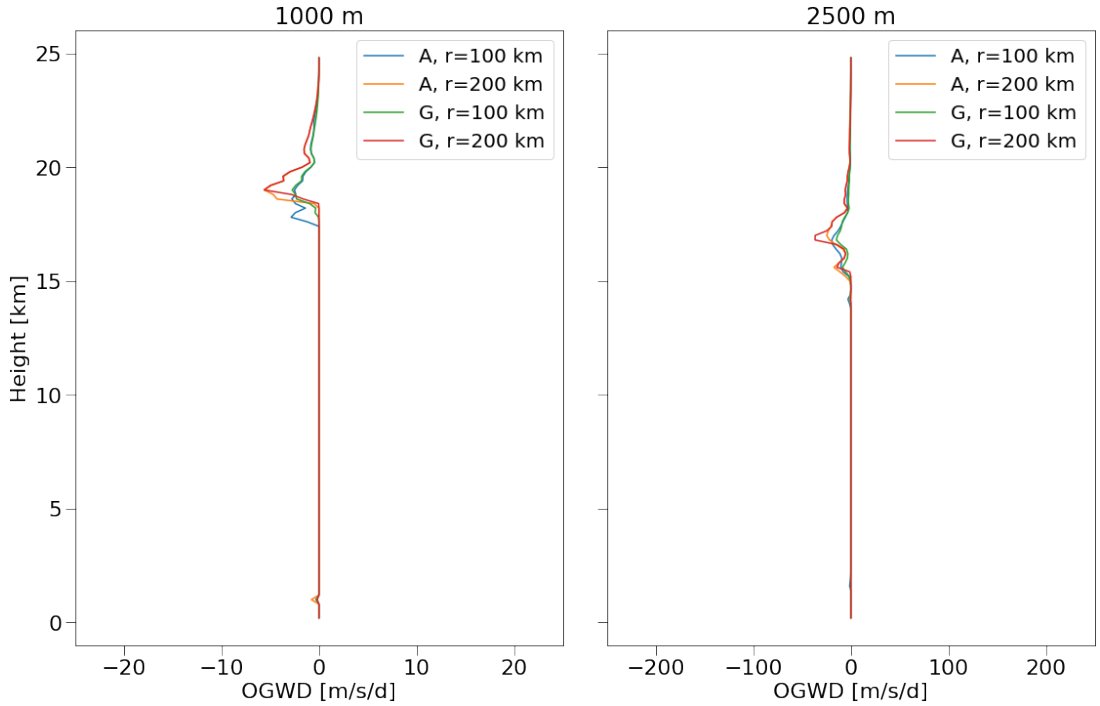

Figure A.5: OGWD calculated using *base*05 parameterization scheme. Average over time and the domain.)

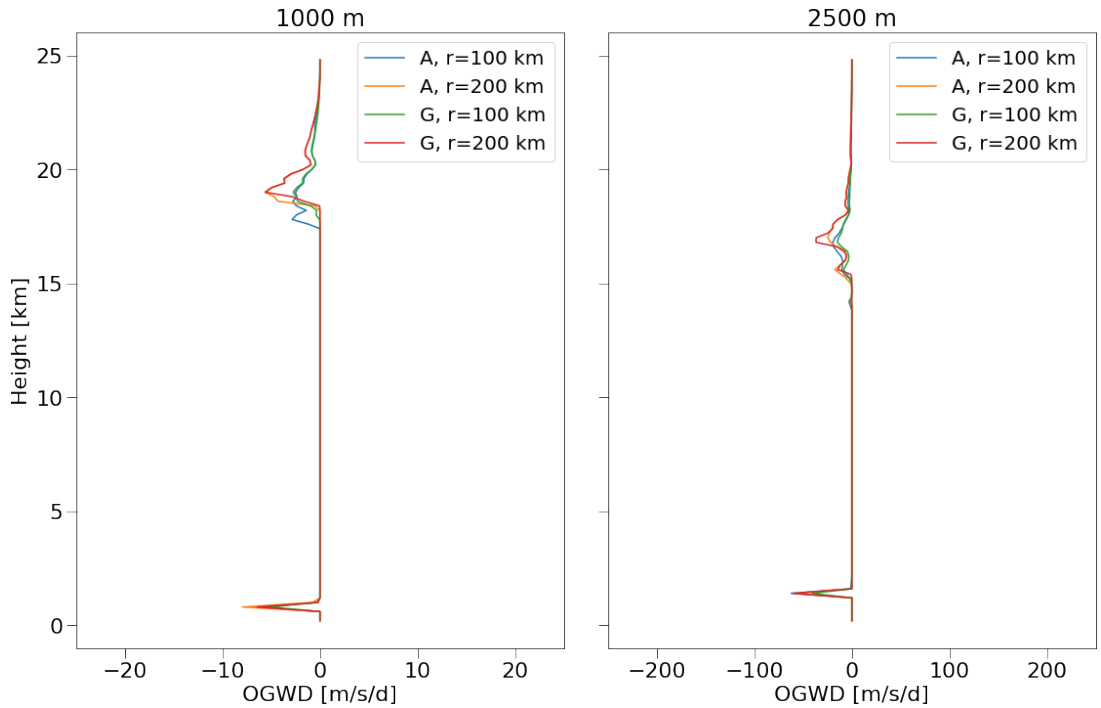

Figure A.6: OGWD calculated using $diffF105$ parameterization scheme. Average over time and the domain.)

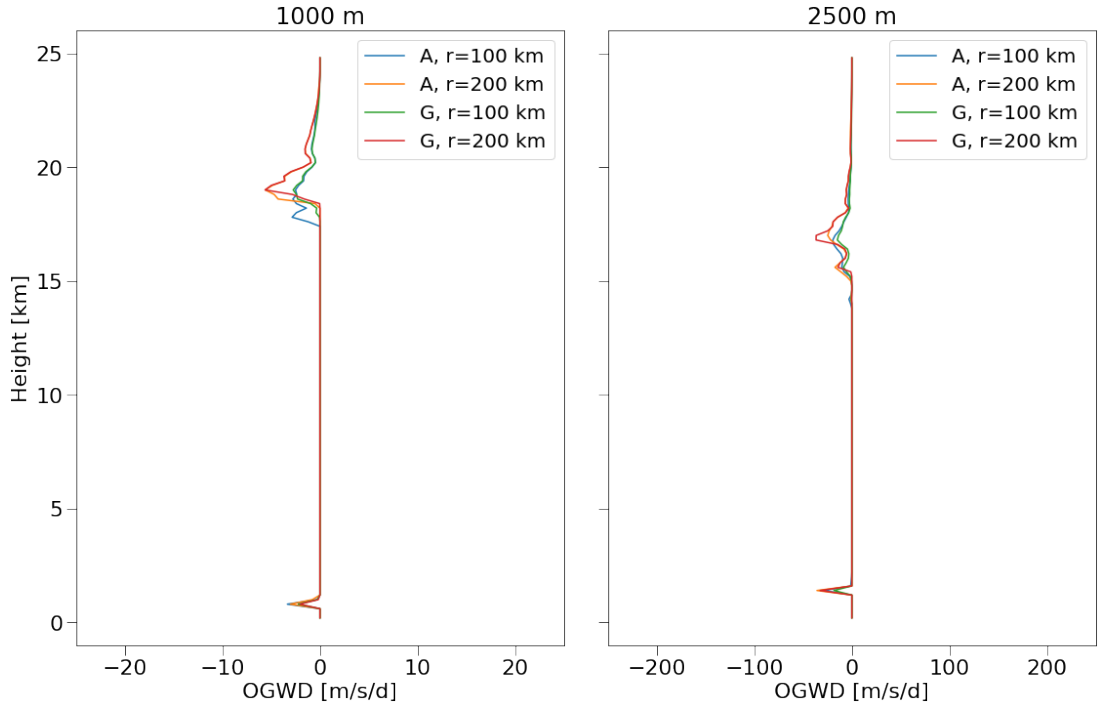

Figure A.7: OGWD calculated using $diffF07055$ parameterization scheme. Average over time and the domain.)

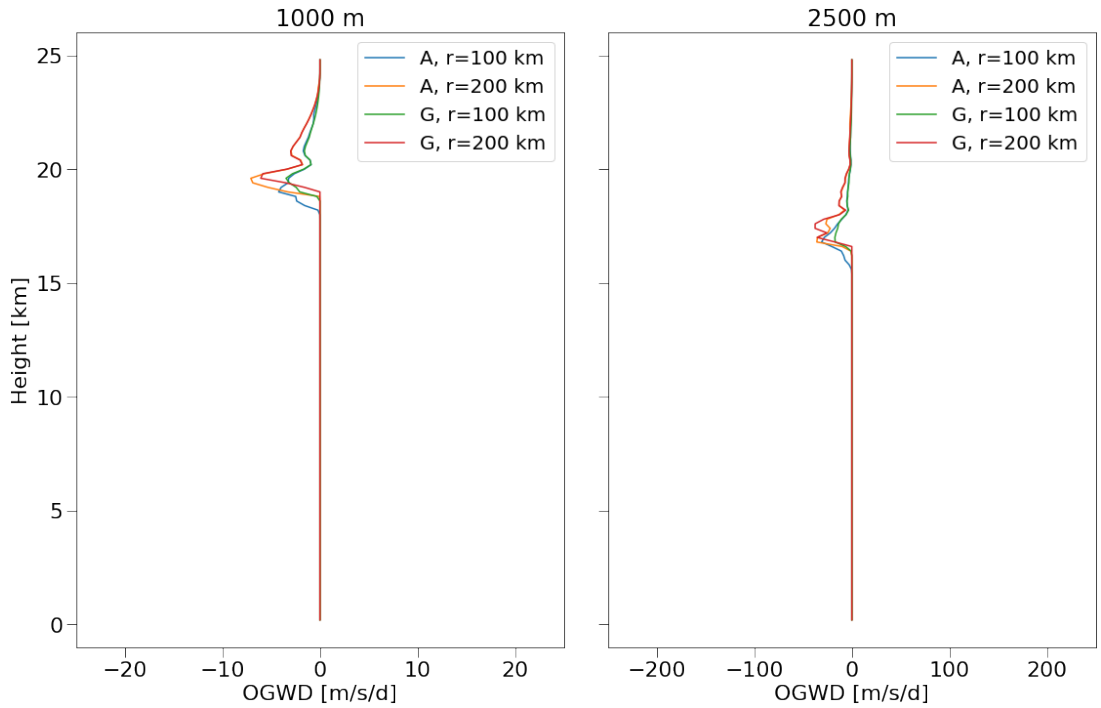

Figure A.8: OGWD calculated using $diffF0507$ parameterization scheme. Average over time and the domain.)